CENTRO DE INVESTIGACIONES
EN OPTICA, A.C.

"OPTIMIZATION OF A HELMHOLTZ RESONATOR FOR COOLING, BY THE SCHLIEREN TECHNIQUE"

Thesis submitted as a requirement for obtaining Master's degree in Optomechatronics

Presented by: Eng. Nkosinathi Carl Shongwe

Thesis advisor: Dr. Bernardino Barrientos García

León · Guanajuato · México
December 2021

Abstract

Experimental and simulation work is carried out to investigate and measure temperature variation of a Helmholtz resonator using the imaging techniques, Background Oriented Schlieren (BOS) and Fringe Deflection (FD). This research project contains the theoretical, numerical and experimental analysis of temperature measurement using optical methods. A comparison of the performance of temperature measurements between the two experimental techniques, Background Oriented Schlieren (BOS) and Fringe Deflection (FD) is reported. Both methods are based on measuring refractive index field gradients using a background image captured with a digital camera. The object to be examined is placed between the background image and the digital camera.

The BOS (Background Oriented Schlieren) technique is a newly established method for simple and inexpensive visualizing of refractive index gradient, temperature and density variation in compressible flows. The BOS design setup mainly consists of a background with randomly placed dots and a camera targeted on the dots. Variations between the uninterrupted image and the distorted image resulted in the dots displacement which is used by the optical flow method to create a displacement field. Fringe Deflection uses vertical fringes instead of the dotted background.

The results obtained show that Fringe Deflection is more efficient. The FD was then used to analyze a Helmholtz resonator. In the Helmholtz resonator experiment, a pulsed synthetic air jet is generated and directed onto a surface to be cooled. The results show that the relatively cooler air expelled from the resonator cavity interacts with the warmer air in the heated plate and cools the heated plate slightly. Since the cooling air is expelled again and again at a certain frequency, the process is repeated and cooler air is pumped to the hot plate.

Acknowledgments

The journey toward a Master's Degree cannot be undertaken alone. It is with the help of countless people on the way have I made it so far and I am forever grateful for their support. This Thesis is an effort to which several people have contributed, directly or indirectly, giving their opinion, correct it, being patient with me and encourage me to follow my dream. For these reasons, I would like to express my deepest and sincere thanks to them for helping me to make it happen.

I would particularly like to thank Dr. Bernardino Barrientos Garcia, my supervisor for this Thesis, for his invaluable help, mentorship, encouragement, guidance, all the time spent and for the motivation and opportunity to work on such an interesting project. It has truly been a privilege to work with Dr. Bernardino, and I am greatly indebted to him for everything he has taught me about research, life, and making it all balance together.

Special thanks to my mentors Dr. Gabrielle Thomas, Dr. Kaboko Jean-Jacques Monga and Nkeletseng MsKay Tsetsane for the support and encouragement.

To all of my friends and colleagues who have helped me grow as a person and always there for me in the good and bad times of my life. Many Thanks.

I would also like to thank my committee members, Dr. Damiano Sarocchi and Dr. Carlos Mares for providing their knowledge and assistance in all aspects of this research, as well as providing valuable feedback and guidance.

Outside of research, I have been extremely fortunate to have the support of a diverse group of friends who helped me keep things in perspective; Marissa Vásquez, Ana Karen Reyes, Joao Trujillo, Martin Figueroa, Marcel Saavedra, and dear friends who have accompanied me on this journey.

Special thanks to Dr. Rodolfo Martinez who made it possible for me to come to Mexico.

Finally, I also owe a great deal of thanks to the Centro de Investigaciones en Optica, $A.C.$, and Consejo Nacional de Ciencia y Tecnologia $(CONACyT)$ for the scholarship with registration number 961403 without which this research would not be possible.

Thank you all.

Declaration of authenticity

I hereby declare that this work was compiled by my authorship, except when specific reference is made to the work of others. The content of this work is original and has not been presented in whole or in part for any other degree in this or any other study center. This Thesis is the result of my own work and does not contain anything that is the result of work done in collaboration, unless specifically stated in the text.

Nkosinathi Carl Shongwe

León, Guanajuato, México

December 2021

Dedication

"I dedicate all my achievements
to you
my beloved **South Africa**"

Contents

List of Figures

List of Tables

Chapter 1

Introduction

Contents

In this first Chapter, the context of the Thesis is introduced. Section 1.1 contains the Background of this Thesis work. The Problem Statement is presented in Section 1.2. The Technical Analysis is described in Section 1.3. Section 1.4 explains the Goals and Objectives of the Thesis. The research Methodology is presented in Section 1.5. Section 1.6 presents the Thesis Organization, and lastly the Summary of the main Results are presented in Section 1.7.

1.1 Background and Motivation

The temperature is an important physical quantity in most industrial processes and in many scientific areas [1]. Designers and engineers face critical challenges in terms of the efficiency, availability and reliability of thermal management for various technical applications. Many material properties show a strong temperature dependence, therefore, it is desirable to have an efficient thermal management system that can effectively dissipate additional heat while controlling the local temperature distribution to improve reliability and prevent premature failure. Some application examples are convection drying, cooling of electronic devices, thermal management in photovoltaic panels and turbine blades. In order to use or to compensate temperature effects, its measurement is necessary. Examples of such temperature dependencies are density, electrical conductivity, refractive index, diffusion and rigidity [3]. Temperature measurement also plays an important role in monitoring the condition of electrical circuits or civil structures [4].

The temperature can arise through combustion due to complex interactions between chemical reactions, heat, substance and momentum transfer. Temperature is an important consequence of these interactions, which is why it is important to measure it. The latest and most accurate methods are used so that we can learn more about the process and this in turn helps save resources in case of energy, a problem that is common today. Cooling is critical as high temperatures are undesirable. A Helmholtz resonator is one of the devices and methods used to control surface temperature.

In this work a study is carried out to optimize a Helmholtz resonator for temperature control with the help of the Schlieren technique. A Helmholtz cooling resonator is analyzed, characterized and examined with optical technique (Fringe Deflection techniques). The technique is implemented to get an insight into the temporal behavior of a Helmholtz resonator. The technique is uninterruptive, whole field type, and robust to external sources of noise [21]. The optical setup is simplified in that only one camera is used to perform the analysis.

A simplified theory is derived to explain the experimental results. It is hoped that the current results will contribute to the future use of the Helmholtz resonator for cooling purposes.

1.2 Problem Statement

The cooling of hot devices, for example electronic circuits, is usually done with the help of mechanical fans. However, these types of devices are generally noisy and sometimes do not produce enough cooling for high speed microprocessors. An alternative is to use a cylindrical cavity in which one of the covers is deformable and can thus be brought into resonance, which increases the efficiency of the device (Helmholtz resonator). The cavity contains only one exit. In this work, the cavity orifice diameter and the operating frequency are investigated in order to maximize and optimize the performance of the Helmholtz resonator.

1.3 Technique Analysis

The measurement method using optical techniques is based on several fundamental principles which will be implemented for the analysis. The use of optical techniques for temperature measurement has the advantage over other methods because optical methods do not introduce any disturbance into the object to be examined. The entire field of view is also covered so that measurements can be carried out for an entire region. In this work two optical methods for temperature measurement are analyzed, Background Oriented Schlieren (BOS) and Fringe Deflection. Both techniques are able to measure displacement fields that are proportional to the gradient of the refractive index distributions within an observation area. In the BOS, a pattern of randomly arranged points is placed in the background, the object to be analyzed is placed between the background and the camera. Two images are taken, one with no object and the other with an object. These images are the reference and the displaced image. The reference and the displaced image are then compared and the displacements calculated. The fringe deflection technique uses vertical fringes in place of the randomly located dots.

1.4 Goals and Objectives

The research outlined in this Thesis is focused on the optimization of the Helmholtz Resonator for cooling of electrical circuits. Firstly, the optimization of a $PIV - BOS$ setup for the analysis of relatively small fields of view of approximately $1cm$ is carried-out. Secondly, the optimization of a Helmholtz resonator with one exit aperture is performed. The main objectives are:

- Numerical modeling of the BOS and FD techniques.
- Comparison of the Background Oriented Schlieren (BOS) and the Fringe Deflection (FD) techniques
- Experimental implementation and optimization of an FD set up for fields of view of around $1cm$, by using one camera.
- Measurement of temperature and velocity of fluid flows.
- Design and implement a Helmholtz device containing only one output.
- Design and develop a Matlab based program to implement the aforementioned objectives.

1.5 Research Methodology

The research methodology is shown in $Figure$ 1.5.1 as a flow chart, clearly showing the optical methods and techniques for data acquisition and clarifying the objectives of this research work.
The process starts with determining the parameters to be measured; the parameters could be refractive index, temperature or density. The process is divided into two parts: the numerical analysis, in which the algorithms for $PIV(BOS)$ and Fringe Deflection are developed. The other part concerns the preparation and development of the experimental procedures for the methods. The PIV technique is mainly studied because the BOS method uses the PIV algorithms. The BOS and the Fringe Deflection techniques are compared to determine which technique gives better results.

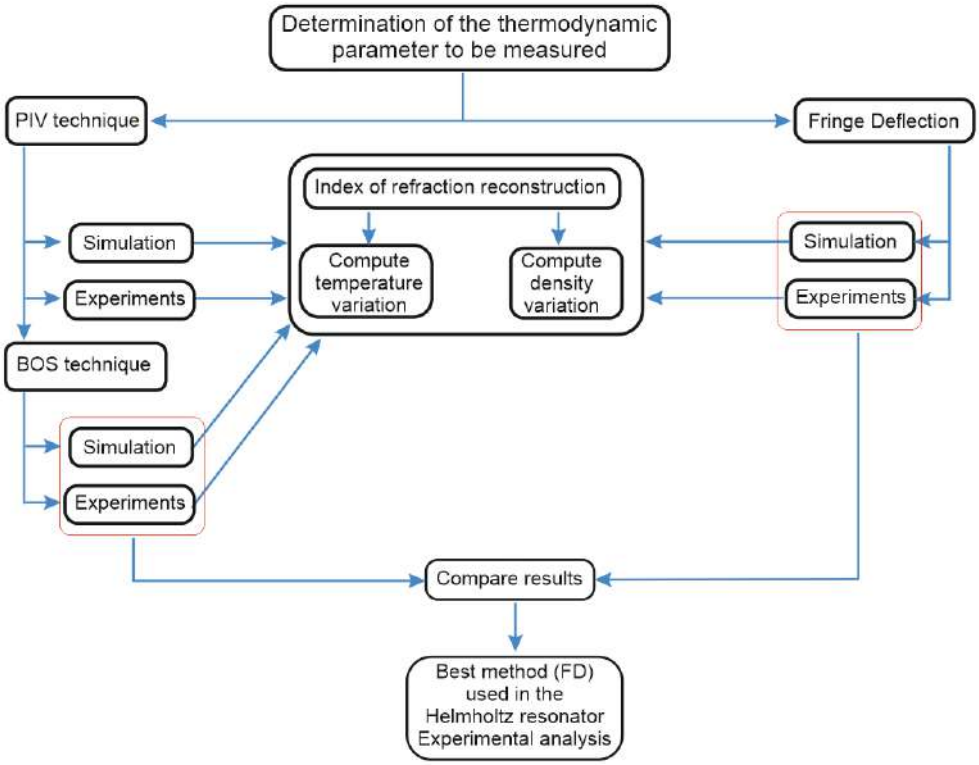

Figure 1.5.1: Flow diagram of the research methodology.

Based on the simulations and experimental analysis, the technique with the best results in terms of performance, error tolerance and robustness is then used in the analysis of the Helmholtz resonator.

1.6 Thesis Organization

This Thesis is divided into 7 Chapters, which are described in more detail below.
Chapter 1 contains the introduction to the Thesis document; back-ground and motivation, problem statement, technique analysis, research goals and objectives and the Thesis organization. Chapter 2 gives a more detailed theoretical background and the working principles of the techniques used, which are the Back-ground Oriented Schlieren (BOS) and the Fringe Deflection (FD). The chapter also outlines the Fermat's Principle and the Ray Deflection theory. The mathematical development for obtaining important variables for the BOS and the FD are formulated in this chapter. The phase difference, the refractive index gradient, together with the temperature derivations are formulated and the application of each technique is discussed.
Chapter 3 contains the literature review pertaining to the experiments and literature of this Thesis. Chapter 4 reports the results obtained by numerical simulation, which allows the selection of optimal parameters; a phase object with circular Gaussian distribution of refractive index is considered. In this Thesis research, 3 experimental investigations are carried-out, the set-up, procedure, results and analysis are documented in Chapter 5. The basic functions of the Helmholtz resonator are explained in Chapter 6. Also contained in Chapter 6 are the Helmholtz resonator results and the general discussions. Finally in Chapter 7, the summary and a list of potential gaps and challenges are presented to lay the foundation for future research and recommendations.

1.7 Summary of Main Results

The main results of this study are summarized below.

- Presented a new algorithm for deprojection of volumetric phase objects.
- Velocity measurement of a moving fluid by the Particle Image Velocimetry technique.
- Temperature measurement of a burning candle using the Background Oriented Schlieren and Fringe Deflection techniques.
- Helmholtz resonator analysis with Fringe Deflection technique.

Bibliography

[1] A. Blanco, B. Barrientos, and C. Mares, "Performance comparison of background-oriented schlieren and fringe deflection in temperature measurement, part 1: numerical evaluation.",Opt. Eng. , 55(5), 054102 (2016).

[2] A. Blanco, B. Barrientos, and C. Mares, "Performance comparison of background-oriented schlieren and fringe deflection in temperature measurement, part 2: experimental evaluation.", Opt. Eng. , 55(6), 064104 (2016).

[3] H. Richard, and M. Raffel, "Principle and applications of the Background Oriented Schlieren (BOS) method", Measurement Science and Technology 12 1576- 1585 (2001).

[4] N. A. Fomin, "Speckle photography for fluid mechanics measurements.", Springer - Verlag, Berlin (1997).

[5] A. H. Meier and T. Roesgen, "Improved background oriented schlieren imaging using laser illumination.", Exp. Fluid 54:1549 (2013).

[6] G. E. A. Meier, "Computerized background-oriented schlieren.", Exp. Fluids, 33, 181-187 (2002).

[7] N. A. Halliwell and C. J. D. Pickering, "Particle image velocimetry: a new field measurement technique, optical measurements in fluid mechanics.", Adam Hilger, 147-152, Bristol, U. K. (1985).

[8] D. B. Barker and M. E. Fourney, "Measuring fluid velocities with speckle pattern.", Opt. Lett., 1, 135-137 (1977).

[9] B. Barrientos, M. Cywiak, W.K. Lee, and P. Bryanston-Cross, "Measurement of dynamic deformation using a superimposed grating.", Rev. Mex. Fs. 50(1) 12-18 (2004).

[10] B. Barrientos, M. Cerca, J. Garcia-Marquez, and C. Hernandez-Bernal, "Three-dimensional displacement fields measured in a deforming granular-media surface by combined fringe projection and speckle photography.", J. Opt. A.: Pure Appl. Opt., 10, 104027, 10 (2008).

[11] B. Dalziel, G. Highes, and T. Sutherland, "Synthetic Schlieren", Proceedings of the 8th International Symposium on ow visualization, ed. G. M. Carlomagno, I. Grant, 62.1-62.6 (1998).

[12] B.S. Dalziel, G.O. Hughes, and B.R. Sutherland, "Whole-field density measurements by synthetic schlieren.", Exp. Fluids, 322-335 (2000).

[13] C. C. Landreth, J. R. Adrian, and C. S. Yao, "Double pulsed particle image velocimetry with directional resolution for complex flows.", Exp. Fluid, 6, 119-128 (1988).

[14] H. C. Van de Hulst, "Light scattering by small particles.", John Wiley and Sons (1957).

[15] E. Goldhahn and J. Seume, "The background oriented schlieren technique: Sensitivity, accuracy, resolution and application to a three-dimensional density field.", Exp. Fluids, 43: 241-249 (2007).

[16] G.E. Elsinga, B.W. Van Oudheusden, F. Scarano, and D. W. Watt, "Assessment and application of quantitative schlieren methods: Calibrated color schlieren and background oriented schlieren.", Exp. Fluids 36, 309-325 (2004).

[17] R. J. Adrian, "Scattering particle characteristics and their effect on pulsed laser measurements of fluid flow: speckle velocimetry vs particle image velocimetry.", App. Opt. 23, 1690-1691 (1984).

[18] H. J. Huang and A. M. Waas, "Improved speckle method for measuring in-plane displacement and strain fields.", Opt. Eng. 46(5), 051005 (2007).

[19] J. Szinitman and T. Rosgen, "Whole-eld density visualization and abel reconstruction of axisymmetry vortex rings. J. Flow Visual.", Im. Process. 13, 343-358 (2006).

[20] M. Raffel, C. Willert, and J. Kompenhans, "Particle image velocimetry, a practical guide.", Springer - Verlag, Berlin (1998).

[21] N. Vinnicheko, A. Uvarov, and Y. Plaksina, "Accuracy of background oriented schlieren for different background patterns and means of refraction index reconstruction.", 15th International Symposium on flow visualization, Minsk, Belarus (2007).

[22] S. Debrus, M. Francon, C. Grover, M. May, and M. Roblin, "Ground glass differential interferometer.", App. Opt. 11(4), 853-857 (1972).

[23] U. Kopf, "Application of speckling for measuring the deflection of light by phase objects.", Opt. Comm. 5(5), 347-350 (1972).

Chapter 2

Background

Contents

The physical basis for Schlieren images stems from Snell's law, which states that light slows down when it interacts with matter. When a medium is homogeneous, as in a vacuum or space, light propagates uniformly, at a constant speed. When an inhomogeneous medium such as moving liquids is encountered, the light rays are refracted and deflected from their uninterrupted path. $Figure\,2.0.1$ displays the principles of the Snell's Law [1].

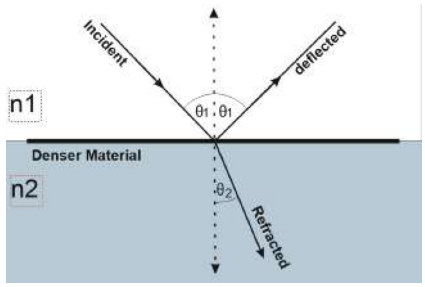

Figure 2.0.1: Principle of Snell's Law.

In $Figure\,2.0.1$, n_1 and n_2 represent the indices of refraction for the two media, and θ_1 and θ_2 are the angles of incidence and refraction that the ray makes with the normal (perpendicular) line at the boundary. Snell's law asserts that:

$$\frac{n_1}{n_2} = \frac{sin\theta_2}{sin\theta_1}. \tag{2.0.1}$$

Snell's law has extreme/exceptional cases, the first involving an incoming angle of zero $0°$, in which case the transmitted light propagates without distortion; the second is related to full reflection, which means all light is reflected. The second phenomenon occurs when the ratio $\frac{n_2}{n_1}$ multiplied by the angle of incidence is greater than one. The focus of this work is the concept of light rays deviating from a straight line when passing through a medium with a different refractive index.

To apply an appropriate quantitative analysis to the Schlieren optical system, the following rules and equations governing Schlieren images are described; Wave Motion, Fermat's Principles, Refractive Index, Ray Deflection, Particle Image Velocimetry (PIV), the Background Oriented Schlieren (BOS) and Fringe Deflection (FD).

2.1 Wave Motion

Most optical systems use light to illuminate the object to be analysed, therefore a mathematical description of light as a wave and its propagation is given, considering terms such as wavelength, frequency, wavefronts etc.

A monochromatic light wave, which propagates in a vacuum, can be generated from the equation:

$$\vec{E}(\vec{r},t) = a(\vec{r})cos[\phi(\vec{r}) - \omega t], \tag{2.1.1}$$

where $\vec{E}(\vec{r},t)$ is the vector of the intensity of the electric field at a given point in space $\vec{r} = r(x,y,z)$ and at a given time t, $\phi(\vec{r})$ is the initial phase of the wave at that point and ω is the angular frequency of the oscillations. The angular frequency is consistent with the following relationships

$$\omega = 2\pi\nu = \frac{2\pi}{T} = \frac{2\pi c}{\lambda_0}, \tag{2.1.2}$$

where ν is the frequency, T is the period of oscillation, λ_0 is the wavelength in vacuum, and c is the speed of

light in vacuum. If the light travels is a medium, the index of refraction of the medium is given by

$$n = \frac{c}{v}, \tag{2.1.3}$$

where v is the speed of light in the medium of propagation, which has the following relationship because it is a wave:

$$c = \lambda\nu, \tag{2.1.4}$$

where λ is the wavelength in the medium and ν is the frequency of oscillation [4]. It is remarkable that the frequency remains constant regardless of the medium. This ratio also applies to multiplication constrained in vacuum. Combining $Eq.(2.1.3)$ and $Eq.(2.1.4)$, results in:

$$\lambda = \frac{\lambda_0}{n}. \tag{2.1.5}$$

A light wave is also characterized by a $k-$wave vector, whose amplitude is determined by;

$$k = \frac{2\pi}{\lambda}. \tag{2.1.6}$$

then $k \cdot v$ is in radians of phase, with 2π radians to the wavelength. The wave vector, normal to the wave fronts, indicates the direction of propagation of a light ray only if the medium is isotropic. The next section describes the path that a ray of light travels according to Fermat's principles.

2.2 Fermat's Principles

A modern Fermat's principle states that the light path that goes from one point to another is such that the time it takes is stationary in relation to the variations of possible paths. In other words, the time it takes for light to travel a distance s in a specific medium is given by;

$$t = \frac{s}{v}, \tag{2.2.1}$$

where s is the distance traveled. The speed v is assumed to be constant throughout the medium, regardless of the direction of travel in the medium. If the refractive index according to $Eq.(2.1.3)$ is used, the result is:

$$t = \frac{sn}{c}, \tag{2.2.2}$$

when a medium in which the index of refraction depends on the position $n = n(s)$ is considered, then an estimate can be made that a differential element ds is traversed in a time lapse $dt = \frac{n}{c}ds$. The total time between two arbitrary chosen points E and F is;

$$t = \frac{1}{c}\int_E^F n(s)ds. \tag{2.2.3}$$

Then, according to Fermat's principle, the extreme values of the function are given as [6]:

$$\delta \int_E^F n(s)ds = 0, \tag{2.2.4}$$

where δ denotes a small variation. Fermat's principle, as shown in $Eq.(2.2.4)$, involves the integration of the index of refraction, discussed in the next section.

2.3 Refractive Index of a Phase Object

A light ray which orthogonally traverses a change in the refractive index experiences a change in phase velocity, but continues to travel in the same direction. The refractive index may be expressed as $n(x, y) = n_0 + \triangle n(x, y)$ where n_0 is the index of refraction of the reference state and $\triangle n(x, y)$ is the local variation of the refractive index with respect to n_0. The ideal gas equation is given by:

$$pV = n_m RT, \tag{2.3.1}$$

where T is the temperature, p is the atmospheric pressure, V is the volume of the gas, n_m is the number of moles contained in said volume of gas and R is the universal gas constant. The total ray deflection results from the refractive index density integrated along the optical path. The Gladstone-Dale equation relates the refractive index to the density of a gas and is given by:

$$n - 1 = K\rho, \tag{2.3.2}$$

where K is the Gladstone-Dale constant for air, which weakly depends on the wavelength of light [5], ρ is the density. K is dependent on gas composition, temperature, and the wavelength of the light passing through the medium. In gases K is typically between 0.1×10^{-3} and 1.5×10^{-3} $(kg/m^3)^{-1}$. $K\rho$ is therefore much smaller than 1, so the refractive index varies only in the third or fourth decimal place. Hence very sensitive optics are required to detect changes in density. The temperature can be expressed as:

$$T = \frac{PV}{n_m R}. \tag{2.3.3}$$

The volume of a gas can be expressed as a function of density based on the expression:

$$V = \frac{m}{\rho}, \tag{2.3.4}$$

where m is the mass of the gas. The temperature can be written as follows:

$$T = \frac{PM}{R\rho}, \tag{2.3.5}$$

where $M = \frac{grams}{mole}$ is the molar mass of the gas. Using the Gladstone-Dale equation, temperature can be expressed as:

$$T = \frac{PMK}{R(n-1)}, \tag{2.3.6}$$

To find the value of the initial refractive index n_0, consider $Eq.(2.3.6)$ for another temperature value:

$$T_0 = \frac{PMK}{R(n_0 - 1)}. \tag{2.3.7}$$

The temperature equation is obtained as:

$$T = T_0 \frac{(n_0 - 1)}{(n - 1)}, \tag{2.3.8}$$

Solving for n_0:

$$n_0 = T \frac{(n - 1)}{T_0} + 1, \tag{2.3.9}$$

On substituting the Gladstone-Dale, $Eq.(2.3.9)$ can be written as:

$$n_0 = \frac{KP_0M}{T_0R} + 1, \tag{2.3.10}$$

where P_0 is the atmospheric pressure of the medium in which the measurements are carried out. By considering the change of refractive index, $\triangle n$, the refractive index of a phase object can be expressed as following:

$$n = n_0 + \triangle n. \tag{2.3.11}$$

Finally, the density can be written as:

$$\rho = \frac{n - 1}{K}. \tag{2.3.12}$$

The next section discusses how a beam of light is deflected when it comes into contact with a medium with a different index of refraction or a phase object.

2.4 Ray Deflection

The relationship between the curvature of the refracted ray and the amplitude of the corresponding refractive index can be deduced from the schematic representation shown in $Figure\,2.4.1$. The following assumptions are used in the derivation [31]:

- The test area is exposed to uniform parallel illumination in the $x-y$ plane without any change in illumination in the $z-$plane.
- Within the schlieren object, the displacement of a ray of light from its rectilinear path is negligible.
- There is no gradient change in either the $x-$ or $z-$ directions, $\frac{dn}{dx} = 0$ and $\frac{dn}{dz} = 0$.
- Only a negative vertical refractive index gradient, $\frac{dn}{dy} < 0$, in the $y-$ direction between z_1 and z_2.

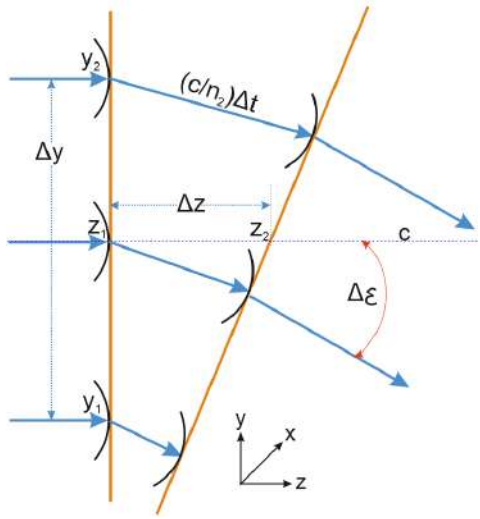

Figure 2.4.1: Deflection of the light-ray through refractive-index gradient.

A planar light wave, indicated by brown lines in $Figure\ 2.4.1$, initially vertical, becomes displaced after propagating through a schlieren object. It can be seen that the planar wavefront of light is initially vertical as it passes through z_1. As the wave crosses the schlieren object from z_1 to z_2, it moves in the differential time $\triangle t$ by the distance $\triangle z$ and is refracted by the angle $\triangle \varepsilon$. Therefore, it can be written as follows:

$$\triangle \varepsilon = \frac{\frac{c}{n_2} - \frac{c}{n_1}}{\triangle y} \triangle t. \tag{2.4.1}$$

and the differential time can be expressed further as follows:

$$\triangle t = \triangle z \frac{n}{c}. \tag{2.4.2}$$

Combining $Eq.(2.4.2)$ with $Eq.(2.4.1)$ yields:

$$\triangle \varepsilon = \frac{n}{c} \frac{\frac{c}{n_2} - \frac{c}{n_1}}{\triangle y} \triangle z. \tag{2.4.3}$$

Upon simplification, the angle can be expressed as:

$$\triangle \varepsilon = \frac{n}{n_1 n_2} \frac{n_1 - n_2}{\triangle y} \triangle z. \tag{2.4.4}$$

The term $\frac{n}{n_1 n_2}$ can be simplified to $\frac{1}{n}$ in the limit as $\triangle y$ approaches 0. Letting all finite differentials approach zero, we get:

$$\frac{d\varepsilon}{dz} = \frac{1}{n} \frac{dn}{dy}. \tag{2.4.5}$$

Since the angle ε is very small, it can be estimated and approximated to be the slope of the refracted beam. By implementing this and taking into account other refractive index gradients, it is possible to obtain a relationship between the curvature of the refracted beam and the amplitude of the refractive index gradient. Small angle approximation is used to postulate $d\varepsilon$ is equal to $\frac{dy}{dz}$, which results in [4]:

$$\frac{d^2y}{dz^2} = \frac{1}{n}\frac{\partial n}{\partial y}, \tag{2.4.6}$$

relating the curvature of a refracted ray to the magnitude of the refractive index gradient. A similar expression can be obtained for x curvature, given by:

$$\frac{d^2x}{dz^2} = \frac{1}{n}\frac{\partial n}{\partial x}, \tag{2.4.7}$$

Schlieren images can be found by integrating the curvature of the light ray in optical inhomogeneities in the appropriately specified direction:

$$\varepsilon_y = \frac{1}{n}\int \frac{\partial n}{\partial y} dz, \tag{2.4.8}$$

and

$$\varepsilon_x = \frac{1}{n}\int \frac{\partial n}{\partial x} dz, \tag{2.4.9}$$

$Eqs.(2.4.6)$ and $(2.4.7)$ show that the bending of the ray is not caused by the refractive index n, but rather by the gradient $\left(\frac{dn}{dy}\right.$ and $\left.\frac{dn}{dx}\right)$ of this refractive index. Furthermore, $Eqs.(2.4.8)$ and $(2.4.9)$ show light ray deflections bend towards regions of higher refractive index.

Ray Equation from Fermat's Principle.

The time it takes for light to travel a distance d is equal to $t = \frac{d}{v} = \frac{nd}{c}$. Thus it is proportional to the product nd, known as the optical path length. As discussed in section 2.2, Fermat's principle states that the path taken by a ray between two given points is the path that can be traveled in the least time. The time of flight is given by the integral:

$$T = \int \frac{ds}{v}, \tag{2.4.10}$$

where T is the time, ds is the infinitesimal arc length (the distance between two infinitely nearby points along the path). Rewriting the time of flight gives:

$$T = \frac{1}{c}\int n\left[\vec{x}(s)\right] ds. \tag{2.4.11}$$

The dependence on the arc length s is indicated. Following the usual variational approach by varying the path of the light ray from $\vec{x}(s)$ to $\vec{x}(s) + \delta\vec{x}(s)$ with fixed endpoints. δ indicates a variation in the path. The standard variation principle deals mainly with path minimization and defines the following equations [32]:

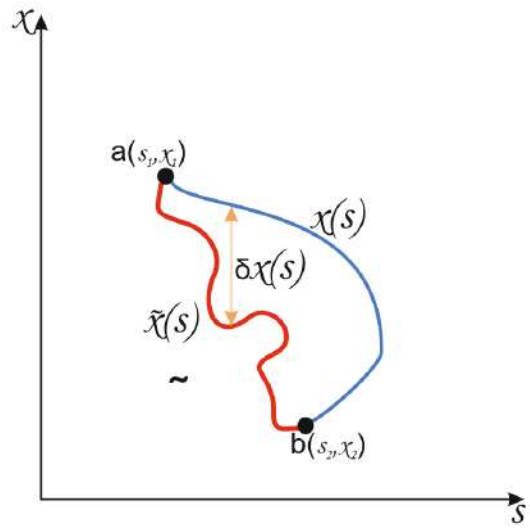

Figure 2.4.2: Cartesian plane to demonstrate the variational approach.

$$I_d = \int_a^b ds = \int_a^b \sqrt{1+y'^2}dx. \tag{2.4.12}$$

and

$$I_t = \int_a^b ds = \int_a^b \frac{\sqrt{1+y'^2}}{v}dx. \tag{2.4.13}$$

$Eq.(2.4.12)$ minimizes the distance between two arbitrary points a and b, while $Eq.(2.4.13)$ minimizes the time. I_d and I_t are the integrals to be minimized. The calculus of variations finds a path or a function that minimizes another function, while the differential calculus finds a point that minimizes a function.
The first order variation in the flight time is then given by:

$$\delta T = \frac{1}{c}\int \delta n\left[x(s)\right] ds. \tag{2.4.14}$$

Consider:

$$\delta n = n\left[s, x(s)+\delta x(s), x^{'}(s)+\delta x^{'}(s)\right], \tag{2.4.15}$$

Expanding $Eq.(2.4.15)$ in a Taylor series gives:

$$n\left(s, x+\delta x, x^{'}+\delta x^{'}\right) = n\left(s, x, x^{'}\right) + \frac{\partial n}{\partial x}\delta x + \frac{\partial n}{\partial x^{'}}\delta x^{'} + \Theta(\delta^2). \tag{2.4.16}$$

Substitute $Eq.(2.4.16)$ into $Eq.(2.4.14)$:

$$\frac{1}{c}\int_a^b n\left(s, x+\delta x, x^{'}+\delta x^{'}\right) ds = \frac{1}{c}\int_a^b n\left(s, x, x^{'}\right) ds + \frac{1}{c}\int_a^b \left(\frac{\partial n}{\partial x}\delta x + \frac{\partial n}{\partial x^{'}}\delta x^{'}\right) + \frac{1}{c}\int_a^b \Theta\left(\delta^2\right) ds, \tag{2.4.17}$$

$$\tilde{T} - T = \int_a^b \left(\frac{\partial n}{\partial x}\delta x + \frac{\partial n}{\partial x^{'}}\delta x^{'}\right) + \int_a^b \Theta\left(\delta^2\right) ds, \tag{2.4.18}$$

where $\tilde{T} = \frac{1}{c}\int_a^b n\left(s, x+\delta x, x^{'}+\delta x^{'}\right) ds$ is the varied path, and $T = \frac{1}{c}\int_a^b n\left(s, x, x^{'}\right) ds$ is defined as in $Eq.(2.4.11)$. According to the definition of the first variation of the functional, T is defined by:

$$\delta T = \tilde{T} - T. \tag{2.4.19}$$

There

$$\delta T = \int_a^b \left(\frac{\partial n}{\partial x}\delta x + \frac{\partial n}{\partial x^{'}}\delta x^{'}\right). \tag{2.4.20}$$

where $\int_a^b \Theta\left(\delta^2\right) ds$ is omitted because only the first-order terms are taken into account. Integrating the 2nd term in $Eq.(2.4.20)$ by parts and considering the fact that $x^{'} = \frac{dx}{ds}$ and $\partial x' = \frac{d(\delta x)}{ds}$, also noting that $\delta x(a) = \delta x(b) = 0$, results in:

$$\delta T = \int_a^b \frac{\partial n}{\partial x}\delta x - \int_a^b \frac{dx}{ds}\left[n\frac{d(\delta x)}{ds}\right] ds. \tag{2.4.21}$$

Variational principles requires that the endpoints be zero, δx, so the 2nd term in $Eq.(2.4.21)$ falls away.

$$\delta T = 0 = \int \left[\frac{\partial n}{\partial x} - \frac{d}{ds}\left(n\frac{dx}{ds}\right)\right] \delta x ds. \tag{2.4.22}$$

Applying the fundamental lemma of Variational Calculus gives [32]:

$$\nabla n - \frac{d}{ds}\left(n\frac{dx}{ds}\right) = 0 \tag{2.4.23}$$

In an inhomogeneous medium, the refractive index $n(\vec{r})$ is a function of the position $r(x, y, z)$, where ds is the difference length element along the path. The time it takes for light to travel from a to b is proportional to the length of the optical path. Taking into account the paraxial propagation of the ray in the $z-$direction, $Eq.(2.4.23)$ can be split into two equations. For the $x-$curvature, the equation is given as:

$$\frac{d^2x}{dz^2} = \frac{1}{n}\frac{\partial n}{\partial x}, \tag{2.4.24}$$

A similar equation for $y-$curvature is given by:

$$\frac{d^2y}{dz^2} = \frac{1}{n}\frac{\partial n}{\partial y}. \tag{2.4.25}$$

The deviation from a straight-line trajectory ε_x of the light ray at the point (x, y), which is generated by the presence of a phase object, can be calculated by integrating $Eq.(2.4.24)$ once with respect to the variable z.
The deflection ε_x is given by:

$$\varepsilon_x = \left(\frac{dx}{dz}\right)_{z2} = \frac{\triangle x}{D} = \frac{1}{n_0}\int_{z1}^{z2}\left(\frac{\partial(\triangle n)}{\partial x}\right)_{\vec{r}} dz, \tag{2.4.26}$$

and

$$\varepsilon_y = \left(\frac{dy}{dz}\right)_{z2} = \frac{\triangle y}{D} = \frac{1}{n_0}\int_{z1}^{z2}\left(\frac{\partial(\triangle n)}{\partial y}\right)_{\vec{r}} dz, \tag{2.4.27}$$

where $n(x,y) = n_0 + \triangle n(x,y)$ which is then replaced in the denominator by n_0 the index of refraction of the reference, $\triangle n(x,y)$ is the local variation of the refractive index with respect to n_0, since in most practical cases $n \approx n_0$; D is the object-to-background distance, and $\triangle x$ and $\triangle y$ correspond to the apparent displacement of an image point due to the presence of the object, in the $x-$and $y-$directions, respectively. The inclinations of the rays $\left(\frac{dx}{dz}\right)_{z1}$ and $\left(\frac{dy}{dz}\right)_{z1}$ at the entrance to the observation region were also assumed to be zero. After the apparent displacements have been measured, the projected index of refraction can be reconstructed. Assuming that the change in refractive index under consideration is due to temperature changes, the projected temperature field can be calculated using $Eq.(2.3.8)$.

2.4.1 Refractive Index Reconstruction

Most of the optical systems used to measure temperature produce the refractive index in the form of displacements, $\triangle x$ and $\triangle y$. Displacement values measured using $Eqs.$(2.4.26) and (2.4.27) correspond to line-of-sight integrated values of the index of refraction. Standardized tomographic techniques are used to recover the corresponding $3D$ distribution of the refractive index. For the case of a Gaussian distribution of the refractive index, this one-to-one correspondence is straightforward. The refractive index is expressed as:

$$\triangle n = (-1) \times (\triangle n_0) exp\left(-C\frac{y}{L_y}\right) exp\left(-\frac{(x-x_0)^2 + (z-z_0)^2}{r_0^2}\right), \tag{2.4.28}$$

where $\triangle n_0$ is the maximum variation of the refractive index at the center of the phase object,r_0 and (x_0, y_0) are the radius and coordinates of the center of the circular Gaussian function, respectively, L_y is the vertical size of the observation area in the $y-$direction. The function given by $Eq.$(2.4.28) resembles the plume of a candle, and is shown in $Figure$ 4.2.4(a). The factor C in the exponential term is a constant that is used to vary the rate of change of the refractive index in the $y-$direction. By substituting $Eq.$(2.4.28) into $Eq.$(2.4.26), the horizontal displacement function projected onto the $xy-$plane of the sensor is obtained to be;

$$\triangle x = \frac{\sqrt{\pi} r_0 D}{n_0}\frac{\partial \triangle n^{'}}{\partial x} = \frac{2\sqrt{\pi}\triangle n_0 D}{n_0 r_0}(x-x_0) exp\left(-C\frac{y}{L_y}\right) exp\left(-\frac{(x-x_0)^2}{r_0^2}\right), \tag{2.4.29}$$

which is a particular form of the Gaussian function, where

$$\triangle n^{'} = -\triangle n_0 \times exp\left(-C\frac{y}{L_y}\right) exp\left(-\frac{(x-x_0)^2}{r_0^2}\right), \tag{2.4.30}$$

is a function without n_0 dependency in z. It can be noted that the original Gaussian radius is preserved and that the effect of the line integral corresponds to a constant given by $\sqrt{\pi} r_0$; it is also assumed that the size of the object is completely enclosed by the area of observation: $Lx > 4r_0$, where Lx is the horizontal size of the region in the $x-$direction. So if the measured profile of the displacements along the $x-$direction for a certain y_0 happens to be the derivative of a Gaussian function, then the $\frac{\partial \triangle n^{'}}{\partial x}$ can easily be obtained from the first equality of $Eq.$(2.4.29), and thus the use of a de-projection algorithm can be avoided. The vertical displacement component, $\triangle y$, can be found similarly as follows;

$$\triangle y = \frac{\sqrt{\pi} r_0 D}{n_0}\frac{\partial \triangle n^{'}}{\partial y} = \frac{2Cr_0\sqrt{\pi}\triangle n_0 D}{n_0 L_y} exp\left(-C\frac{y}{L_y}\right) exp\left(-\frac{(x-x_0)^2}{r_0^2}\right). \tag{2.4.31}$$

The factor C can be chosen so that the maximum displacements in the $x-$ and $y-$ directions are the same. $Figure$ 4.2.4(b) shows a typical displacement function that is obtained from $Eqs.$(2.4.29) and (2.4.31). When the $x-$ and the $y-$displacement fields are added to the position of the spatial structures of the reference image,

it produce the displaced image, which can be used for numerical simulation purposes (discussed in further detail in Section 4.3).

There are two ways to recover the refractive index from the density variation caused by the presence of a phase object. To demonstrate the reconstruction process, consider the Table 2.1 shown below. The two procedures are labeled Procedure 1 ($P1$) and Procedure 2 ($P2$).

Procedure 1 uses integration of $\triangle x$ to recover $\triangle n$ (as depicted in point number 7 in the table), while procedure 2 uses the values of x to divide $\triangle x$. x represents the values at which $\triangle x$ is spread along the $x-$direction. The $P2$ procedures avoids the integration process.

Procedure 1 (P1)	**Procedure 2 (P2)**
1. $\triangle n_{original} = \triangle n_0 exp\left(-C\frac{y}{L_y}\right) exp\left(-\frac{(x-x_0)^2+(z-z_0)^2}{r_0^2}\right)$	
2. $\triangle x = \frac{1}{n_0} D \int (\frac{\partial(\triangle n)}{\partial x}) dz$	
3. $\triangle x = \frac{1}{n_0} D \frac{\partial}{\partial x} \int (\triangle n) dz$	
4. $\frac{\triangle x}{D} = \frac{1}{n_0}\frac{\partial}{\partial x}\triangle n_0 \sqrt{\pi} r_0 exp\left(-C\frac{y}{L_y}\right) exp\left(-\frac{(x-x_0)^2}{r_0^2}\right)$	
5. $\frac{\triangle x}{D} = \frac{\sqrt{\pi} r_0}{n_0}\frac{\partial}{\partial x}(\triangle n)$	5. $\frac{\triangle x}{D} = \frac{\sqrt{\pi} r_0}{n_0}\triangle n_0 exp\left(-C\frac{y}{L_y}\right)(\frac{-2x}{r_0^2}) exp\left(-\frac{(x-x_0)^2}{r_0^2}\right)$
6. $\triangle n_{recovered} = \int (\frac{\triangle x}{D} n_0 \frac{1}{r_0}\frac{1}{\sqrt{\pi}})\, dx$	6. $\frac{\triangle x}{D} = -\frac{2\sqrt{\pi}}{n_0 r_0} x \left[\triangle n_0 exp\left(-C\frac{y}{L_y}\right) exp\left(-\frac{(x-x_0)^2}{r_0^2}\right)\right]$
7. $\triangle n_{recovered} = \frac{1}{D} n_0 \frac{1}{\sqrt{\pi}}\frac{1}{r_0}\int (\triangle x)\, dx$	7. $\triangle n_{recovered} = -\frac{\triangle x r_0}{2xD\sqrt{\pi}}$

Table 2.1: Refractive index re-construction

In step 1, the Gaussian distribution change in refractive index equation is displayed. In step 2, the apparent change in displacement ($\triangle x$) along the $x-$direction is displayed. $\triangle x$ is the transverse displacement of a ray. Step 3 states that if the rate of change of $\triangle n$ is continuous, then, the integral and the differentiation can be exchanged. In step 4, the equation for $\triangle n$ is substituted and the integral computed. Steps 1 to 4 are the same for both methods. Step 5 of Procedure 1, substituted $\triangle n$ in place of $(\triangle n_0)\sqrt{\pi} r_0 exp\left(-C\frac{y}{L_y}\right) exp\left[-\frac{(x-x_0)^2}{r_0^2}\right]$, and step 6 integrated both sides and make $\triangle n$ the subject of the formula. In step 7, all variables are constants with the exception of $\triangle x$, which remains in the sign of the integration. Therefore, step 7 of Procedure 1 indicates that the integral of $\triangle x$ must be taken in order to reconstruct the change in index of refraction. It should be emphasized that the FD technique produces a change in phase $\triangle\phi$. To get $\triangle x$, the formula:

$$\triangle x = \left(\frac{\Delta\phi}{2\pi} P\right), \tag{2.4.32}$$

is used, where $P = \frac{1}{f_0}$ is the period of sinusoidal fringes (grating). In procedure 2, instead of integrating, $\triangle x$ is divided by x to get $\triangle n$.

It is noted that dividing by x is relatively easier since the integration process is omitted but poses challenges when x approaches zero (0) from both sides, because dividing by zero (0) results in an infinity or undefined expression. This fact will be demonstrated and explained further in the experimental section.

2.5 Relationship Between Temperature and Displacement

Since the accuracy of BOS is affected by the range of displacement values, an analysis of the relationship between this parameter and temperature is important. From the Gaussian variation of the refractive index, given by $Eq.(2.4.28)$, the maximum $x-$component is attained when

$$x = \frac{r_0}{\sqrt{2}}, \tag{2.5.1}$$

Using $x_0 = 0$ and $y = 0$, $Eq.(2.4.29)$ gives the maximum displacement $\triangle x_{MAX} = \frac{1.5 \times D \triangle n_0}{n_0}$. Taking into account $Eq.(2.3.8)$, and $Eq.(2.3.11)$:

$$T = T_0 \frac{(n_0 - 1)}{(n_0 + \triangle n_0 - 1)}. \tag{2.5.2}$$

Making $\triangle n_0$ the subject of the formula leads to:

$$\triangle n_0 = \left(\frac{T_0}{T} - 1\right)(n_0 - 1). \tag{2.5.3}$$

Substituting for $\triangle n_0$ in $\triangle x_{MAX} = \frac{1.5 \times D \triangle n_0}{n_0}$ leads to:

$$\triangle x_{MAX} = \frac{1.5 \times D}{n_0}\left(\frac{T_0}{T} - 1\right)(n_0 - 1), \tag{2.5.4}$$

with $T_0 = 25°C$ and $n_0 = 1.00022$. From $Eq.(2.4.29)$, it can be seen that Δx_{MAX} is directly proportional to D, which implies that larger values of D in $Eq.(2.4.29)$ results in larger values of Δx_{MAX}. D is the distance from the object to the background. The displacement value can be processed correctly using the BOS technique.
The refractive index decreases with increasing temperature. Therefore, the lowest refractive index in the middle of the candle flame (shown in $Figure$ 4.3.2) corresponds to the highest center-line temperature.
The following section introduces the error calculation formulas for the simulation results.

2.6 Error Computation

Every measurement involves an uncertainty known as an error. Errors in experimental measurements are caused by unknown, and unpredictable changes in experiments. These changes may occur in the measurering insteruments or in the environmental conditions.

2.6.1 RMS error

The RMS error for the numerical results is calculated by considering the given displacements $(\triangle x_g, \triangle y_g)$ and the computed (simulated) displacement values $(\triangle x_c, \triangle y_c)$. The error in calculating the $x-$displacements component can be expressed as:

$$e_x = \sqrt{\frac{\sum_{i=1}^{N}(\triangle x_{i,c} - \triangle x_{i,g})^2}{N}}, \tag{2.6.1}$$

where N is the total number of displacement vectors. An expression similar to $Eg.(2.6.1)$ can be used for the error in the $y-$displacements:

$$e_y = \sqrt{\frac{\sum_{i=1}^{N}(\triangle y_{i,c} - \triangle y_{i,g})^2}{N}}. \tag{2.6.2}$$

The corresponding relative errors can be found by dividing $Eq.(2.6.1)$ by $max(\triangle x_g)$, where $max(\cdot)$ is a function that extract the maximum value of the argument. In addition, the total relative error can be determined as

$$e = \frac{\sqrt{e_x^2 + e_y^2}}{max(\triangle_g)}, \tag{2.6.3}$$

where $\triangle_g = \sqrt{\triangle x_g^2 + \triangle y_g^2}$
These formulas are extensively used for the errors evaluation, which is discussed in the next section.

2.6.2 Added Noise

To test the performance and accuracy of the algorithms developed, noise was added to the images. The added noise is determined as follows:

$$Noise = (\frac{added\ error}{100})/2 \times \triangle n_0 - (\frac{added\ error}{100}) \times \triangle n_0 \times random\left[size(\triangle n)\right], \tag{2.6.4}$$

where $added\ error$ is varied from 1 to 150, generating random noise ranging from 1% to 150% errors. After adding the errors, the respective parameters are reconstructed using the correlation method in the BOS technique and the Fourier method in the Fringe Deflection technique. The equation used to generate the noise for the FD technique is similar to $Eq.(2.6.4)$, but the noise is through π instead of $\triangle n_0$ as in BOS analysis:

$$Noise = (\frac{added\ error}{100})/2 \times \pi - (\frac{added\ error}{100}) \times \pi \times random\left[size(\triangle n)\right], \tag{2.6.5}$$

Errors are computed to evaluate the performance and robustness of the developed algorithms.

2.7 Radius Calculation

To reconstruct the $3D$ from the $2D$ distribution map, a Gaussian function of the form:

$$f(x, y) = A(x - x_0)exp\left[-\frac{(x - x_0)^2}{B^2}\right], \tag{2.7.1}$$

is fitted in each line of the reconstructed $\triangle x$ map. In $Eq.(2.7.1)$, A is the amplitude , x_0 is the centroid and B is the radius to be reconstructed by curve fitting, which is similar to r_0. After these values have been calculated, the Gaussian distribution can be reconstructed numerically, taking into account that the radius r_0 in $Eq.(2.4.28)$ has to be calculated for each row. A $3D$ reconstruction is possible, since the radius in $3D$ is the same as in $2D$ extended to the 3rd axis.

2.8 Interpolation

Due to the nature of a CCD camera, a captured image becomes pixelated and thus discretized. Since the image domains are discretized, the discrete cross-correlation domain only exists at integer values. This means that the maximum value within the cross-correlation domain, which corresponds to particle displacement within the interrogated area, is at best measured to an integer value with an uncertainty of ± 0.5 pixels. Various methods

have been used in the past to estimate the location of the correlation peak, in an attempt to obtain sub-pixel accuracy.

2.8.1 Sub-pixel Interpolation

Sub-pixel interpolation is an accepted procedure to refine interpolating the correlation map in the neighbourhood of the maximum to achieve sub-pixel accuracy. Simulation data can be used to quantify the achievable accuracy for a particular image setup. One common approach is to fit the correlation data to a function that uses only three neighbouring values to estimate a component of displacement. The Gaussian peak fitting, shown in $Tab.(2.2)$, is the most commonly used three-point estimator. The reasonable explanation for this is that the particle images themselves, when properly focused, describe Airy intensity functions that are very well approximated by a Gaussian intensity distribution.

The following procedure is used to detect a correlation peak and get an accurate sub-pixel displacement estimate:

Step 1: Scan the correlation plane $R = R_{II}$ for the maximum correlation value $R_{(i,j)}$ and store its integer coordinates (i, j).

Step 2: Extract the adjoining four correlation values: $R_{(i-1,j)}$, $R_{(i+1,j)}$, $R_{(i,j-1)}$ and $R_{(i,j+1)}$.

Step 3: Use three points in each direction to apply the three point estimator, generally the Gaussian curve formula shown in Table 2.2 is used.

If the highest point in the correlation plane is $R_{(i,j)}$, its closest neighbours are $R_{(i-1,j)}, R_{(i+1,j)}, R_{(i,j-1)}$ and $R_{(i,j+1)}$. A curve is fitted to the three points in the $x-$ direction, and the maximum value of this curve is assumed to be at the $x-$coordinate of the correlation peak. This process is repeated for the y coordinate.

Curve-fitting Function	Three-point Estimators
$f(x,y) = A\, exp\left[\frac{-(x_0-x)^2}{B^2}\right]$	$x_0 = \frac{ln\, R_{(i-1,j)} - ln\, R_{(i+1,j)}}{2ln\, R_{(i-1,j)} - 4ln\, R_{(i,j)} + 2ln\, R_{(i+1,j)}}$ $y_0 = \frac{ln\, R_{(i,j-1)} - ln\, R_{(i,j+1)}}{2ln\, R_{(i,j-1)} - 4ln\, R_{(i,j)} + 2ln\, R_{(i,j+1)}}$

Table 2.2: Three-point estimators used to achieve sub-pixel resolution. The indices (i, j) corresponds to the spatial location of the maximum location of the correlation value within the correlation domain.

In the curve-fitting function $f(x,y) = A\, exp\left[\frac{-(x_0-x)^2}{B^2}\right]$, A is defined as the amplitude, x_0 is the centroid (location), and B is the radius (peak width).

The assumption that the correlation peak is Gaussian implies that the original particle images are Gaussian. With sub-pixel interpolation, there is still a residual effect that biases the displacement estimate towards integer values, therefore, it is recommended to use a suitable image interpolation method in order to avoid or minimize the loss of information.

The next section deals with the PIV method and its application to this Thesis work. The PIV method determines the displacement of particles in a fluid flow.

2.9 Particle Image Velocimetry

This Chapter provides a general description and theory of Particle Image Velocimetry (PIV). A detailed description of the technique in its entirety is not given here, rather it is detailed as is relevant to its application in the

current investigation.

PIV is a full-field experimental technique used to perform velocity measurements and flow patterns within a fixed geometry [7]. The basic requirements for a PIV system are an optically transparent test section, an illuminating light source (laser), a recording medium (camera) and a computer for image processing. PIV is a non-intrusive measurement technique with highly developed optical and electronic instruments, which is applied to experimental fluid mechanics for the measurement of entire velocity fields. In the PIV technique, the motion of a fluid (either liquid or gaseous) is visualized by illuminating a thin sheet of fluid containing reflective and neutrally buoyant tracer particles.

The most salient feature of PIV is the measurement of two components of displacement of a flow-tracing particle in a plane with respect to time. The measurement is performed by projecting a two-dimensional sheet of light into the region of interest. Natural particles or artificially introduced $seed$ are illuminated with a two-dimensional sheet of laser light.

Successive images of the illuminated $seed$ are taken with a digital camera positioned orthogonal to the plane of the light sheet. Advanced and sophisticated post-processing is required to handle the large amount of data collected with the PIV technique.

2.9.1 Rules for PIV Image Capture

For the best results from a PIV experiment, image acquisition and interrogation must match the flow. Typically, the following parameters can be controlled to optimize the measurement: the time between laser pulses (t) or the time between image acquisition; image shifting; photograph magnification; interrogation spot size; Dimensions of the arc; seed particles and seed concentration; and the light-sheet dimensions [16]. With these parameters in mind, the following rules were developed by Adrian and Keane [7].

Rule 1: The size of the interrogation window must be small enough for a vector to describe the flow within that point.

Rule 2: There should be more than ten particle image pairs per interrogation window.

Rule 3: The maximum displacements in the plane should be less than $\frac{1}{4}$ the size of the interrogation window.

Rule 4: The maximum out-of-plane displacement must be less than $\frac{1}{4}$ of the thickness of the light-sheet.

Rule 5: The minimum displacement in the plane must be two particle image diameters.

Rule 6: The exposure must be large enough to clearly show the particles.

$Figure$ 2.9.1 shows the PIV flow diagram.

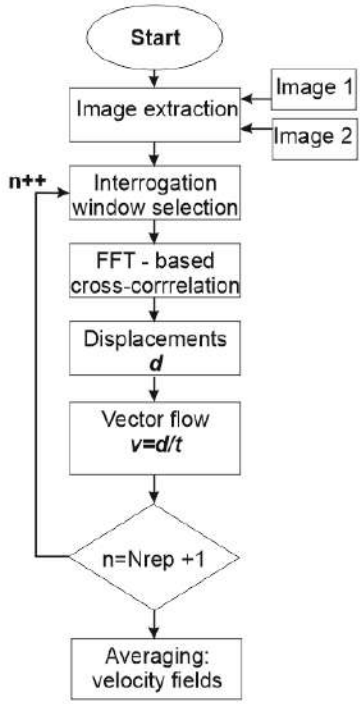

Figure 2.9.1: PIV flow diagram.

2.9.2 Technique Outline

PIV is a quantitative form of photographic flow visualization. According to the definition of speed, i.e. the first derivative of position with respect to time, the technique is to measure the displacement of the fluid (Δx) in a given time interval (t). The position of the liquid is made visible by light that is scattered by a liquid or solid, which is illuminated by a layer of laser light. In principle, it is a technique that measures the velocity of tracer particles that faithfully follow the flow. To achieve this, the flow is inoculated with small particles, assumed to be sufficiently small and light to move with local flow velocity and illuminated with a two-dimensional sheet of laser light. Proper particle seeding is essential for successful PIV measurements [16].

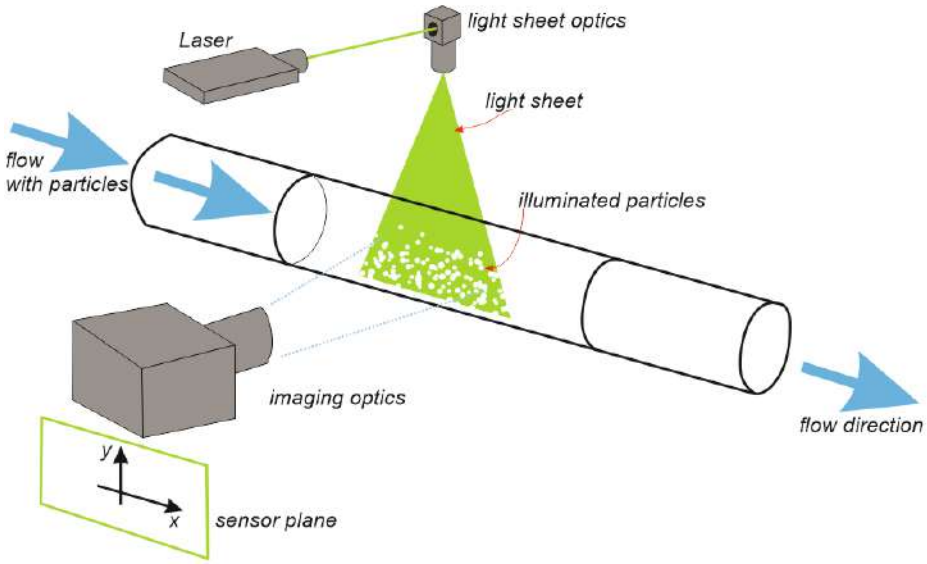

Figure 2.9.2: Principle of PIV technique: A laser sheet illuminates the particles in the fluid. A high-speed camera records the displacement of the particles.

$Figure$ 2.9.2 shows a typical set-up for PIV recording. Small tracer particles are added to the flow area (It is assumed that the tracer particles faithfully and accurately move with local flow velocity). A plane (light sheet) within the flow stream is illuminated by a sheet of laser light. The illuminated flow area is photographed from the side parallel to the illuminated sheet ($90°$ from the laser light sheet direction) with a digital camera capturing the movement of the particles. The light reflected off and scattered by the particles is captured and recorded as two separate images (at time t_0 and $t_0 + \Delta t$) on a high quality CCD camera sensor. The image analysis process mainly consist of determining the displacement of the particles. For evaluation, the digital PIV data set (each image) is divided into smaller interrogation regions, which are referred to as the $interrogation\ windows$". The size of these regions determines the spatial resolution of the measurement. The interrogation regions of the images are compared and the pixels are cross-correlated using a cross-correlation algorithm, as shown in $Figure$ 2.9.3.

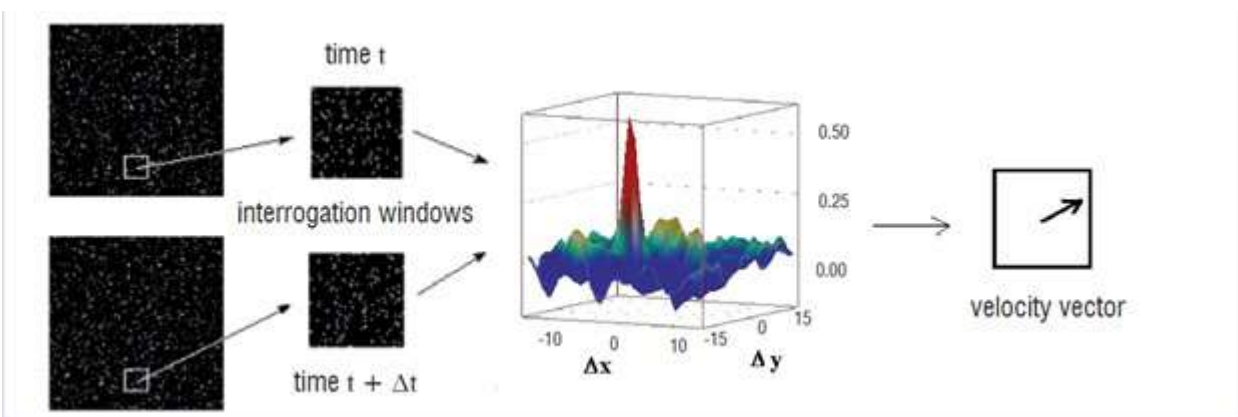

Figure 2.9.3: Cross-correlation process [9].

The cross-correlation program creates a peak in each region so that each square has a velocity vector based on the seed displacement and the time between successive images. The data is then used to generate a velocity

vector and streamline plots in the illuminated plane to access the fluid dynamics in the area of interest. The interrogation process is repeated for all interrogation areas in the PIV recording. The local displacement vector of the particle images between the two illuminations is determined for each interrogation window by means of a spatial statistical cross-correlation function. Taking into account the time interval between the images, it is possible to derive the projection of the velocity vector of the local flow onto the plane of the light sheet that is assigned to the center of the interrogation window. The main advantage of the PIV technique is its ability to provide a quantitative and instantaneous measurement of velocity not only at the point but at the same time on a whole plane simultaneously: visualization and quantification of the $2D$ flow structure are available. A more elaborate description of the PIV method can be found in literature [23].
It is important to note that the PIV technique uses information from the interrogation window to obtain only one velocity vector. In this sense, the value of the computed velocity is an average of the velocity of all particles in the interrogation window. The velocity field obtained is thus a filtered version of the actual flow field.

2.9.3 Mathematical Derivation

The PIV technique provides global velocity data within a two-dimensional area and does not directly measure important differentiable quantities such as vortex and strain velocities or integral quantities such as streamlines, circulation or potential lines. As such, they must then be calculated from the velocity fields [9]. The next sections explain how to perform such calculations.

Calculation of Differential Flow Properties

The displacement of the tracer particles $\vec{d}$ can be expressed in its components u, v and w, where u is the horizontal component and v is the vertical component in the plane, and w is a component perpendicular to both u and v. To distinguish the velocity field data, it must first be determined which terms can actually be calculated from the planar velocity field. Starting from the complete velocity gradient tensor or the strain tensor, which are both a result of the deformation tensor, the following can be stated:

$$\vec{d}(\vec{r}) = \begin{bmatrix} \frac{\partial u}{\partial x} & \frac{\partial u}{\partial y} & \frac{\partial u}{\partial z} \\ \frac{\partial v}{\partial x} & \frac{\partial v}{\partial y} & \frac{\partial v}{\partial z} \\ \frac{\partial w}{\partial x} & \frac{\partial w}{\partial y} & \frac{\partial w}{\partial z} \end{bmatrix} \begin{bmatrix} dx \\ dy \\ dz \end{bmatrix}.$$

$$= \begin{bmatrix} \frac{\partial u}{\partial x} & \frac{1}{2}\left(\frac{\partial v}{\partial x} + \frac{\partial u}{\partial y}\right) & \frac{1}{2}\left(\frac{\partial w}{\partial x} + \frac{\partial u}{\partial z}\right) \\ \frac{1}{2}\left(\frac{\partial v}{\partial x} + \frac{\partial u}{\partial y}\right) & \frac{\partial v}{\partial y} & \frac{1}{2}\left(\frac{\partial w}{\partial y} + \frac{\partial v}{\partial z}\right) \\ \frac{1}{2}\left(\frac{\partial w}{\partial x} + \frac{\partial u}{\partial z}\right) & \frac{1}{2}\left(\frac{\partial w}{\partial y} + \frac{\partial v}{\partial z}\right) & \frac{\partial w}{\partial z} \end{bmatrix} + \begin{bmatrix} 0 & \frac{1}{2}\left(\frac{\partial v}{\partial x} - \frac{\partial u}{\partial y}\right) & \frac{1}{2}\left(\frac{\partial w}{\partial x} - \frac{\partial u}{\partial z}\right) \\ -\frac{1}{2}\left(\frac{\partial v}{\partial x} - \frac{\partial u}{\partial y}\right) & 0 & \frac{1}{2}\left(\frac{\partial w}{\partial y} + \frac{\partial v}{\partial z}\right) \\ -\frac{1}{2}\left(\frac{\partial w}{\partial x} - \frac{\partial u}{\partial z}\right) & -\frac{1}{2}\left(\frac{\partial w}{\partial y} - \frac{\partial v}{\partial z}\right) & 0 \end{bmatrix}, \tag{2.9.1}$$

Substitution of strain components gives:

$$\begin{bmatrix} \frac{\partial u}{\partial x} & \frac{1}{2}\left(\frac{\partial v}{\partial x} + \frac{\partial u}{\partial y}\right) & \frac{1}{2}\left(\frac{\partial w}{\partial x} + \frac{\partial u}{\partial z}\right) \\ \frac{1}{2}\left(\frac{\partial v}{\partial x} + \frac{\partial u}{\partial y}\right) & \frac{\partial v}{\partial y} & \frac{1}{2}\left(\frac{\partial w}{\partial y} + \frac{\partial v}{\partial z}\right) \\ \frac{1}{2}\left(\frac{\partial w}{\partial x} + \frac{\partial u}{\partial z}\right) & \frac{1}{2}\left(\frac{\partial w}{\partial y} + \frac{\partial v}{\partial z}\right) & \frac{\partial w}{\partial z} \end{bmatrix} = \begin{bmatrix} \epsilon_{xx} & \frac{1}{2}\epsilon_{xy} & \frac{1}{2}\epsilon_{xz} \\ \frac{1}{2}\epsilon_{xy} & \epsilon_{yy} & \frac{1}{2}\epsilon_{zy} \\ \frac{1}{2}\epsilon_{xz} & \frac{1}{2}\epsilon_{yz} & \epsilon_{zz} \end{bmatrix}, \tag{2.9.2}$$

While for the vorticity tensor it is defined as:

$$\nabla \times \overrightarrow{V} = \begin{bmatrix} \hat{i} & \hat{j} & \hat{k} \\ \frac{\partial}{\partial x} & \frac{\partial}{\partial y} & \frac{\partial}{\partial z} \\ u & v & z \end{bmatrix} = \quad \hat{i}\left(\frac{\partial w}{\partial y} - \frac{\partial v}{\partial z}\right) - \hat{j}\left(\frac{\partial w}{\partial x} - \frac{\partial u}{\partial z}\right) + \hat{k}\left(\frac{\partial v}{\partial x} - \frac{\partial u}{\partial y}\right) = (\gamma_{yz}, -\gamma_{xz}, \gamma_{xy}), \tag{2.9.3}$$

so;

$$\begin{bmatrix} 0 & \frac{1}{2}\left(\frac{\partial v}{\partial x} - \frac{\partial u}{\partial y}\right) & \frac{1}{2}\left(\frac{\partial w}{\partial x} - \frac{\partial u}{\partial z}\right) \\ -\frac{1}{2}\left(\frac{\partial v}{\partial x} - \frac{\partial u}{\partial y}\right) & 0 & \frac{1}{2}\left(\frac{\partial w}{\partial y} + \frac{\partial v}{\partial z}\right) \\ -\frac{1}{2}\left(\frac{\partial w}{\partial x} - \frac{\partial u}{\partial z}\right) & -\frac{1}{2}\left(\frac{\partial w}{\partial y} - \frac{\partial v}{\partial z}\right) & 0 \end{bmatrix} = \begin{bmatrix} 0 & -\frac{1}{2}\gamma_{xy} & -\frac{1}{2}\gamma_{xz} \\ \frac{1}{2}\gamma_{xy} & 0 & -\frac{1}{2}\gamma_{zy} \\ \frac{1}{2}\gamma_{xz} & \frac{1}{2}\gamma_{yz} & 0 \end{bmatrix}, \tag{2.9.4}$$

hence;

$$\vec{d}(\vec{r}) = \begin{bmatrix} \epsilon_{xx} & \frac{1}{2}\epsilon_{xy} & \frac{1}{2}\epsilon_{xz} \\ \frac{1}{2}\epsilon_{xy} & \epsilon_{yy} & \frac{1}{2}\epsilon_{zy} \\ \frac{1}{2}\epsilon_{xz} & \frac{1}{2}\epsilon_{yz} & \epsilon_{zz} \end{bmatrix} + \begin{bmatrix} 0 & -\frac{1}{2}\gamma_{xy} & -\frac{1}{2}\gamma_{xz} \\ \frac{1}{2}\gamma_{xy} & 0 & -\frac{1}{2}\gamma_{zy} \\ \frac{1}{2}\gamma_{xz} & \frac{1}{2}\gamma_{yz} & 0 \end{bmatrix}, \tag{2.9.5}$$

The symmetry of the tensor represents the strain tensor with the elongation strains on the diagonal and the off-diagonal shear strains, while the asymmetric part contains only the vorticity components. Since the conventional two-component $(2D)$ PIV technique only provides the velocity components (u, v) and that these data can only be differentiated in the (x, y) directions, only a few terms of the expression 2.9.6 can be estimated by PIV, simplifying in the form:

$$\vec{d}(\vec{r}) = \begin{bmatrix} \epsilon_{xx} & \frac{1}{2}\epsilon_{xy} \\ \frac{1}{2}\epsilon_{xy} & \epsilon_{yy} \end{bmatrix} + \begin{bmatrix} 0 & -\frac{1}{2}\gamma_{xy} \\ \frac{1}{2}\gamma_{xy} & 0 \end{bmatrix}, \tag{2.9.6}$$

since the third velocity component terms and $\frac{d}{dz}$ cannot be measured. Since the fields for vorticity and strain rates cannot be measured directly , differentiation schemes should be used to derive these quantities.

2.9.4 Computation of the Cross-correlation Function

The computation of the cross-correlation function is at the heart of most PIV data processing and is generally based on Fast-Fourier Transform (FFT) algorithms. The cross-correlation analysis of PIV images yields a statistical estimate of the local tracer particles' displacement, an iterative process which yields velocity vectors using interrogation windows. With some degree of generality, the use of such an operator is interpreted as an optimization process.

The correlation method calculates the displacement $\vec{d}$ of the particles using two images. The first image I_1 is at time t, while the second image I_2 is at time $t + dt$, where dt is a small change in time. The method works with gray-scale images. Normally the scale is from 0 to 255, representing the lowest and highest value of light intensity respectively. In this way, the white pixels in the images indicate particles and the black background represents the void. The main objective of the correlation method is to obtain the displacement of each particle using the two images. Recognizing each particle in the two images and then calculating the displacement is a really complex problem since an image can contain thousands of similar particles. It is common to divide the image into small sub-images and correlate them with their peers between images. With this result it is possible to determine the

displacement of the particles.
For the digital evaluation of PIV, it is suggested to follow the following steps:

- Get the two images and store them on a computer in a gray-scale.
- Filter images to reduce noise
- Divide the averaged images into small samples. If the correlation is carried out using the Fourier transform, the samples of the images I_1 and I_2 must have the same size.
- Apply the FFT to each sample of images I_1 and I_2.
- Calculate the product of the Fourier transform of the partial image I_{sf1} with the corresponding conjugate of the Fourier transform of the partial image I_{sf2}. Calculate this for each pair of samples and then apply the inverse FFT;
$$PIV = \left|\mathcal{F}^{-1}\left\{\mathcal{F}\left\{I_1\right\}\mathcal{F}\left\{I_2\right\}^*\right\}\right|, \tag{2.9.7}$$
- Find the coordinates of the correlation peak that correspond directly to the displacement. The displacement is given by the distance from the center of the correlation peak to the center of the correlation image.

The position of the correlation peak is very important in the digital evaluation of this technique; This peak can be measured with sub-pixel precision. Since the input data is discretized, the correlation value only exists for integral shifts. The peak value only allows $\frac{1}{2}$ pixel precision for displacement.
The PIV algorithm is developed and tested so that it could be applied to the BOS technique which involves tracking spots placed in a background, analogous to the PIV technique. The BOS technique is discussed next.

2.10 Background Oriented Schlieren

Background Oriented schlieren (BOS) is a flow visualization technique that carries the promise of quantitative measurements. Flow visualization in its broadest sense represents any technique that is used to detect the movement of the fluid and extract additional information about the flow by making the flow visible.
Schlieren techniques are fundamental and valuable tools in a number of scientific and technical disciplines and are well-known methods to visualize refractive index gradients in compressible flows [23]; they allow visualisation and recording of otherwise invisible light refractions (phase differences) in transparent media. Finding out the refractive index, temperature and density helps to understand and control various flow behaviours.
The background Oriented Schlieren technique is a fast and emerging technique for visualizing high speed flows and flows in general, with the use of digital image processing, which replaces optical processing in classical Schlieren. The use of simple optics, high precision, rapid evaluation and the authoritative role of numerical methods are some of the main advantages of using these methods.
There are different Schlieren technique arrangements, each used for different purpose. In this thesis report, only BOS (Background Oriented Schlieren) is discussed and implemented. The BOS technique is an optical density visualisation technique which uses correlation on a background pattern to quantitatively characterize compressed and thermal flows. In its most basic form, this technique uses an electronic camera with a high shutter speed, a high intensity light source, and a structured background dot pattern as the main optical elements.

2.10.1 Fundamental Properties of the BOS Technique

The BOS technique is sensitive to integrated refractive index gradients that are perpendicular to the line of sight. The experimental setup for typical arrangements of the BOS experiment can be organized by placing the background target with the randomly generated dots on one side and a camera on the other, $Figure$ 2.10.1 and $Figure$ 2.10.2 [15, 16]. The density gradients present in the inhomogeneous flow area lead to a certain deviation of what the camera sees from a homogeneous field between the camera and the background pattern. The image of an undistorted random dot on background pattern B, seen along the solid blue straight line without schlieren (object labeled O on the schematic representation of $Figure$ 2.10.2), is shifted by the refraction of object O (dotted magenta-colored line) to $B^{'}$. In the figure, the space between z_1 and z_2 defines the object area, L represent the lens, S is the camera sensor, B is the background, s_t is the distance from the object to the background, s_0 is the distance from the object to the lens, and s_i is the distance from the lens to the sensor.
The distortion is caused by the bending of the light rays due to inhomogeneities in the medium and is described by the functional dependence of the refractive index of the space $n(\vec{r})$. BOS is sensitive to the deflection angle ξ_x of light rays propagating through a varying refractive-index field. With the small refraction angle ε_x, this shift is seen as the $\triangle x$ displacement from the point on the camera image sensor. $\triangle x$ can be measured by comparing background images with and without object O by the use of digital image correlation software that detects the shift in a small interrogation window. The cross-correlation software developed for the PIV, discussed in the previous section, is used for this purpose.
Once $\triangle x$ is known, the angle of refraction ε_x is determined from the trigonometry of the setup. ε_x is the result of a line integral of the refractive index gradient $\frac{\partial n}{\partial x}$ along the optical axis z through the Schlieren object O, given by $Eq.(2.4.9)$. Once ε_x and ε_y in a $2D$ matrix are retrieved, the mapping of grayscale values leads to a useful pseudo-schlieren image.

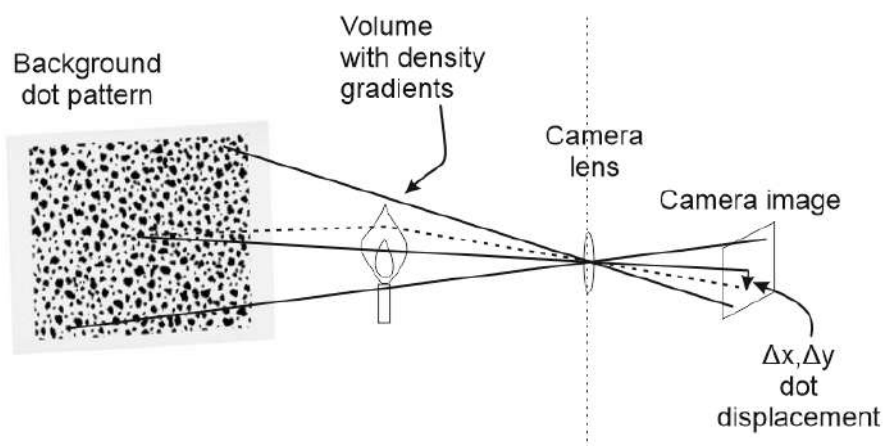

Figure 2.10.1: Conceptual drawing of BOS imaging.

$\triangle x$ and $\triangle y$ are horizontal and vertical shifts of the background pattern due to the light waves traveling through the density gradient.

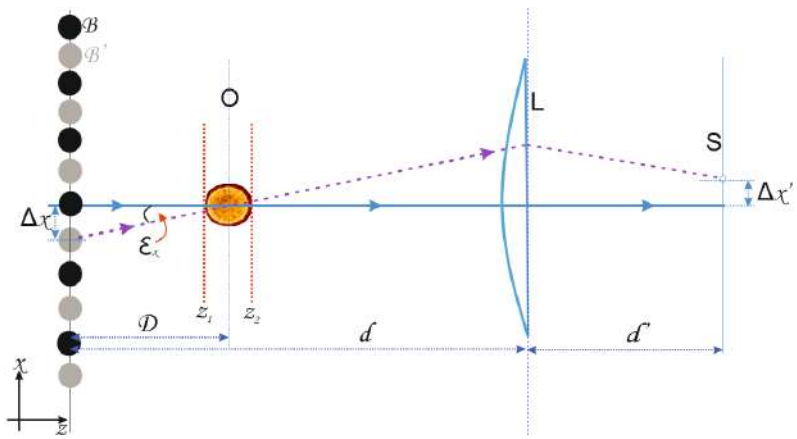

Figure 2.10.2: Typical setup illustrating the integrating nature of the BOS technique.

Information about the density gradient field can be obtained from the relationship between the refractive index n and the density ρ given by the Gladstone-Dale equation $Eq.(2.3.2)$, while the relationship between the refractive index n and temperature is given by $Eq.(2.3.8)$.

The relative displacement between the reference and displaced images can be obtained by cross correlation of corresponding sub-images. The position of the maximum on the correlation map directly defines the unknown displacements, as described for the PIV technique. The density field of axisymmetric flows are calculated from the Schlieren data after applying a Fourier transform algorithm. In this case, the transform algorithm reconstructs the density field from ray deflections.

The background Oriented Schlieren technique consists of two independent phases: image acquisition and image evaluation. The first addresses the problems of designing the pattern to be imaged, locating the components in the optical assembly, and determining suitable conditions for capturing the images. The image evaluation portion addresses the problems of comparing reference and measurement images and extracting data from these comparisons. The predominant method of data extraction in BOS is based on cross-correlation algorithms developed for particle image velocimetry [26].

2.10.2 Sensitivity and Spatial Resolution of the BOS Method

The background Oriented Schlieren measurement can quantify the ray deviation, however, it is only integrated through the line of sight, illustrated in $Figure$ 2.10.1 and $Figure$ 2.10.2. $Figure$ 2.10.3 shows another schematic representation of the optical setup to be used for sensitivity analysis. Shown in the figure; structured background, test area to be examined, lens with focal length F, image recording sensor and the specified distances and designated angles. When recording a feature located at point B on the background image, the point is imaged in the point I. Introducing an object with variable index of refraction $n(\vec{r})$ deflects the beam by an angle ε, so that the imaged point is displaced by $\triangle x'$ to point J. The prerequisite for observing this effect is that the pattern displacement $\triangle x'$ is greater than the linear size of the pixel l_{px}.

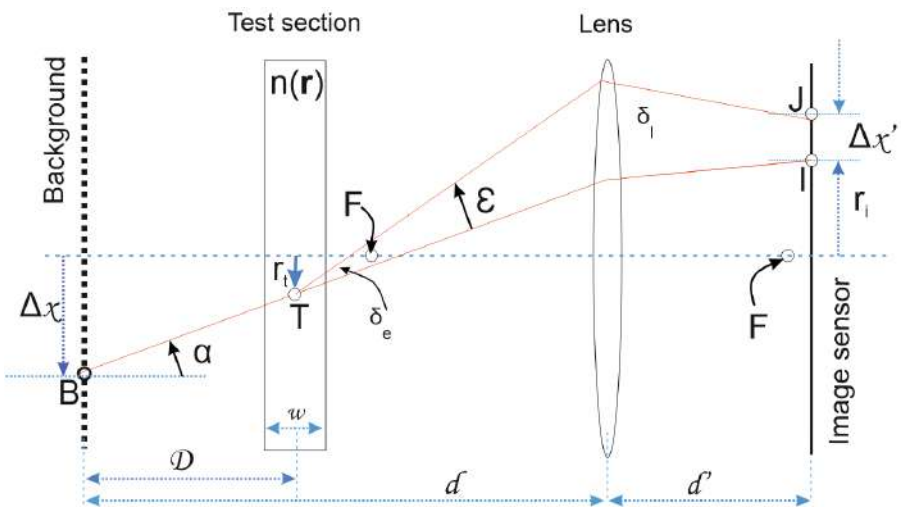

Figure 2.10.3: Optical set-up schematic

The limit of detection is determined based on the relation:

$$\triangle x' \geq l_{px}. \tag{2.10.1}$$

One consequence of the change in the direction of the beam is that the beam leaves the test area at a different point than the beam while recording the reference image. But this difference, indicated as δ_e in $Figure\,2.10.3$, is negligible as long as δ_l, the distance between the entry points of these beams into the lens is much larger. Since $\frac{\delta_e}{\delta_l} = \frac{w}{(d-D)}$ (w is the width of the test section), this condition is fulfilled only if:

$$\frac{w}{(d-D)} \ll 1. \tag{2.10.2}$$

This means that in the case of a BOS structure with dimensions that are much larger than the width of the test area, it can be assumed that the object only deflects the light beam, but does not displace it. In addition, as in the case of the thin lens described by the main plane, the entire test section can be approximated by a refractive plane.

2.10.3 Discussion

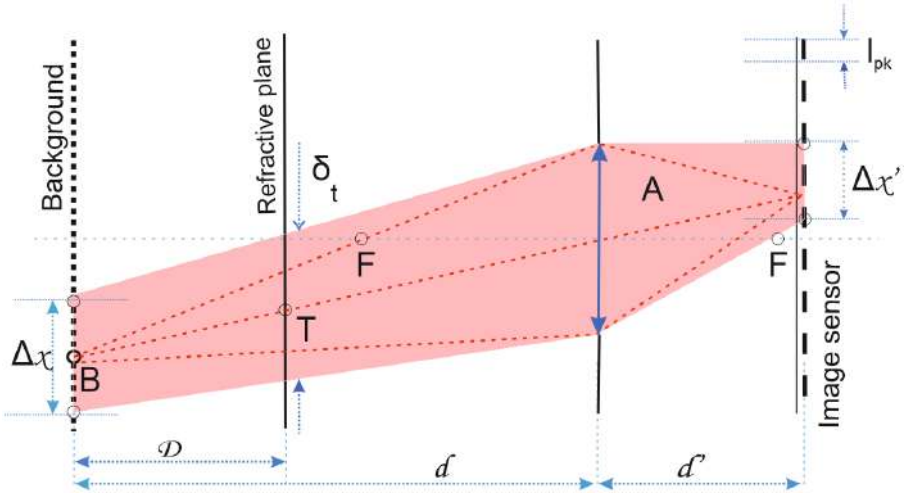

Figure 2.10.4: Light cone creating the image in the BOS system.

In the described BOS method, the test section is placed between the background and the objective lens. This limits the values of D in the range $0 < D < d$ and thus the sensitivity S of the BOS setup is given by

$$0 < S < d'. \tag{2.10.3}$$

This shows that the sensitivity of a BOS setup can be set to any level, limited only by the focal length of the lens. In practice, however, the sensitivity is adjusted by defining the spatial size of the experimental setup (setting D, limited by the laboratory space and field of view) and the lenses and cameras used (setting of M). In older publications on the sensitivity of BOS, the use of lenses with a long focal length was recommended to increase the sensitivity. While this is correct, however, lenses with a long focal length are preferred: Lenses with a longer focal length lead to higher magnifications [26].

The spatial resolution of a BOS structure, which represents a characterization of the blurred out-of-focus imaging, is affected by two terms consisting of different parameters. It can be said that $\triangle x'$ and $f_{\#}$ are characteristics of the camera and have a limited number of values, typically 5–$50\mu m$ for $\triangle x'$; and 5.6–32 for $f_{\#}$ [26]. At relatively large magnifications $(M > 0.1)$, the second term can be neglected due to a very low value for $\triangle x'$: if error propagation is taken into account, even a small uncertainty in D, for example 0.1 $(1mm$ in a meter$)$ would result in a greater uncertainty in δ_t than the value of $\frac{\triangle x'}{M}$ itself. Therefore, a good approximation of the spatial resolution in relation to experimentally measured parameters can be expressed as

$$\delta_t = \frac{d'}{d' + d}\frac{D}{f_{\#}}. \tag{2.10.4}$$

This result can be interpreted as follows: The deflection angle ε at point T is affected by the change in the refractive index $n(\vec{r})$ along the entire light cone with the vertex at B and the base diameter δ_t, $i.e.$, $r = r_t \pm \delta_t$. An important observation is that neither the sensitivity S nor the spatial resolution δ_t are dependent on the angle α.

The advantage of the BOS method is that it is very easy to couple with the Particle Image Velocimetry (PIV). The next section covers another Background Oriented Schlieren; the Fringe Deflection technique. The two techniques; BOS and FD are compared numerically and experimentally later in this Thesis work.

2.11 Fringe Deflection

For the BOS method, randomly located dots are used, however, straight (horizontal, vertical, or crossed) fringes are used for the Fringe Deflection technique. $Figure$ 2.11.1 shows the experimental setup, $Figure$ 2.11.2 shows the schematic representation of the experimental setup. Another difference is that the BOS technique uses the cross-correlation method to detect the displacements, while the FD technique uses the Fourier transform mechanism to determine the phase difference between the fringes.
The FD experimental setup is similar to the BOS setup, except that straight-line fringes are used instead of the random point. The $Figure$ 2.10.2 shows the phase object placed between the CCD camera and the background. The object deflects light rays at an angle ε_x, which is recorded by the camera as $\triangle x$.

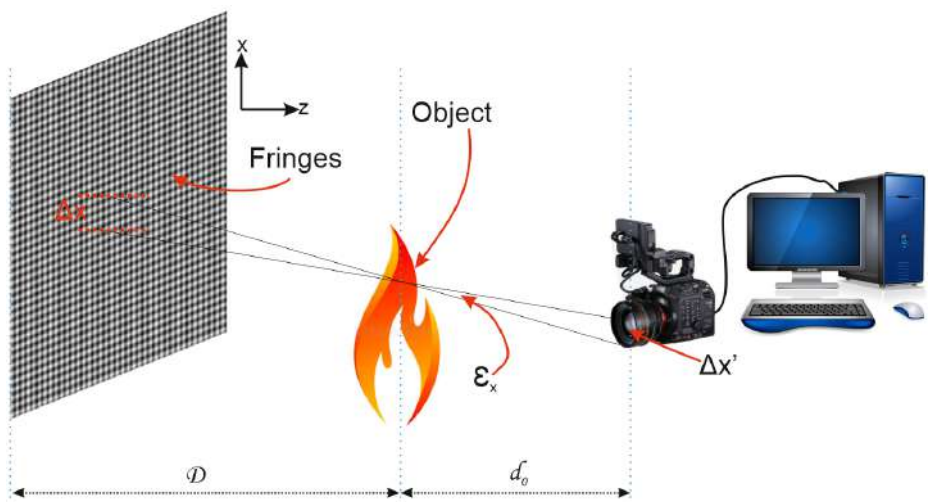

Figure 2.11.1: FD experimental set-up consisting of a grid, a CCD camera coupled with a lens, a candle flame in the object area, and a computer. .

As can be seen in $Figure$ 2.11.2, when the object is introduced, the fringe background B is perceived to have been deflected by $\triangle x$ to B'. The parameters and concept are the same as described for the configuration of the BOS.

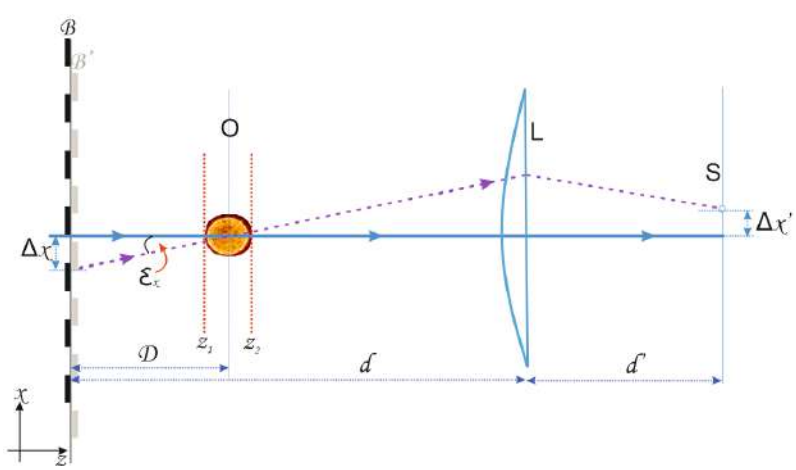

Figure 2.11.2: Typical schematic representation of the set-up, illustrating the integrating nature of the FD technique.

2.11.1 Fundamental Operation of the FD Technique

The basic functionality of FD technique is similar to that of BOS technique presented in the previous section. The only difference is that instead of the random dotted background pattern used in the BOS technique, the FD use fringes of straight lines (horizontal, vertical or crossed) as the background pattern, as shown in $Figure$ 2.11.2. Like BOS, FD generates an optical distortion from the background image of a second image, which is digitally processed with the first in order to produce displacements characteristic of the distortion field. This approach requires modern computer-aided optical processing and digital imaging.

Two images are compared which correspond to two different states of a phase object; with and without an object. After the object has been introduced, the corresponding spatial structures are shifted from their original position. The shifts are proportional to the change in the refractive index. The displacements are calculated by retrieving the phases.

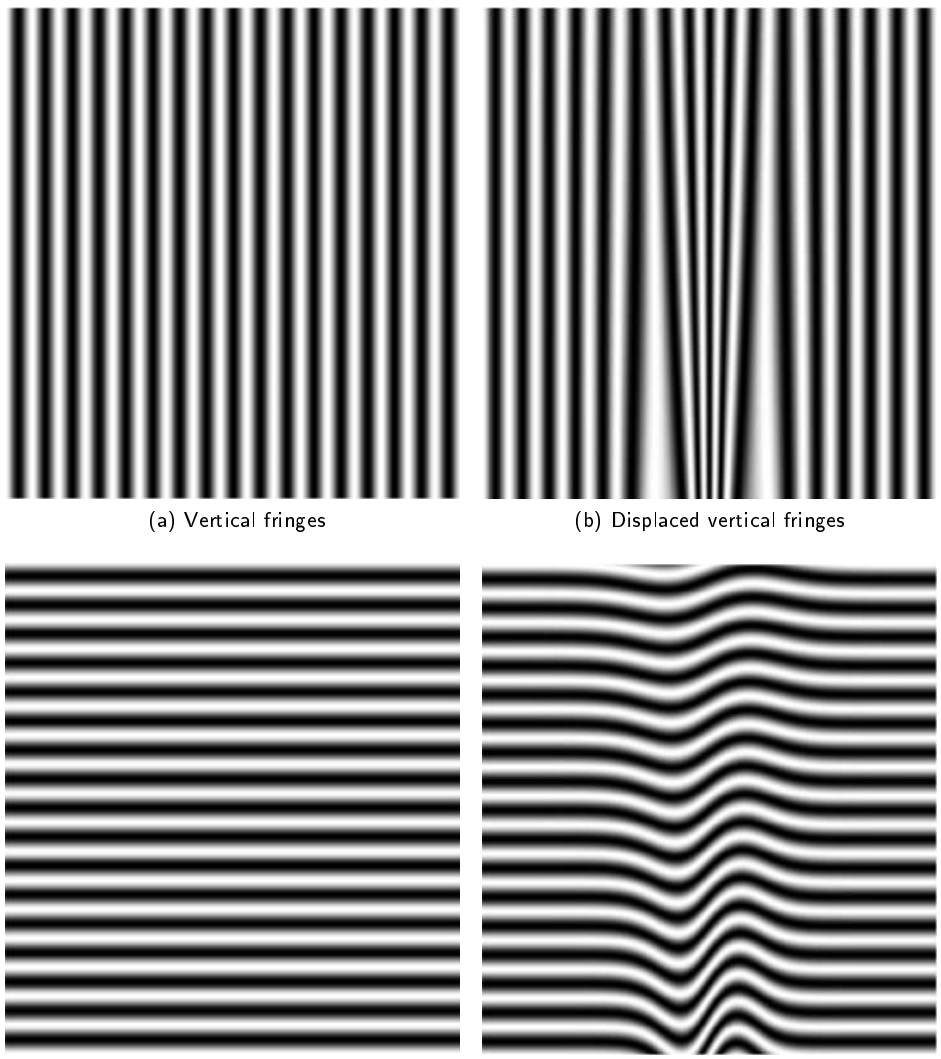

(a) Vertical fringes (b) Displaced vertical fringes

(c) Horizontal fringes (d) Displaced horizontal fringes

Figure 2.11.3: Fringes a) vertical fringes, b)displaced vertical fringes,c) horizontal fringes, d) displaced horizontal fringes

$Figure$ 2.11.3 (a) and (c) show vertical and horizontal fringes, (b) and (d) show displaced fringes. The fringe

deflection method is well suited for the calculation of in-plane displacements, such as those that occur when a beam light is deflected by a phase object. The fringes are created by a pattern of straight sinusoidal fringes (lines-per-inch). The deviation from the straightness of the fringes can be of the order of a fraction of the grating period. The deviations correspond to the displacement of each point that forms a fringe. To achieve sensitivity in the horizontal and vertical directions, a perpendicular cross grid should be used.
The displacements are calculated as follows. For background images that only consist of a grid aligned in the vertical direction, the reference image can be expressed by following equation that represents the intensity.

$$I_1(x,y) = a(x,y) + \frac{1}{2}b(x,y)\left[exp\left(i(2\pi f_0 x + \phi_{ref})\right) + exp\left(-i(2\pi f_0 x + \phi_{ref})\right)\right],$$

$$I_1(x,y) = a(x,y) + b(x,y)\left[cos(2\pi f_0 x + \phi_{ref})\right], \tag{2.11.1}$$

and

$$I_2(x,y) = a(x,y) + \frac{1}{2}b(x,y)\left[exp\left(i(2\pi f_0 x + \phi_{ref} + \Delta\phi)\right) + exp(-i(2\pi f_0 x + \phi_{ref} + \Delta\phi))\right],$$

$$I_2(x,y) = a(x,y) + b(x,y)\left[cos(2\pi f_0 x + \phi_{ref} + \Delta\phi)\right], \tag{2.11.2}$$

where $a(x,y)$ is the average intensity related to pattern brightness and back-lighting, $b(x,y)$ is the intensity modulation related to the pattern contrast and surface reflectivity, f_0 is the carrier frequency, ϕ_{ref} is a phase term that takes into account perspective and aberration effects, and $\Delta\phi(x,y)$ is the phase resulting from deviations from the straight fringes after introducing the object.
The arguments of $Eq.(2.11.1)$ and $Eq.(2.11.2)$ can be calculated using the Fourier phase extraction method as follows:

$$I_1(x,y) = a(x,y) + \frac{1}{2}b(x,y)exp\left(i2\pi f_0 x\right)exp\left(i\phi_{ref}\right) + \frac{1}{2}b^*(x,y)exp\left(-i2\pi f_0 x\right)exp\left(-i\phi_{ref}\right). \tag{2.11.3}$$

Apply the Fourier transform to $Eq.(2.11.3)$, yields

$$I_F(f_x,f_y) = A(f_x,f_y) + B\left(f_x - f_0, f_y\right) + B^*\left(-f_x - f_0, f_y\right), \tag{2.11.4}$$

where $A(f_x,f_y) = \Im\left\{a(x,y)\right\}$ and $B(f_x,f_y) = \Im\left\{\frac{1}{2}b(x,y)exp(i2\pi f_0 x)exp(i\phi_{ref})\right\}$.

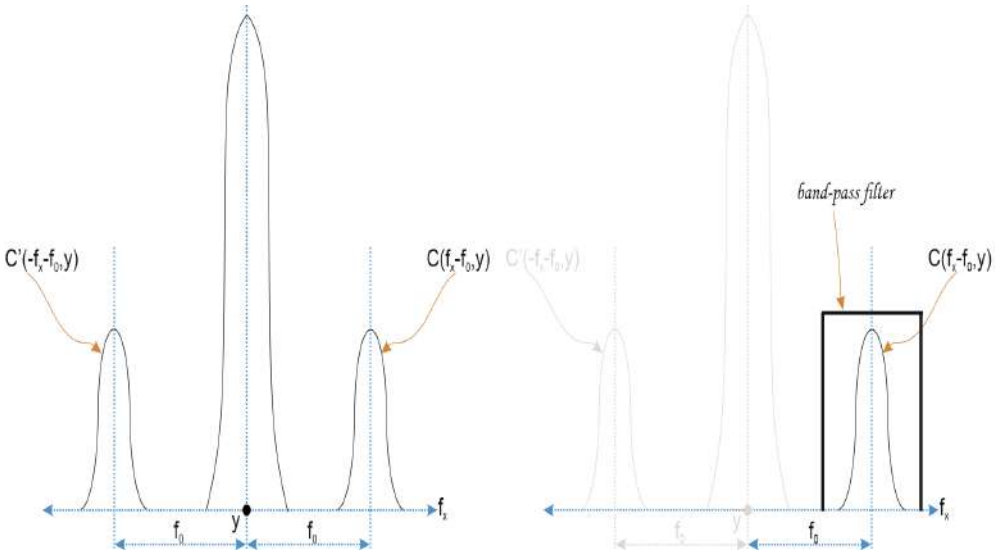

(a) Fourier spectrum of a fringe pattern. (b) Single spectrum isolated by a band-pass filter.

Figure 2.11.4: Fourier spectrum lobes.

Apply a band pass filter to $Eq.(2.11.4)$ to isolate a side lobe (centered on the carrier frequency f_0) as shown in $Figure$ 2.11.4(b), results in:

$$I_{FP}(f_x, f_y) = B\left(f_x - f_0, f_y\right). \tag{2.11.5}$$

Finally, apply the inverse Fourier transform to $Eq.(2.11.5)$ to give

$$\begin{aligned}\Im^{-1}\left\{B\left(f_x - f_0, f_y\right)\right\} &= \Im^{-1}\left\{\Im\left[b(x,y)exp(i2\pi f_0 x)exp(i\phi_{ref})\right]_{f_x - f_0, f_y}\right\} \\ &= \frac{1}{2}b(x,y)exp\left[i(2\pi f_0 x + \phi_{ref})\right] \\ &= C(x,y) + iS(x,y),\end{aligned} \tag{2.11.6}$$

where $C(x,y) = (\frac{1}{2})b(x,y)cos(2\pi f_0 x + \phi_{ref})$ and $S(x,y) = (\frac{1}{2})b(x,y)sin(2\pi f_0 x + \phi_{ref})$. Therefore, the reference argument can be obtained from

$$2\pi f_0 x + \phi_{ref} = tan^{-1}\left[\frac{S(x,y)}{C(x,y)}\right]. \tag{2.11.7}$$

Similarly, the argument of the displaced fringe pattern can be calculated and the desired phase term can be obtained by subtracting the arguments. $\Delta\phi = (2\pi f_0 x + \phi_{ref} + \Delta\phi) - (2\pi f_0 x + \phi_{ref})$. The displacement in the $x-$direction Δx is related to $\Delta\phi$ by $Eq.(2.4.32)$ where $P = \frac{1}{f_0}$ is the period of the sinusoidal fringes.

In this chapter the background and basic mathematical derivations are developed. The next chapter deals with literature view to understand what has been done in this area of research.

Bibliography

[1] Snell's Law, Encyclopedia Britanica, Retrieved on May, 2, (2021) $https://www.britannica.com/science/Snells-law$.

[2] K. Okamoto, "Fundamentals of Optical Waveguides", Academic Press, 7, 8, 67 (2006).

[3] G. Lifante, "Integrated Photonics: Fundamentals" Wiley, 7, 8, 10 (2003).

[4] S. Doric, "Ray tracing through gradient-index media: recent improvements", Appl. Opt. 29 4026-9 (1990).

[5] G.E. Elsinga, B.W. Van Oudheusden, F. Scarano, and D. W. Watt, "Assessment and application of quantitative schlieren methods: Calibrated color schlieren and background oriented schlieren.", Exp. Fluids 36, 309-325 (2004).

[6] J. Hazewinkel, L. R. M. Maas, and S. B. Dalziel, "Tomographic reconstruction of internal wave patterns in a paraboloid," Exp. Fluids 50, 247-258 (2011).

[7] R. Adrian, and R. Keane, "Optimization of particle image velocimeters. Part 1: Double pulsed systems.", Measurement Sci. Technol, 1(1): 1202-1215 (1990).

[8] M. Raffel, C. Willert, S. Wereley and J. Kompenhans, "Particle Image Velocimetry: A Practical Guide.", Vol. 2nd, New York: Springer. 448 (2007).

[9] M. Raffel, C.E. Willert, F. Scarano, C.J. Kahler, S.T. Wereley and J. Kompenhans, "Particle Image Velocimetry_ A Practical Guide", Experimental Fluid Mechanics, Springer (2018).

[10] O. S. Jensen, J. P. Kunsch, and T. Rosgen, "Optical density and velocity measurements in cryogenic gas flows", Exp. Fluids 39, 48-55 (2005).

[11] C. Brossard, J.-C. Monnier, P. Barricau, F.-X. Vandernoot, Y. Le Sant, F. Champagnat, and G. Le Besnerais, "Principles and Applications of Particle Image Velocimetry", Optical Diagnostics of Flows. The Onera Journal Aerospace Lab. Issue 1 - December (2009).

[12] D. Dabiri, "Cross-Correlation: Digital Particle Image Velocimetry - A Review.", University of Washington Seattle, WA (2006).

[13] M. Raffel, "Background-oriented schlieren (BOS) techniques", Exp. Fluids 56 60 (2015).

[14] G.S. Settles, and M.J. Hargather, "A review of recent developments in schlieren and shadowgraph techniques.", Measurement Science and Technology 28(4): 042001 (2017).

[15] G.E.A. Meier, "Computerized background-oriented schlieren.", Exp. Fluids 33 181–7 (2002).

[16] H, Richard and M. Raffel, "Principle and applications of the background oriented Schlieren Methods", Meas. Sci. Technol, 12, 1576-1585 (2001).

[17] S.B. Dalziel, G.O. Hughes, and B.R. Sutherland, "Whole-field density measurements by 'synthetic schlieren'.", Exp. Fluids 28 322–35 (2000).

[18] L. Venkatakrishnan, and G.E.A. Meier, "Density measurements using the background oriented schlieren technique, Exp. Fluids 37, 237–47 (2004).

[19] G.E. Elsinga, B.W. van Oudheusden, F. Scarano, and D.W. Watt, "Assessment and application of quantitative schlieren methods: calibrated color schlieren and background oriented schlieren.", Exp. Fluids 36, 309–25 (2004).

[20] C. Alvarez-Herrera, D. Moreno, B. Barrientos and J. A. Guerrero-Viramontes, "Temperature measurement of air convection using a schlieren system," Opt. Laser Tech. 41, 233-240 (2008).

[21] E. Goldhahn, and J. Seume, "The background oriented schlieren technique: sensitivity, accuracy, resolution and application to a three-dimensional density field.", Exp. Fluid 43 241–9 (2007).

[22] S. Tokgoz, R. Geisler, L. J. A. van Bokhoven and B. Wieneke., "Temperature and velocity measurements in a fluid layer using background-oriented schlieren and PIV methods.", Measurement Science and Technology 23(11): 115302 (2012).

[23] G. Settles, "Schlieren and Shadowgraph Techniques: Visualizing Phenomena in Transparent Media.", Ed. by Springer (2001).

[24] C. K. Reinholtz, K. E. Scott, F. L. Heltsley and M. N. Rhode, "Visualization of Jettison Motor Plumes from an Orion Launch Abort Vehicle Wind Tunnel Model using Background-Oriented Schlieren". volume AIAA 2010-1736. US Air Force Test and Evaluation Days, Nashville TN, February (2010).

[25] J. Szinitman and T. Rosgen, "Whole-eld density visualization and abel reconstruction of axisymmetry vortex rings". J. Flow Visual. Im. Process. 13, 343-358, (2006).

[26] A.B. Gojani, B. Kamishi, and S. Obayashi, "Measurement sensitivity and resolution for background oriented schlieren during image recording.", The Visualization Society of Japan, June (2013).

[27] M. Takeda, H. Ina, and S. Kobayashi, "Fourier-Transform Method of Fringe-Pattern Analysis for Computer-Based Topography and Interferometry", J. Opt. Soc. Am., 72, 156-160 (1982).

[28] K.A. Nugent, "Interferogram Analysis Using an Accurate Fully Automatic Algorithm", Appl. Opt., 24, 3101-3105 (1985).

[29] D.J. Bone, H.A. Bachor, and R.J. Sandeman, "Fringe-Pattern Analysis Using a 2-D Fourier Transform", Appl. Opt., 25, 1653-1660 (1986).

[30] D. Malacara, M. Servin, and Z. Malacara, "Interferogram Analysis for Optical Testing", Chapters 2 and 11, Taylor & Francis, Boca Raton (2005).

[31] A. Mazumdar, "Principles and techniques of Schlieren Imaging Systems",Columbia University, New York (2013).

[32] W. Ballman, "Basic differential Geometry: Variational theory of geodeics", Mathematisches Institut, Universitat, Bonn (2003).

Chapter 3

Literature Review

Contents

3.1 Introduction

The application of digital analysis to particle image velocimetry (PIV) shows an increasing number of successful studies over this decade. As a result, the interest of the user community in exploring challenging workflows drives theoretical studies to gain a deeper understanding of $PIV(BOS)$ performance. In this Chapter, a wide range of past applications of $PIV(BOS)$ and FD in fluid and heat transfer are reviewed.

Turbulence has been a subject of research for over a century and there is still no complete understanding of the phenomena that cause it. Approaches to the study of turbulence are based on numerical, experimental and theoretical techniques, and the contribution of these techniques has made significant progress. With the advent of lasers in the $1960s$, it became possible to develop non-intrusive measurement techniques using sophisticated optical and electronic tools. $PIV(BOS)$ and FD are techniques applied to experimental fluid mechanics to measure whole velocity fields.

Background-oriented stripes have become a well-established technique for visualizing and quantifying the distributions of the refractive index gradient and numerous articles discuss the display of different types of variable density flows.

In this chapter different flow visualization techniques are explained. These techniques are divided into two categories; geometric (macroscopic) and thermodynamic parameter measurements. Conventional Schlieren is most commonly used to provide qualitative information and/or geometric flow parameters. In contrast, quantitative Schlieren is mainly used for thermodynamic parameter measurements such as density and temperature.

3.2 Geometric Flow Parameter Measurement

Lately, many practical experiments have been conducted with direct photographic imaging and image processing to measure macroscopic gas and fuel vapour flow parameters. The most common techniques for macro-spray parameters are direct photographic imaging and the conventional Schlieren technique. Most of these geometric parameter measurements are widely used in combustion and engine research, and there have been many important contributions from researchers in the field.

In modern form, PIV stands for the quantitative and accurate measurement of fluid velocity vectors at a large number of points simultaneously, and it is now understood that this is in fact a very challenging, complex, and relatively recent achievement.

The ability to capture thousands of PIV images made it desirable to speed up the interrogation process and automate vector cleanup.

3.3 Thermodynamic Flow Parameters Diagnostic Techniques

Temperature, flow velocity, density, pressure and species concentration are the universal parameters for describing the thermodynamic behavior of a flow. A number of researchers rigorously examined measurement techniques for optical thermodynamic parameters such as: Laser Induced Fluorescence (LIF), Rayleigh Scattering, Raman Scattering, and Coherent Anti-Stokes Raman Spectroscopy $(CARS)$. Other techniques that provide thermodynamic flow parameters are Laser Doppler Velocimetry (LDV), Particle Image Velocimetry (PIV), Background Oriented Schlieren (BOS), and Color Schlieren. These methods can be divided into molecular flow and particle flow diagnostic techniques.

3.3.1 Molecular Based Techniques

Molecular-based techniques include either elastic (non-energy-exchanging) or non-elastic (energy-exchanging) light scattering processes from atoms or molecules. Since the properties of the gas molecules are determined directly without seeding, these techniques can provide information about gas temperature and density that could not be found with particle-based techniques [1]. When a laser beam passes through a gas, the molecules cause inelastic and elastic light scattering. The inelastic scattering is called Raman scattering, and the elastic scattering is called Rayleigh scattering.

Table 3.1: Overview of the optical diagnostic tools used over the years.

Optical Measurement	**Scientific Approach**	**Major Equipment**	**Measured Parameters**
Raman Scattering	Detection of inelastic scattered light when light sheet hits atoms/ molecules.	Laser beam source, signal detectors, extra optical equipment	Concentration and temperature
Rayleigh Scattering	Detection of elastically scattered light when light sheet hits atoms / molecules.	Laser beam source, signal detectors and additional optical devices.	Density, Velocity, Temperature
Coherent Anti-Stokes Raman Spectroscopy $(CARS)$	Two laser beams with different wavelengths inside a flow stream to produce a third beam with different wavelengths. The shape of the spectral signature and the intensity of the third beam are used to measure the flow parameters.	Laser beam, signal processor and detectors.	Species concentration and Temperature
Planar Laser Induced Flouresence $(PLIF)$	Laser light resonance with species wavelength excites atoms/molecules to higher electronic energy states light is emitted when these molecules relax back to a lower energy state.	CCD camera, Laser beam, seed generator, optical filter.	Concentration, temperature, speed and pressure
Laser - Doppler Velocimetry (LDV)	By measuring the Doppler frequency shift, the difference between the frequencies of the received and incident lasers that are scattered by moving particle velocity can be calculated.	Signal receiver and processor, continuous laser beam photodetector, and additional optical devices.	Velocity and Turbulence
Phase Doppler Interferometry (PDI)	The difference between the received and incident laser light is used to measure particles diameter.	Laser beam photodetector, signal receiver and processor, additional optical devices.	Droplet size and velocity
Particle Image Velocimetry (PIV)	The scattered light from illuminated particles is recorded at different times and the correlation of the particle positions in frame pairs gives velocity and turbulence vectors.	CCD camera, seeds Generator, Laser beam, and optically Filter.	Velocity and turbulence
Rainbow Schlieren	The light beam refraction due to a change in the refraction index is measured using colour change of the recorded images.	Graded filter, light source and camera.	Temperature and Density
Background Oreiented Schlieren (BOS)	Refraction of light due to a change in the refractive index is measured using a distortion of the background images.	Camera, light source, high frequency background.	Temperature and Density

3.3.2 Particle Based Techniques

Particle-based measurement techniques use light reflection by seeding particles when a beam of light passes through the flow to measure flow parameters such as velocity and turbulence. Laser Doppler Anemometry (LDA), Planar Doppler Velocimetry (PDV), and Particle Image Velocimetry (PIV) are the most commonly used particle-based measurement techniques.
The direct relationship between the index of refraction and density of a fluid has been used to measure density and other thermodynamic parameters of flow.

3.4 Quantitative Schlieren

Quantitative Schlieren methods can measure the angles of light deflection in two spatial directions, and the spatial integration returns the projected density gradient field. Qualitative Schlieren techniques, in which Schileren photos or geometric flow data are examined, do not provide any data such as gas density, concentration temperature or speed information. Studies by Schardin [2] and Skotinov [4] discussed several quantitative Schlieren methods for gas dynamics research.
In the early research on optical flow measurement systems Kopf [3] in "Application of speckling for measuring the deflection of light by phase objects" emphasized practical implementations, extensions to specific cases, and overcoming existing limitations in the session on holographic interferometry and speckle. By assuming the speckle pattern to be a carrier, U. Kopf (Siemens AG, Munich) applied speckle techniques to carrier frequency holography and discussed the use of this technique in superimposing images to determine the time characteristics of a deformation process. The information provided by the article can be used to help develop alternative strategies.
Meier [5] and Dalziel [6] developed a quantitative Schlieren technique that measures the density variation, with which mainly scalar flow parameters are meeasured, and called it "Background Oriented Schieren (BOS)" and "Synthetic Schlieren" respectively. However, Settles [7] states that the correct name for the technique should be Synthetic Background - Distortion Schlieren Imaging.
Venkatakrishnan and Meier [8] developed a three-dimensional density distribution of an air jet using computed tomography. They calculated the refractive index as a line integral and developed a three-dimensional density field based on a filtered back projection algorithm. Goldhahn and Seume [9] considered projections recorded with BOS as gradient information and showed the possibility of directly with a computed tomography for the deflection measurement of BOS.
Klinge et al. [10] carried out BOS in conjunction with PIV measurements to derive quantitative data on the velocity and density of the wing tip vortex. Klinge [11] expanded the work of Meier [5] by developing a technique for measuring an incompressible flow velocity field using the density field of a fluid parcel as a marker. However, this method only worked for a flow rate of Mach 0.3 and below.
The first task in BOS data processing is to find the angular deflection vectors of the refracted light rays. Previous literature indicates that most deflection vector calculations were performed using optical flow techniques based on PIV-like regions. Atcheson et. al. [13] compared different optical flow techniques for the BOS vector calculation. Differential techniques estimate motion by examining the intensity gradient of the first and second order derivatives in space and time. Research work by Horn and Schunck [14] as well as Lucas and Kanade [15] are considered pioneering approaches to solving optical problems with differential techniques.
The latest application of the BOS technique was presented in 2016 by Mier and Hayasaka et al, also by Hendiger in the year 2020. Hayasaka explained the BOS system's ability to extract information from density gradients in small sizes. In this study, the BOS method was used to study the underwater shock wave generated by

a laser by identifying the displacement vectors of local density gradients of water to obtain the pressure field. Hayasaka's experiment showed the advantage of the optical flow over the PIV method (cross correlation) in terms of resolution.

Meir used simple image subtraction to explore the use of colour gradient backgrounds as an alternative that eliminates the need to perform a complex image correlation between the digital images while Hendiger [28] applied the BOS technique to test the temperature limit of a non-isothermal ventilation jet used in ventilation, where low temperature difference poses a challenge.

The main researchers' important contributions to current BOS technology are shown in Table 3.2.

Table 3.2: Researchers and their contribution to today's BOS..

Authers/year	**Contributions**	**Constraints**
Schardin/1942 [2, 12]	The refractive objects are based on their distortion of a patterned background.	Provide qualitative measurements only
Kopf /1972 [3]	Measured density field by using the displacement of a laser speckle pattern caused by a candle flame.	–
Dalziel/1998 [6]	Reported BOS as 'Synthetic Schlieren'.	Qualitative measurements only
Meier/ 1999 [5]	Invented and applied for BOS patent.	Provide qualitative measurements only
Sutherland et. al/1999 [16]	Measure density and velocity fields of internal waves in a stratified fluid using 'synthetic Schlieren'	The light deflection integrated along the optical path provides only two-dimensional measurements.
Richard et. al /2000 [17]	Attempted to investigate BOS applications in a supersonic jet, turbulent flame and the blade tip vortices a helicopter.	Provide qualitative information only
Augensteine et.al/2001 [18]	Compared holographic filters with BOS	–
H Richard and M Raffel /2001 [19]	Demonstrated use of BOS to study compressible vortices of a helicopter blade	Provide qualitative measurements only
Klinge et.al 2002 [20]	Measured local density information of a helium jet using BOS.	Used an Abel inversion reconstruction technique, a technique that is sensitive to noise.

Table 3.3: Researchers and their contribution to today's BOS. Continued...

Authors/year	Contributions	Constraints
Klinge et. al/2004 [10]	Uses BOS and PIV to measure velocity and density of a wing tip vortex created by an aerodynamic profile. Computed optimal BOS setup. Uses "Abel Inversion" to reconstruct the index of refraction.	Velocity was measured using PIV technique, while BOS was only used to measure density.
Elsinga et. al /2004 [21]	Evaluated and compared applications of BOS and color Schlieren.	–
Venkatakrishnan and Meier/ 2004 [8]	Used inverse tomographic algorithms to re-construct two-dimensional slices from a three-dimensional flow using a cone-cylinder model.	Used a Poisson equation to calculate the density field. Then used the gradient information from the BOS method in the back-filtered projection algorithm.
Goldhahn and Seume/2007 [9]	Investigated the sensitivity, accuracy and resolution of BOS in 3D density fields. Calculated 3D density field directly from the deflection angle using computed tomography.	Only density field variations were measured.
Leopold/2007 [22]	Applied colored background pattern to increase the resolution of the BOS system.	–
Kindler et. al/2007 [23]	Applied BOS and computer tomography to examine the vortex measurement of the rotor blade tip.	–
Baur and Tapee /2002 [25]	Examined the system sensitivity and the effective distances between BOS devices.	No thermodynamic parameters were measured
Atcheson et.al/2008 [13]	Evaluated optimal optical flow algorithm for estimating deflection vectors in BOS.	–
Mier/2016 [27]	Used simple image subtraction to explore the use of colour gradient backgrounds.	–
Hayasaka/2016 [26]	Extract information from density gradients in small sizes	Density
Hendiger/2020 [28]	Applied the BOS technique to test the temperature limit of a non-isothermal ventilation jet used in ventilation.	Temperature

These experiments describe the computational effort required for the subsequent quantitative determination of the refractive index, temperature and density.

3.5 Fringe Deflection

A lot of research has been done into Fringe Deflection technique. Over the past couple of years, Fringe Deflection techniques have been used to analyze various physical phenomena. This section provides an overview of the literature on what has been done with the FD technique.

In 1970, W.Z. Black and W.W. Carr [30]investigated a differential interferometer that generates temperature-dependent fringe shift, to recent applications by B. Barrientos, C. Mares, D. Sarocchi, M. Cerca, and R Vaklivia in 2019 [36] where they used fringe projection for $3D$ displacement measurement in dry granular avalanche models, and J. Yu, N. Gao, J. Zhang, and Z. Meng in 2020 where they investigated the phase sensitivity and precision in the shape restoration of $3D$ diffused objects in fringe projection profilometry. Table 3.4 shows the Fringe Deflection research conducted and its application over the years.

Table 3.4: Researchers and their contribution to today's BOS. Continued...

Authors/year	Contributions	Constraints
W.Z. Black and W.W. Carr /1970 [30]	Investigated a differential interferometer that produces a fringe shift that is a function of temperature gradient. The described interferometer is capable of producing an infinite fringe pattern in which fringe lines corresponds to lines of constant index of refraction gradients.	Index of refraction gradients.
O. Kafri / 1980 [31]	Described a novel quantitative method for mapping ray deflections of a collimated beam of light.	Refractive index was measured.
M. Takeda, H. Ina, and S. Kobayashi / 1982 [34]	Computer processing of a non-contour-like fringe pattern than automatically distinguishes between the elevation and depression of objects or shape of a wavefront.	-
D.J. Bone, H.-A. Bacher and R.J. Sandeman / 1986 [33]	Refinement of the Fourier transform for fringe pattern analysis to include a 2D Fourier transform. The 2D transformation enables a better separation of the desired information components from the undesired components than the 1-D transformation.	Only refractive index was measured.
R.E. Peale and P.L. Summers /1996	Modification of schlieren optics for industrial gas-leak detection.	
César D. Perciante and José A. Ferrari / 2000 [29]	Applied phase gradient extraction algorithm that does not require the calculation of a Fourier transform of the images, which is performed only by subtracting images. Uses a periodic pattern in two orthogonal directions.	Only refractive index variations were measured.
K. Hatanaka and T. Saito /2015 [35]	Used periodic pattern with multiple scales(multifrequency).	density was extracted from the phase.
B. Barrientos, C. Mares, D. Sarocchi, M. Cerca, and R. Valdivia / 2019 [36]	investigated the feasibility of measuring 3D displacements in dry granular avalanche models using simultaneous fringe projection and digital image correlation.	Displacements were measured.
J. Yu, N. Gao, J. Zhang, and Z. Meng / 2020 [37]	Investigated the phase sensitivity and accuracy when retriving three-dimensional (3D) shape of diffused objects in fringe projection profilometry (FPP). Proposed a novel method to obtain 3D shapes with high accuracy by combining the optimal fringe frequency and the fringe direction (OFF + OFD).	-

3.6 Summary and Conclusion

In recent years, the Background Oriented Schlieren (BOS) technique has received great interest for its ability to provide quantitative data in refractive index variation in flow fields. One of the main advantages of BOS technique, the reduced optical access requirements, promotes its use in harsh industrial environments and complex structures. It turns out that the ideal recording and evaluation methods for the quantitative determination of density fields and density gradients have not yet been found. Currently, white-light background illumination, gray-scale recording, cross-correlation assessment, and tomographic analysis are the most common techniques for recording and evaluating quantitative measurements.

The Background Oriented Schlieren (BOS) technology has received great interest in recent years due to its ability to provide quantitative data on refractive changes in flow fields. After the first (e.g. Dalzie et al. 2000; Richard and Raffel 2001; Meier 2002) publications, more recent publications have focused on the precise modeling (Godhahn and Seume 2007) and validation (Elsinga et al. 2004) of the technique, but the basic technique has not undergone many changes or improvements. The latest and most significant advances in Background Oriented Schlieren techniques is the development of the Light-Field BOS (LF-BOS). The Light-Field BOS uses a $4D$ light probe instead of a static image, to create Schlieren images. The rays emitted by the probe are optically encoded with color and intensity variations, which provides a very accurate way of estimating and analyzing the deflection of the rays of a Schlieren object. The advantages of the $LF-BOS$ are the portability and functionality of the hand-held system, as well as low monitoring costs and minimal calibration. Fringe deflection techniques have also been extensively studied and implemented in analytical applications, with an emphasis on temperature measurements.

This literature review chapter contained a significant number of studies on cross-correlated image analysis methods, which provided a mathematical background for evaluating performance and identifying some of the limitations, accuracy and robustness of the BOS and FD techniques. However, further research is needed to more clearly categorize the difficulties encountered during temperature measurement and Helmholtz resonator optimization.

Bibliography

[1] J. N. Forkey, W. R. Lempert, and R. B. Miles, "Accuracy limits for planar measurements of flow field velocity, temperature and pressure using filtered Rayleigh scattering", Exp. Fluids, 24, 151-162 (1998).

[2] H. Schardin, "Schlieren Methods and Their Applications," Ergebnisse der Exakten Naturwissenschaften, Vol. 20, 303-439, (English translation: NASA TT F-12,732) (1942).

[3] U. Kopf, "Application of speckling for measuring the deflection of laser light by phase objects", Opt. Commun., 5, 347-350 (1972).

[4] M. Skotinov, "Quantitative Schlieren methods in gas Dynamics", Nauka, Moskow USSR, 1st edition (1976).

[5] G. E. A Meier, "Hintergrund Schlierenmessverfahren", Deutsche Patentanmeldung, DE 199 42 856 A1 (1999).

[6] S. B. Dalziel, G. O. Hughes and B. R. Sutherland, "Synthetic Schlieren", Proc. of 8th International Symposium on Flow Visualization, Sorrento, Italy, 1-4 September (1998).

[7] G. S. Settles, "Recent Developments in Schlieren and Shadowgraph Techniques", Proc. of 14th International Symposium on Flow Visualization, Dageu, Korea Italy, 21-24 June (2010).

[8] L. Venkatakrishnan and G. E. A. Meier , "Density Measurements Using The Background Oriented Schlieren Technique", Exp. Fluids , 37, 237-247 (2004).

[9] E. Goldhahn , and J. Seume , "Quantitative Measurements of Three-Dimensional Density Fields Using the Background Oriented Schlieren Technique", Exp Fluids, 43, 241-249 (2007).

[10] F. Klinge, T. Kirmse, and J. Kompenhans, "Investigation of the density and velocity distribution of a wing tip vortex by means of stereoscopic Background Oriented Schlieren Method (BOS) and stereoscopic Particle Image Velocimetry (PIV)", Proc. of 12th International Symposium on Application of Laser Techniques to Fluid Mechanics, Lisbon, Portugal (2004).

[11] F. Klinge, "Fluid flow rate determining method, involves tracing spatial offset of density variations based on images taken at different times, and determining local flow rate of fluid from offset and interval of times", Patent document DE102006047286 (2008).

[12] B. Atcheson, "Schlieren-Based Flow Imaging, MSC Dissertation", The University Of British Columbia, Canada (2007).

[13] B. Atcheson, W. Heidrich, and I. Ihrke, "An evaluation of optical flow algorithms for Background oriented Schlieren", Exp. Fluids, 46, 467-477 (2008).

[14] B. K. P Horn and B. G. Schunuck, "Determining optical flow", Artificial Intelligence, 17, 185-203 (1981).

[15] B. D. Lucas and T. Kanade, "An iterative image registration technique with an application to stereo vision", Proc. of DARPA IU Workshop, 121-130 (1981).

[16] B. R. Sutherland, S. B. Dalziel, G. O. Hughes, and P. F. Linden, "Visualization and measurement of internal gravity waves by 'Synthetic Schlieren', part I: Vertically oscillating cylinder", J Fluid Mech 390:93–126 (1999).

[17] H. Richard, M. Raffael, J. Kompenhans J, and G.E.A. Meier, "Demonstartion of the Pplicability of a background Oriented Schlieren (BOS) Method", Proc. of 10th Int Symp Appl Laser Techniques to Fluid Mechanics, Lisbon, Portugal (2000).

[18] E. Augenstein, F. Leopold, H. Richard, and M. Raffel, "The background oriented schlieren method versus visualization with holographic filters", Proc. of 4th international symposium on particle image velocimetry, Göttingen, Germany (2001).

[19] H. Richard and M. Raffel, "Principle and applications of the background oriented Schlieren Methods", Meas. Sci. Technol, 12, 1576-1585 (2001).

[20] F. Klinge and M. Reithmuller, "Local density information on application obtained by means of background oriented schlieren(BOS) method", Proc of 11th International Symposium on Application of Laser Technology to Fluid Mechanics, Lisbon, Portugal (2002).

[21] G.E. Elsinga, B.W. van Oudheusden, F. Scarano, and D.W. Watt, "Assessment and application of quantitative schlieren methods: Calibrated color schlieren and background oriented schlieren," Exp. Fluids 36, 309–325(2004).

[22] F. Leopold, "The Application of the Colored Background Oriented Schlieren Technique (CBOS) to Free-Flight and In-Flight Measurements", Proc of. Int. Conf. on Instrumentation in Aerospace Simulation Facilities, Pacific Groove, CA USA (2007).

[23] K. Kindler, E. Goldhahn, F. Leopold and M. Raffel, "Recent developments in background oriented Schlieren methods for rotor blade tip vortex measurements", Exp. Fluids 43, 233–240 (2007).

[24] K. Berger, I. Ihrke, B. Atcheson, W. Heidrich, and M. Magnor, "Tomographic 4D Reconstruction of Gas Flows in the Presence of Occluders," Proc. of the Vision, Modeling, and Visualization Workshop, Braunschweig, Germany, November 16-18 (2009).

[25] L. Baur and J. Tapee, "Background Oriented Schlieren", Technical Report AAE 490R/590R, Purdue University (2002).

[26] Y. T. T. L. M. k. K. Hayasaka, "Measurment of a laser-induced underwater shock wave by the optical-flow-based background- oriented schlieren technique", in 18th International Symposium on the Application pf laser and imaging Techniques to Fluid mechanics, LISBON, PORTUGAL (2016).

[27] F.A. Mier, and M.J. Hargather, "Color gradient background-oriented schlieren imaging",Springer-Verlag Berlin Heidelberg (2016)

[28] J. Hendiger, M. Chludzinska, and P Zietek, "Assessment of the background oriented schlieren application in testing the temperature limitof an axisymmetric ventilation jet", Environmental Engineering, Warsaw University of Technology, Air Condition and Heating Department, Porland (2020).

[29] César D. Perciante and José A. Ferrari, "Visualization of two-dimensional phase gradients by subtraction of a reference periodic pattern", (2000).

[30] W. Z. Black, and W.W. Carr, "Application of a Differential Interferometer to the Measurement of Heat Transfer Coefficients", Review of Scientific Instruments, 42(3), 337 (1971).

[31] O. Kafri, "Noncoherent method for mapping phase objects", Opt. Lett. 5, 555–557 (1980).

[32] R. E. Peale and P. L. Summers, "Zebra schlieren optics for leak detection", Appl. Opt. 35, 4518–4521 (1996).

[33] D. J. Bone, H.-A. Bacher, and R. J. Sandeman, "Fringe-pattern analysis using a 2-D Fourier transform", Appl. Opt. 25, 1653–1660 (1986).

[34] M. Takeda, H. Ina, and S. Kobayashi, "Fourier-transform method of fringe-pattern analysis for computer-based topography and interferometry", JOSA 72:156–160 (1982).

[35] K. Hatanaka and T. Saito, "Background oriented schlieren method using multi-scale periodic pattern", in 29th International Symposium on Shock Waves 1, 453–458, Springer International Publishing, Switzerland (2015).

[36] B. Barrientos, C. Mares, D. Sarocchi, M. Cerca, and R Valdivia, "Dynamic three-dimensional displacement analysis of small-scale granular flows by fringe projection and digital image correlation", Springer-Verlag GmbH Germany part of Springer Nature (2019).

[37] J. Yu, N. Gao, Z. Zhang, and Z. Meng, "High Sensitivity Fringe Projection Profilometry Combining Optimal Fringe Frequency and Optimal Fringe Direction", Optics and Lasers in Engineering, 129, 106068 (2020)

Chapter 4

Numerical Simulation

Contents

For the numerical simulations presented, a phase object is considered, which is indicated by a Gaussian distribution of the change in refractive index. The Gaussian refractive index distribution is the first approximation representing objects of axisymmetric degree, such as the gas jet emitted by a gas burner. To analyze the most important parameters, a series of simulations were performed to obtain the temperature, for the BOS technique, the particles are generated randomly. The **MatLab R2018a** software was used in the different simulations.
While this approach provides idealized conditions that are different from those encountered during the experiment, this strategy, however, allows for performance evaluation with complete control over the image parameters.

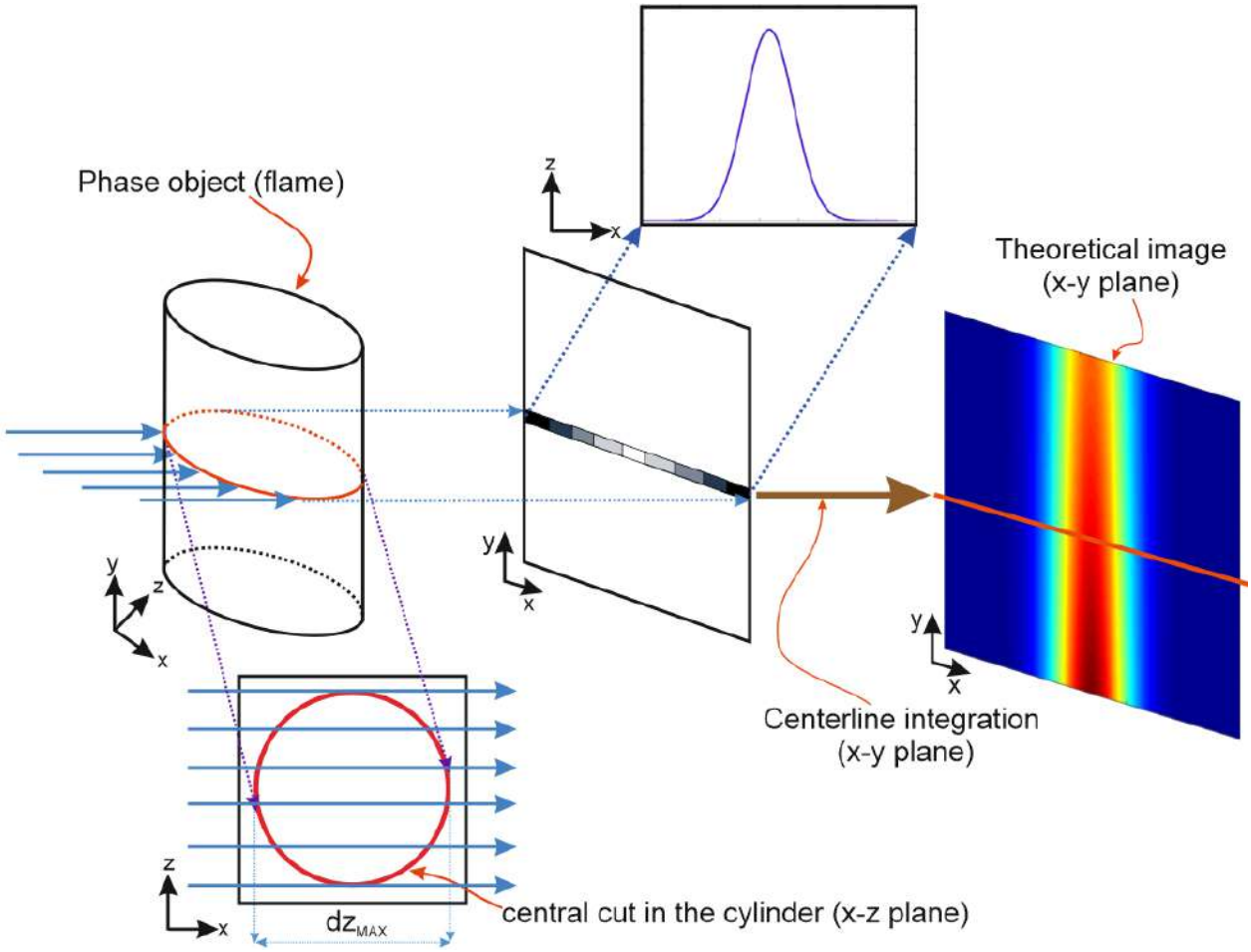

Figure 4.0.1: Flame object with longitudinal transverse as Gaussian function.

$Figure$ 4.0.1 shows the center line of the generated change in Refractive Index Δn image in the horizontal direction.

4.1 Flame Simulation

In this Chapter, the numerical simulation is presented. The results of the numerical simulations allow the selection of the optimal parameters for the techniques.
The phase object has a volume formed by the $x-y-z$ planes, the refractive index distribution of which corresponds to the Gaussian function, in which all its values are known. The function is given as in $Eq.(2.4.28)$.

To simulate the Gaussian distribution of the refractive index, the radius is first required. $Figure\,4.1.1$ shows the simulated radius values in the range from $7.7mm$ to $12.6mm$. This radius is used in the computation of the refractive index. The radius of the Gaussian function varies roughly linearly to produce a well simulated and more realistic flame.

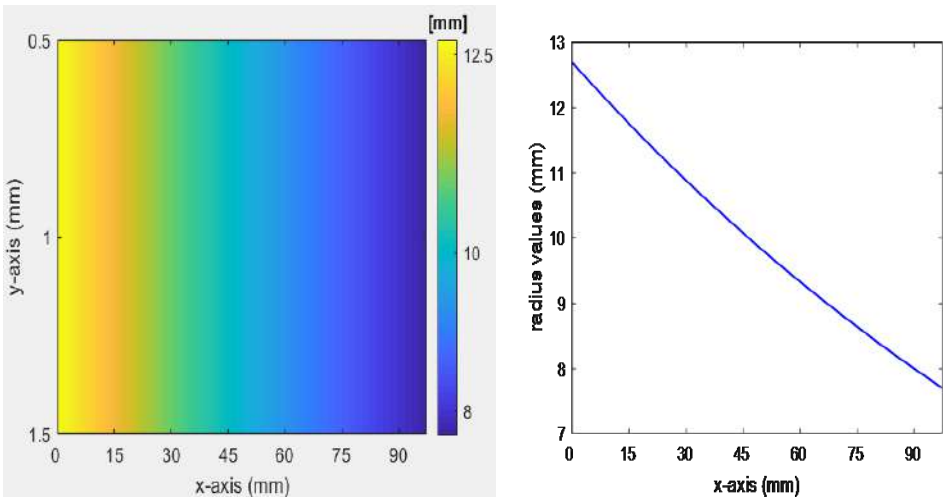

(a) Generated values of the radius. (b) Horizontal profile of the radius.

Figure 4.1.1: Simulated radius; a) generated values b) Horizontal profile of the radius.

$Figure\,4.1.2$ shows the top view of the generated Gaussian $\triangle n$ with the horizontal profile through the center line. To generate the Gaussian distribution, the equation parameters of $Eq.$(2.4.28) were set as; $\triangle n_0 = -1.69 \times 10^{-4}$, $L_x = 91mm$, $L_y = 91mm$, $(x_0, y_0) = (0, 0)$.

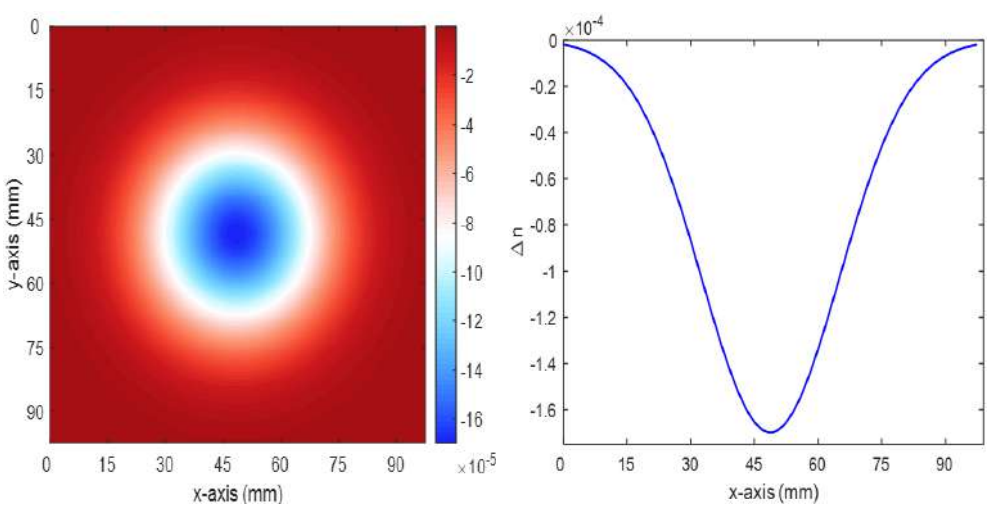

(a) cross-section through the origin. (b) Horizontal profile of the Gaussian flame.

Figure 4.1.2: Gaussian variation of the refractive index; a) Top view b) Horizontal profile through the center.

In this first part, a uniform flame in the y direction will be simulated, i.e. as if it were a cylinder and had a slightly varying width throughout the generation area. The temperature and density distributions can be calculated using

$Eq.$(2.3.8) and $Eq.$(2.3.12) respectively.

4.2 Simulation with Exponential Decaying Flame

To simulate a flame a scenario is considered that includes the maximum displacement of $1.5\ pix$ for $\triangle x$ and $0.6\ pix$ for $\triangle y$. $Figure$ 4.2.1(a) shows the generated refractive index of the exponential decaying flame. $Figure$ 4.2.1(b) shows the horizontal profile taken along row 1300, while $Figure$ 4.2.1(c) shows the vertical profile taken along column 650 in a $91mm \times 91mm$ image. The horizontal profile of $Figure$ 4.2.1(a) shows the decreasing refractive index at the depth at which the burning candle plume is located. The vertical profile running through the middle of $Figure$ 4.2.1(a) from top to bottom shows that the refractive index decreases towards the wick of the candle. The associated displacement field of each displacement component is shown in $Figure$ 4.2.2(a) and $Figure$ 4.2.3(a), respectively.

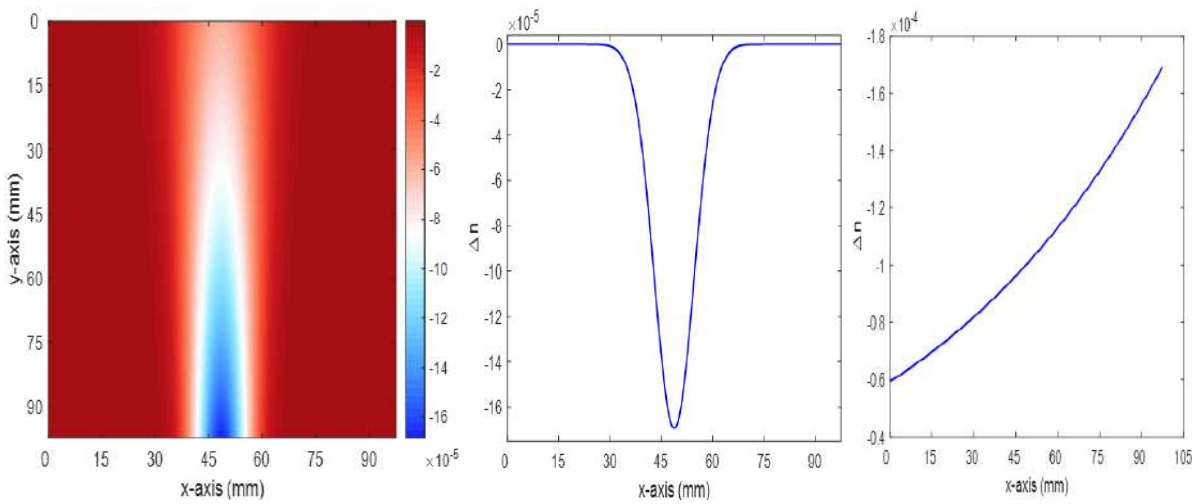

(a) Decaying flame (b) Horizontal profile (c) Vertical profile

Figure 4.2.1: Simulated $\triangle n$; $a)$ decaying flame and $b)$ horizontal profile, $c)$ vertical profile

$Eq.$(2.4.29) and $Eq.$(2.4.31), respectively, generate the x and y components of the displacement as shown in $Figure$ 4.2.2(a) and $Figure$ 4.2.3(a). These displacements are marked as the given displacements.
Illustrated in $Figure$ 4.2.2(a) is the change in the x-direction, in m, with its horizontal profile in $Figure$ 4.2.2(b).

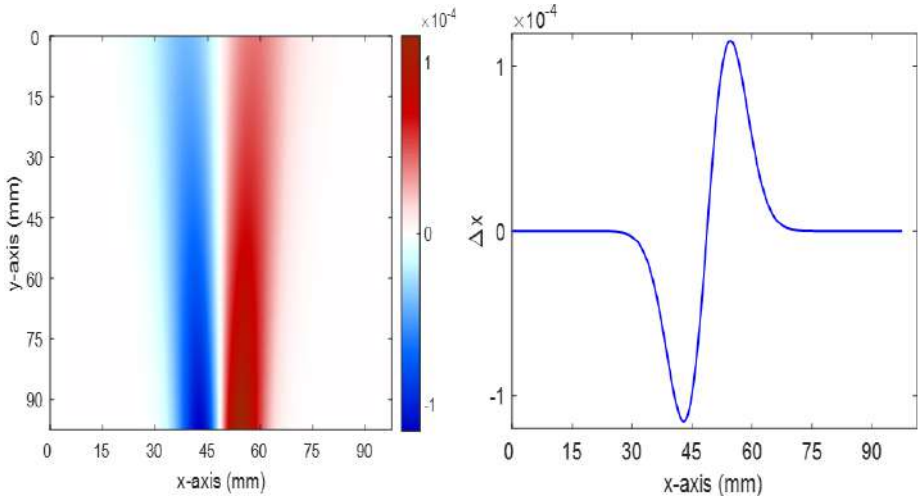

(a) Change in x ($\triangle x$), in m. (b) Horizontal profile of $\triangle x$

Figure 4.2.2: Change in displacement in the x direction, in m; $a)$ $\triangle x$ and $b)$ horizontal profile.

$Figure 4.2.3$ shows the change in displacement in the $y-$direction , in m, also shown is the horizontal and vertical profile, respectively.

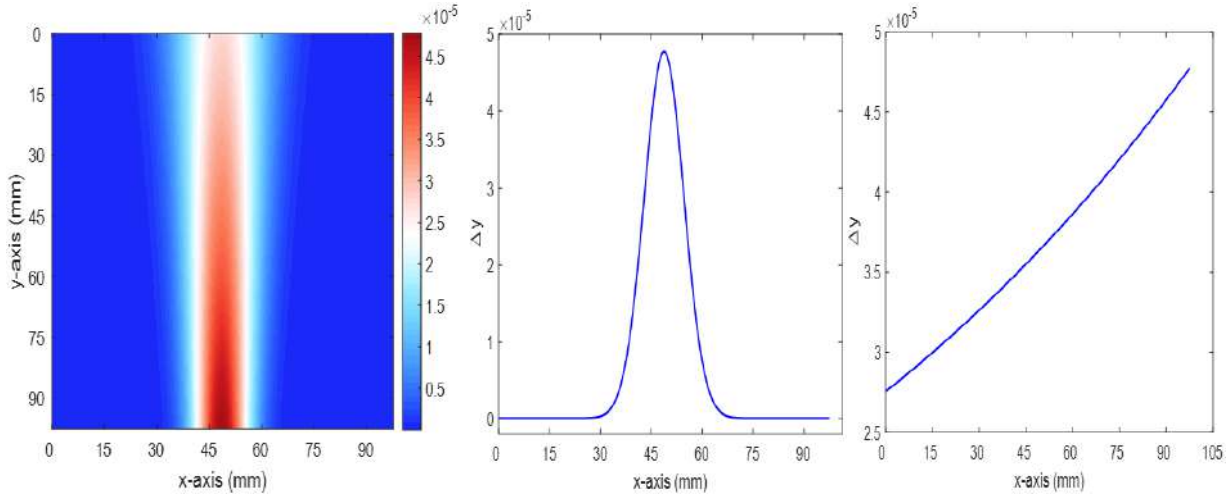

(a) Change in y, in m. (b) Horizontal profile (c) Vertical profile

Figure 4.2.3: Change in displacement in the y direction, in m; $a)$ $\triangle y$, $b)$ horizontal profile and $c)$ vertical profile.

As seen in the vertical cross section view, the variation is maintained to be exponential because the derivative of the exponential term creates this variation.

By considering the change in x and y in each pixel, the displacement vector in each pixel can be plotted. The length of each vector depicts the extent of each displacement as depicted in $Figure\,4.2.4(b)$, which is the results of the Gaussian distribution derivatives of the refractive index $Eq.$(2.4.28), plotted with the Matlab function $quiver$. $Figure\,4.2.4(a)$ shows a $3D$ construction of the refractive index.

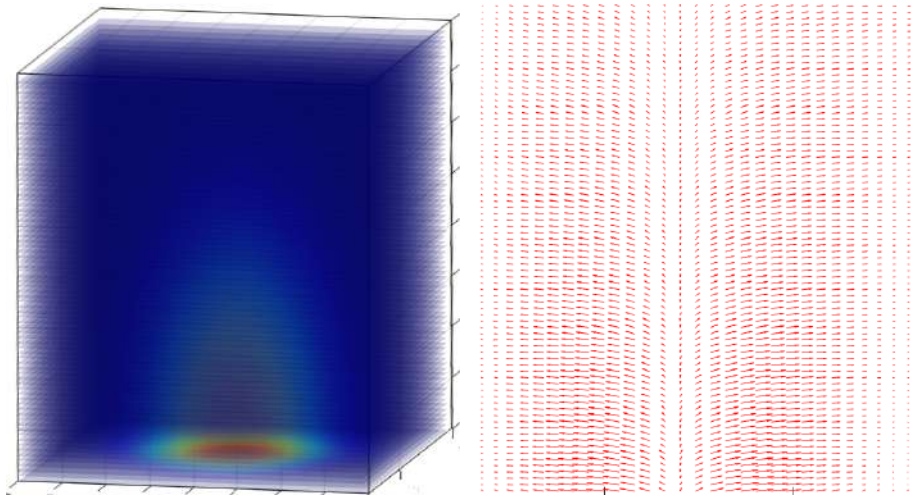

(a) 3D distribution of the refractive index (b) Displacement Vectors; the maximum vector is equivalent to $2.0pix$.

Figure 4.2.4: Simulated plume; a) 3D distribution of the refractive index variation, and$b$) Resulting displacement field of the background plane.

To illustrate the basic idea, a $2D$ Gaussian distribution curve is shown in $Figure$ 4.2.5. In order to generate a $3D$ of the Gaussian distribution, the curve is translated to the 3rd axis.

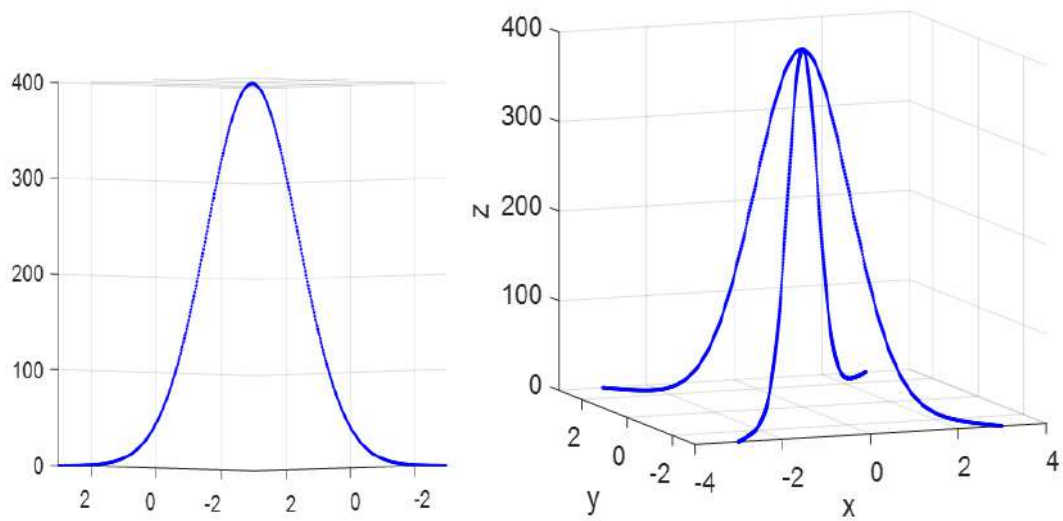

(a) 2D Gaussian distribution curve (b) Reconstructed 3D curve

Figure 4.2.5: 3D re-construction a) 2D and b) 3D

$Figure$ 4.2.5(a) shows a $2D$ Gaussian distribution curve, in $Figure$ 4.2.5(b) the same $2D$ is shifted along the 3rd axis in order to form a $3D$ Gaussian distribution. For the sake of clarity, only a few lines of the $3D$ distribution curve are shown.

The calculated temperature map is shown in $Figure$ 4.2.6, displaying the simulated temperature T calculated with $Eq.$(2.3.8). The maximum temperature is $\approx 1000°C$, while the minimum is at room temperature $\approx 25°C$.

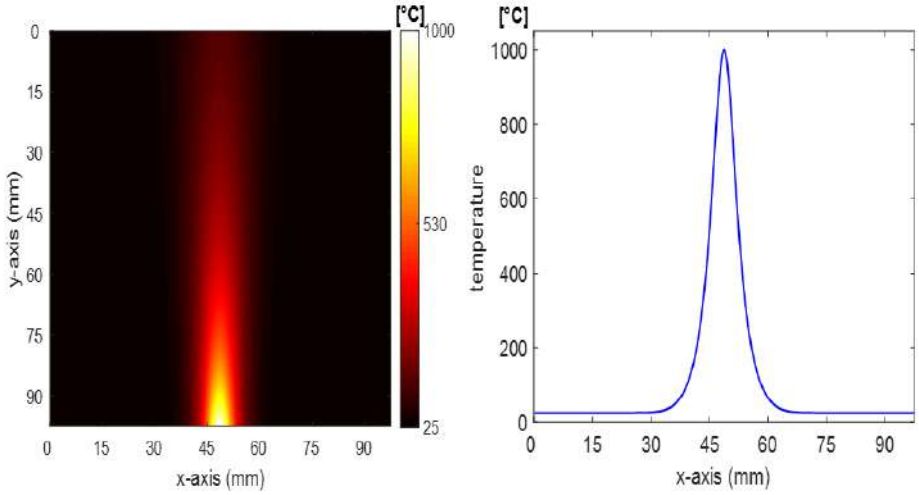

(a) Temperature variation (b) Horizontal profile

Figure 4.2.6: Simulated; $a)$ Temperature variation ΔT and $b)$ horizontal profile.

The density is calculated from the refractive index using the Gladstone-Dale equation $Eq.(2.3.2)$ which can be arranged as $\rho = \frac{n-1}{K}$. Simulated density ranges from 0.25 to $0.95 \frac{kg}{m^3}$.

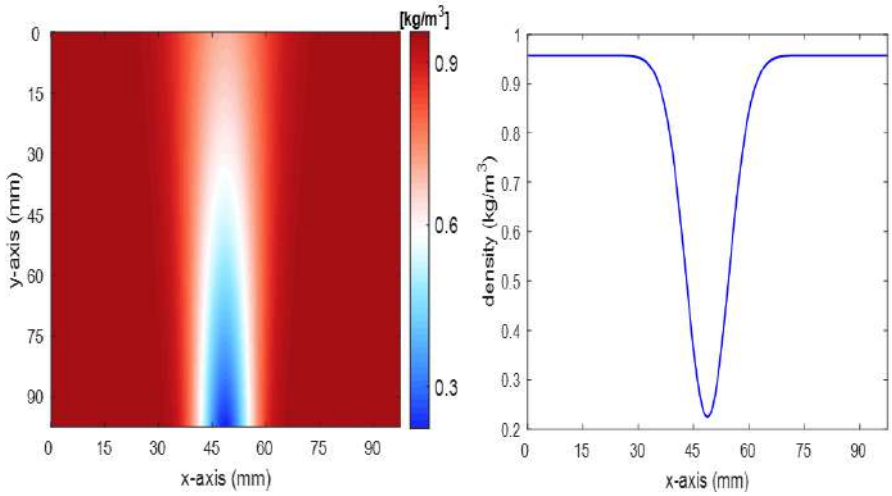

(a) Density variation (b) Horizontal profile of the density

Figure 4.2.7: Simulated; $a)$ density variation ρ and $b)$ horizontal profile

4.3 BOS Simulation

A simulation of the BOS experiment is performed to predict the theoretical precision of the Schlieren method under ideal conditions. BOS images are generated. The synthetic images are analysed to obtain the Refractive Index, temperature variation and density field for the simulated experiment.

To simulate the BOS method, a reference BOS image composed of 89500 computer-generated Gaussian particles, with coordinate centers randomly selected in a region of $91mm \times 91mm$, shown in $Figure\ 4.3.1(a)$, while in

$Figure$ 4.3.1(b) is the image with the particles displaced with their Δx and Δy respectively. The displacement image $Figure$ 4.3.1(b) was generated by adding the particle displacement Δx and Δy to the corresponding reference center coordinates, however, the displacement of the particles, as shown in the figure, is not visible to the naked eye. The displaced image and the reference image are then used to calculate the corresponding displacement fields using the Fourier transform algorithm.

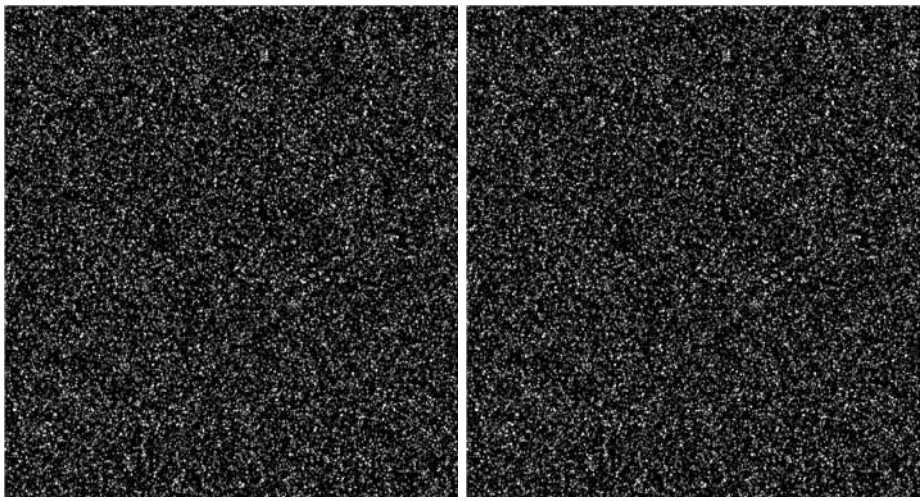

(a) Reference Image (b) Displaced BOS particles

Figure 4.3.1: Generated BOS particles; a) Reference Image, b) Displaced Particles

An artificial image was created to mimic the image obtained from the actual implementation of the BOS (PIV). The density of the dots was chosen as high as possible. The size of the interrogation window is limited by the particle spacing, therefore, a high seeding density is a desirable condition.

The image is computer digitized with a sampling of $91mm \times 91mm$, where the sample represent the display area. In this array matrix of $91mm \times 91mm$, the objects shown in the image are hypothetical particles of different sizes and positions, embedded in an ideal black background, shown in $Figure$ 4.3.1. To achieve a realistic background, the artificial images are modified by adding additive Gaussian noise. The intensity of the pixels representing an object (particle) in the gray scale follows a Gaussian function, supported by:

$$I(x,y) = I_0 exp\left[-\frac{(x-x_0)^2/a^2 + (y-y_0)^2/b^2}{2d_0^2}\right], \tag{4.3.1}$$

where $I(x,y)$ is the gray scale intensity at the position (x,y) in pixels, (x_0,y_0) is the position of the object's centroid, I_0 is the maximum intensity of the object, a and b are parameters to modify the shape and the d_0 parameter is the particle diameter in pixels. The image was generated based on a specific set of parameters. These includes the number of particles ($N_p = 89500$), minimum and maximum radius for particles ($d_{r_{min}}, d_{r_{max}}$), minimum and maximum gray scale intensity ($I_{p_{min}}, I_{p_{max}}$) and the image size in the x and y direction ($L_x = 91mm, L_y = 91mm$).

Since physically all permitted values of the (x_0) and (y_0) coordinates are equally likely to occur, the coordinates of the object's center were generated by a random number generator. In particular, the coordinates of the center of each object are calculated as follows:

$$x_0(i) = \xi L_x \; and \; y_0(i) = \xi L_y, \tag{4.3.2}$$

where ξ is a uniform randomly distributed deviation, where values between 0.0 and 1.0 are assumed, x_0 and y_0 are the coordinates of the center of object i. Likewise, the radius size of the object $\frac{d_0}{2}$ and its maximum gray scale I_0 are generated randomly.
One of the purposes of artificial images is to create velocity fields. The methodology employed is as follows:
From the Gaussian distribution of the refractive index function $Eq.$(2.4.28), the derivatives Δx and Δy were calculated, which resulted in $Eq.$(2.4.29) and $Eq.$(2.4.31) respectively. These values were then incorporated into each pixel of $Eq.$(4.3.1) as the x - and y - disturbances, which resulted in the displacement of the particles as shown in $Figure 4.3.1(b)$. The displacement vectors of the particle was then calculated and shown in $Figure$4.3.2 as the arrows.

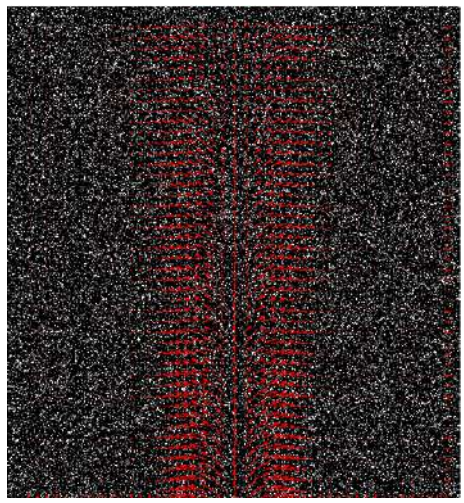

Figure 4.3.2: BOS reference pattern superimposed with the displacement vector field computed with the cross-correlation algorithm.

$Figure$ 4.3.2 shows the displacement vector field generated by the PIV cross-correlation analysis superimposed on the background pattern image. The arrows are pointing outward, with a region in the center with almost no displacement.

4.3.1 BOS Error Computation

To evaluate the robustness of the BOS method, random noise was added to the computed images. After adding the noise the process of recovering the components, Δx, Δn, ΔT, $\Delta \rho$ was initiated. The discrepancy between the original parameters (without the added noise) and the parameters with noise was calculated and reported.
This section assesses the robustness of BOS technique when the recorded images contain noise. To perform this simulation, random noise is generated and added to the captured images.

4.3.1.1 Change in Displacement Δx

The cross-correlation technique computes the displacements which are represented by the change is x (Δx). $Figure$ 4.3.3(a) show the recovered change in x after the noise amounting to 50% were added. $Figure$ 4.3.3(b) depicts the horizontal profile of the recovered Δx_{REC} compared to the original Δx_{SIM}. The red curve is the horizontal profile of Δx_{SIM} for the simulated reference, the blue curve is the horizontal profile of the calculated Δx_{REC}. The calculated Δx_{REC} differs from the simulated Δx_{SIM} by an error of 7.6%.

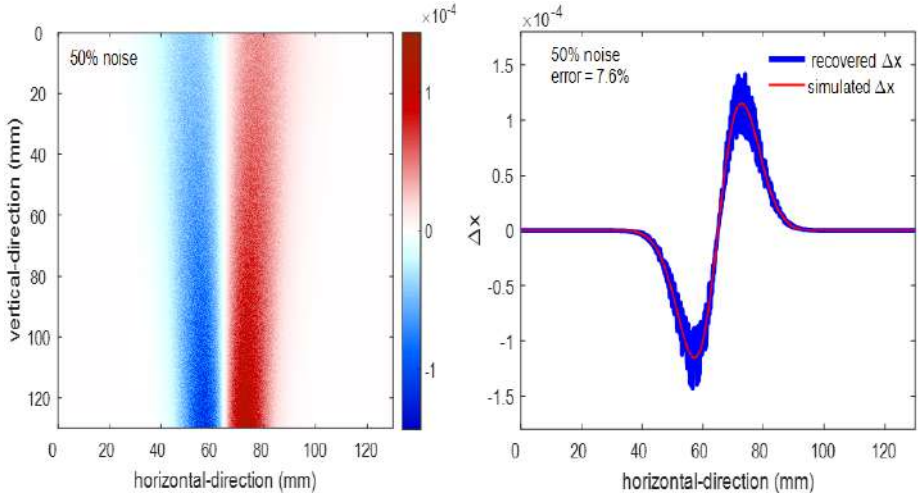

(a) Δx with 50% added noise (b) Horizontal profile of $\triangle x$

Figure 4.3.3: Δx $a)$ with 50% added noise , $b)$ horizontal profile.

As shown in the $Figure$ 4.3.4, the discrepancy between the recovered change in x and the original Δx amounts to 15.2% when the added random noise was set to 100%.

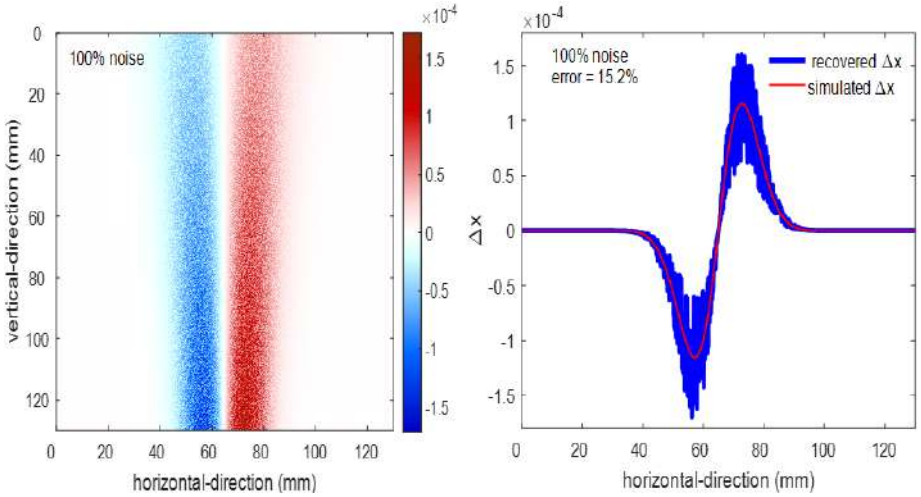

(a) Δx with 100% noise (b) Horizontal profile

Figure 4.3.4: Δx $a)$ with 100% added noise, $b)$ horizontal profile.

When the added random noise was set to generate 150% noise, the recovered Δx deviates by 22.0% error from the original Δx. The recovered parameter deviates more from the original parameter as the added noise is increased. The blue curve is the recorded $\triangle x$ parameter, and the red curve is the original simulated parameter.

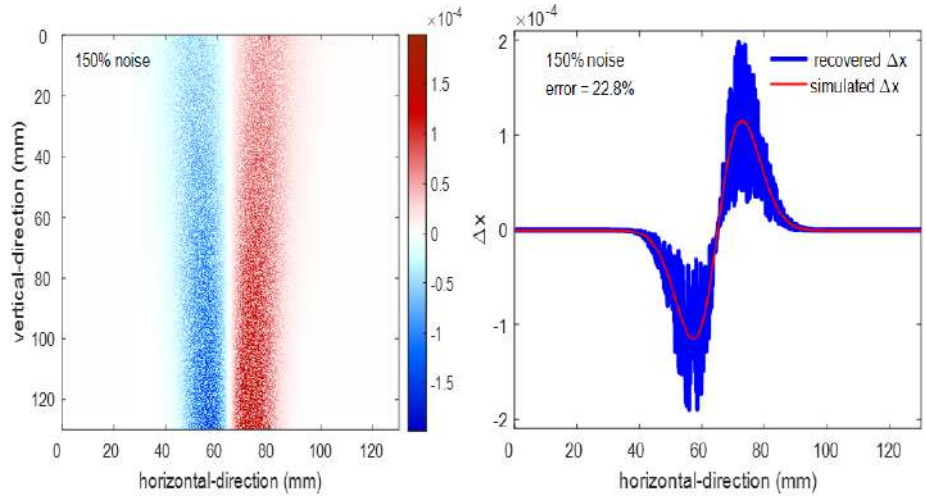

(a) Δx with noise (b) Horizontal profile

Figure 4.3.5: Δx $a)$ with 150% added noise $b)$ horizontal profile.

4.3.1.2 Radius Computation

Using $Eq.(2.7.1)$, a curve-fitting algorithm was implemented on $\triangle x$ to extract the radius, since recovering parameters such as $\triangle n$ requires that the radius be known in advance. The recovered radius is shown in $figure 4.3.6$ together with the simulated radius for comparison. The recovered radius is shown in blue curve with the simulated radius in red curve. There are small deviations between the simulated radius and the recovered radius, however the two curves are in the same range.

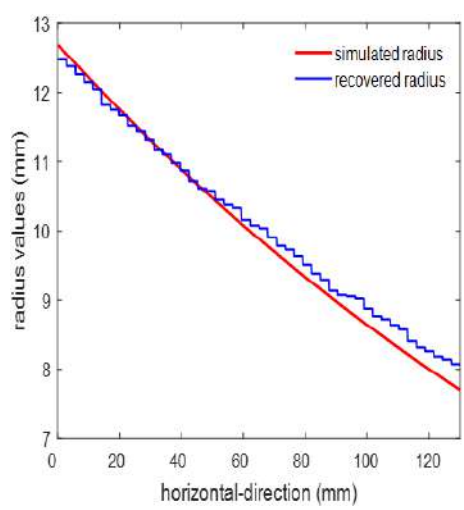

Figure 4.3.6: BOS recovered radius in blue curve with the simulated radius shown in red curve.

4.3.1.3 Change in Refractive Index Δn

The refractive index is reconstructed by two procedures as outline in Section 2.4.1, the first is by the integration procedure and the second is through dividing by x. $Figure$ 4.3.7 to $Figure$ 4.3.9 displays the errors generated when recovering the refractive index. $Figure$ 4.3.7(a) depicts the recovered change in refractive index Δn by

the integration procedure after noise amounting to 50% was added. The recovery of the refractive index by the division by x procedure is shown in $Figure$ 4.3.7(b). $Figure$ 4.3.7(c) demonstrates the comparison of the horizontal profiles between the original simulated Δn_{SIM} and the two recovered Δn. An error of 1.0% was recorded for the integration method and an error of 7.3% for division by x. The streaks in $Figure$ 4.3.7(a) are the result of the line-by-line integration process on the $\triangle x$ image. The streaks increases as the added noise increases.

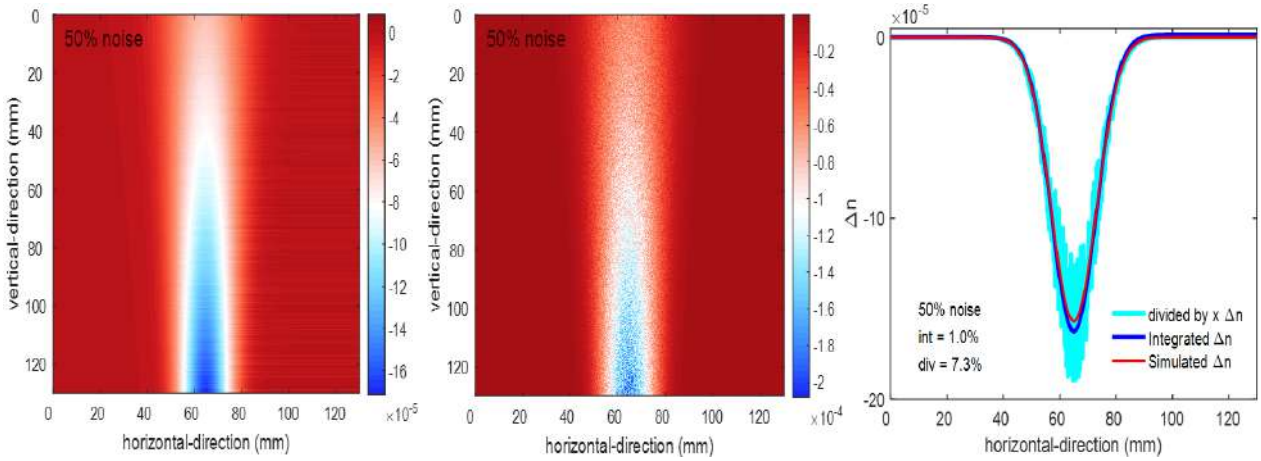

(a) Integrated (b) Divided by x (c) Horizontal profile comparison

Figure 4.3.7: Recovered Δn when 50% noise is added; a) by the integration method, b) by dividing by x method, and c) horizontal profile comparison.

The random noise generated was increased to 100% to determine how the algorithm would perform under these conditions. $Figure$ 4.3.8(a) is recovery of Δn by the integration method. $Figure$ 4.3.8(b) shows the recovered change in refractive index Δn by the dividing by x procedure. While $Figure$ 4.3.8(c) demonstrates the comparison of the horizontal profiles. The errors for the two methods of integration and division by x are 1.8% and 14.6%, respectively.

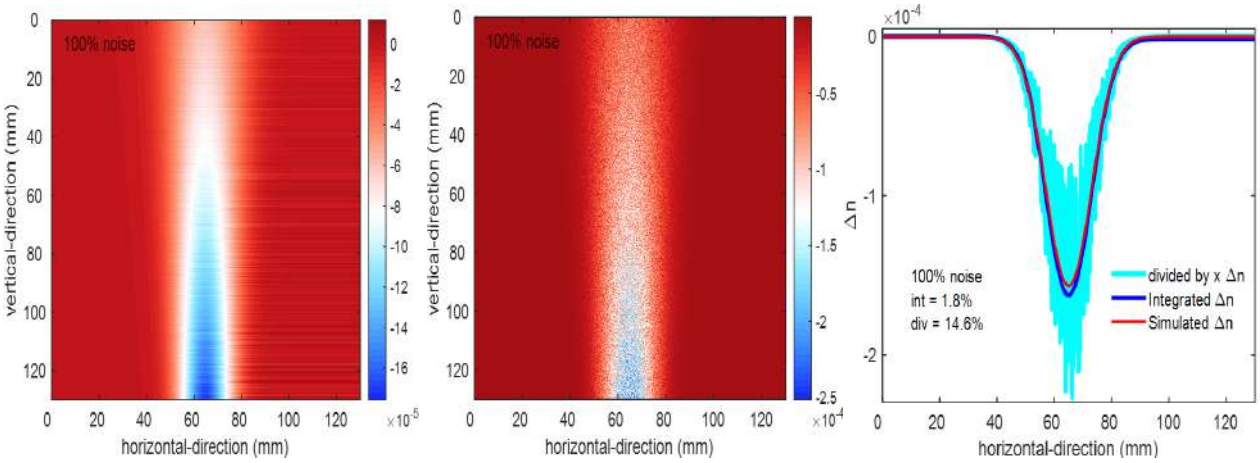

(a) Integrated (b) Divided by x (c) Horizontal profile comparison

Figure 4.3.8: Recovered Δn when 100% noise is added; a) by the integration method, b) by dividing by x method, and c) horizontal profile comparison.

In a 150% added noise, the calculated error is 2.2% for the integration method, while a 21.9% error is recorded for the method of division by x.

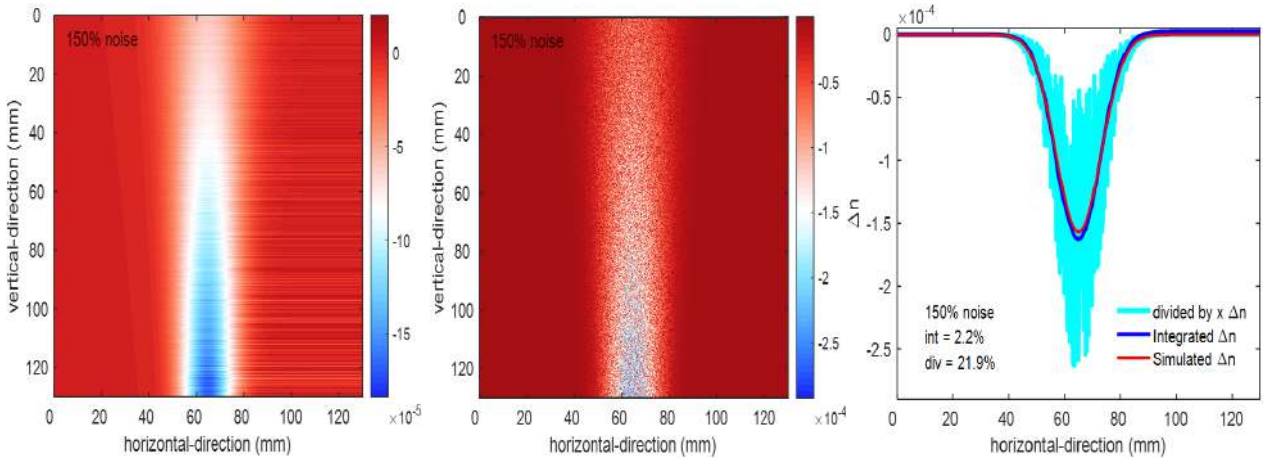

(a) Integrated (b) Divided by x (c) Horizontal profile comparison

Figure 4.3.9: Recovered change in Δn) when 150% noise is added; a) by the integration method, b) by dividing by x method, and c) horizontal profile comparison.

4.3.1.4 Change in Temperature ΔT

$Figure$ 4.3.10 to $Figure$ 4.3.12 shows the recovered Temperatures T computed from the recovered $\triangle n$ by using the equation $Eq.(2.3.8)$. The recovered Temperatures were computed after noise of 50%, 100% and 150% were added to $\triangle n$ to simulate a real situation in which noise is present. $Figure$ 4.3.10(a) show the recovered Temperature T by the integration procedure after noise amounting to 50% was added. In $Figure$ 4.3.10(b) the resulting Temperature recovered by the division by x method is depicted. The comparison of the horizontal profiles is shown in $Figure$ 4.3.10(c). The computation of the integration method causes an error of 0.5%, the x division procedure causes an error of 8.2%.

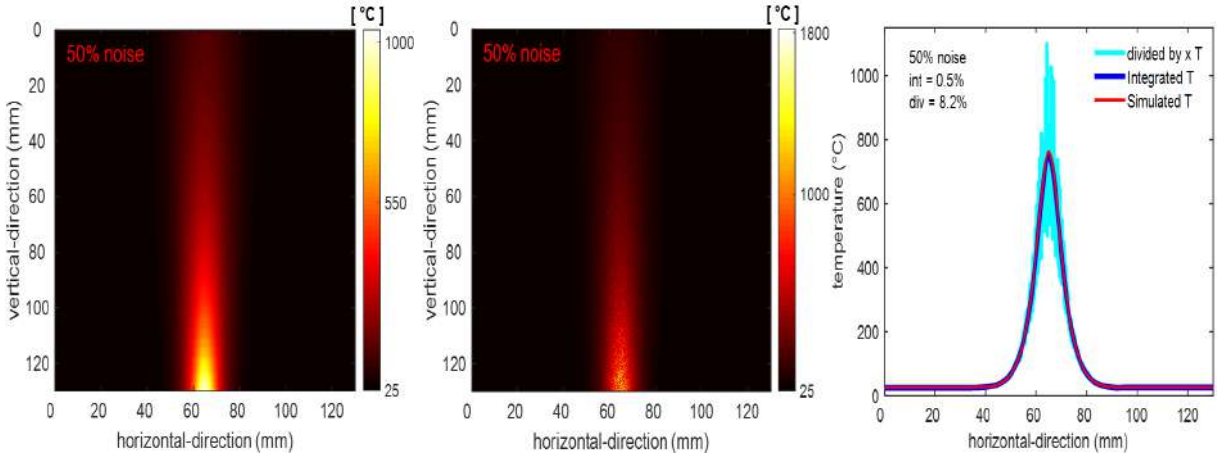

(a) Integrated (b) Divided by x (c) Horizontal profile comparison

Figure 4.3.10: Recovered T with 50% added noise; a) by the integration method, b) by dividing by x and c) is the horizontal profile comparison.

$Figure$ 4.3.11(a) shows the Temperature T recovered by the integration process after noise of 100% was added. $Figure$ 4.3.11(b) depicts the recovered Temperature T by the method of dividing by x. $Figure$ 4.3.11(c) is the horizontal profile comparisons. The integration procedure results in an error of 2.1%, while the division by x method gives errors amounting to 131.7%.

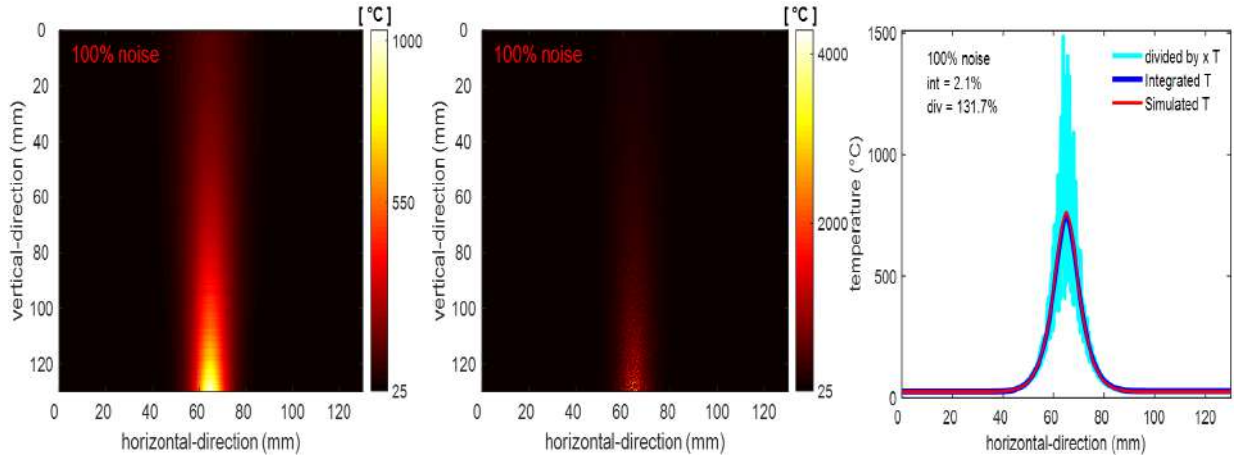

(a) Integrated (b) Divided by x (c) Horizontal profile comparison

Figure 4.3.11: Temperature T with 100% noise added; a) by the integration technique, b) by dividing by x , and c) horizontal profile comparison.

$Figure$ 4.3.12(a) show the recovered Temperature T by the integration procedure after noise of 150% was added. $Figure$ 4.3.12(b) depicts the recovered Temperature T by dividing by x. $Figure$ 4.3.12(c) demonstrates the comparison of the horizontal profiles. The computed error is 2.8% for the integration procedure, and an error of 413.0% is shown for the method of dividing by x.

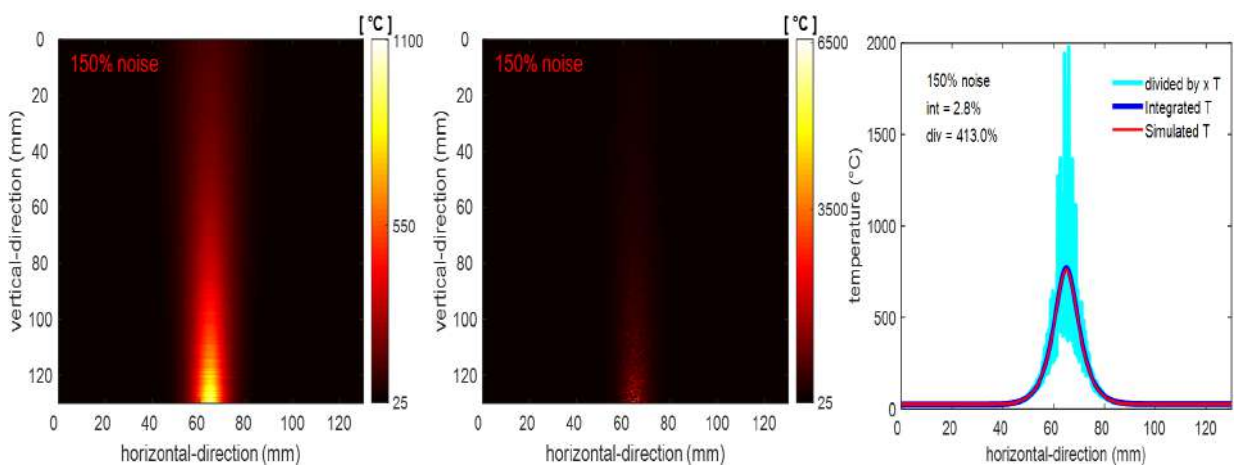

(a) Integrated (b) Divided by x (c) Horizontal profile comparison

Figure 4.3.12: Temperature T with 150% noise added; a) by the integration procedure, b) by dividing by x , and c) horizontal profile comparison.

4.3.1.5 Change in Density ρ

The density variation surrounding the simulated burning candle is analyzed and noise is added to simulate a scenario in which noise is present in an experimental evaluation. $Figure$ 4.3.13 to $Figure$ 4.3.15 presents the reconstructed density ρ computed by using $Eq.(2.3.12)$. $Figure$ 4.3.13(a) shows the recovered density ρ by the integration method after 50% noise is added. $Figure$ 4.3.13(b) presents the reconstructed density ρ where the method of dividing by x is used. To compare the recovered densities, a horizontal profile was draw through row 1200 of a $91mm \times 91mm$ image, $Figure$ 4.3.13(c) shows the comparison results. The computed error is 0.95% for the integration procedure, and an error of 2.6% is shown for the method of dividing by x.

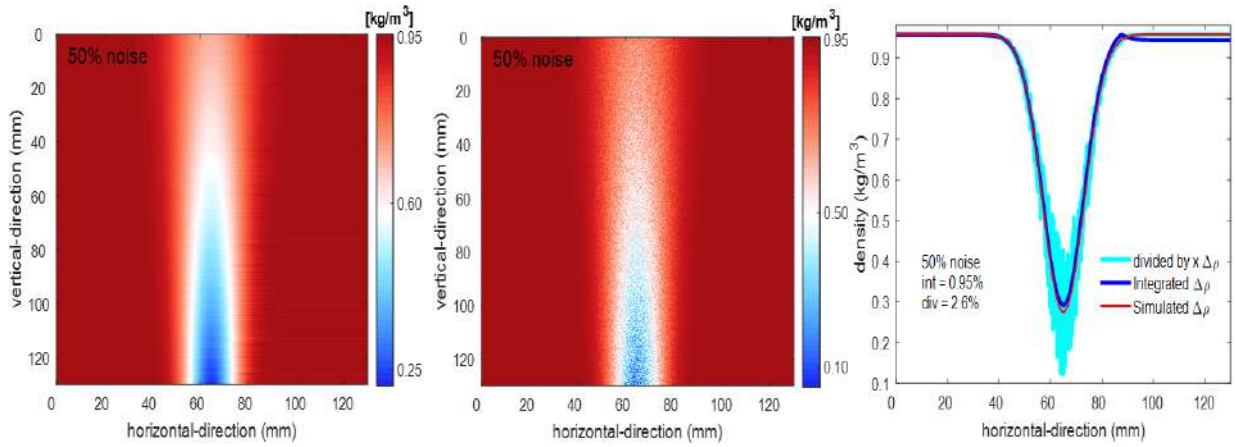

(a) Recovered ρ using integration method. (b) Recovered ρ by divided by x. (c) Horizontal profile comparison

Figure 4.3.13: Recovered ρ with 50% noise added; $a)$ by the integration method, $b)$ by dividing by x , and $c)$ horizontal profile comparison.

Adding 100% random noise results in $Figure$ 4.3.14. $Figure$ 4.3.14(a) shows the density ρ recovered by the integration process. $Figure$ 4.3.14(b) depicts the recovered density ρ by dividing by x. $Figure$ 4.3.14(c) is the horizontal profiles comparison. The recovered density has an error of 1.7% for the integration method and 5.1% for the method of division by x.

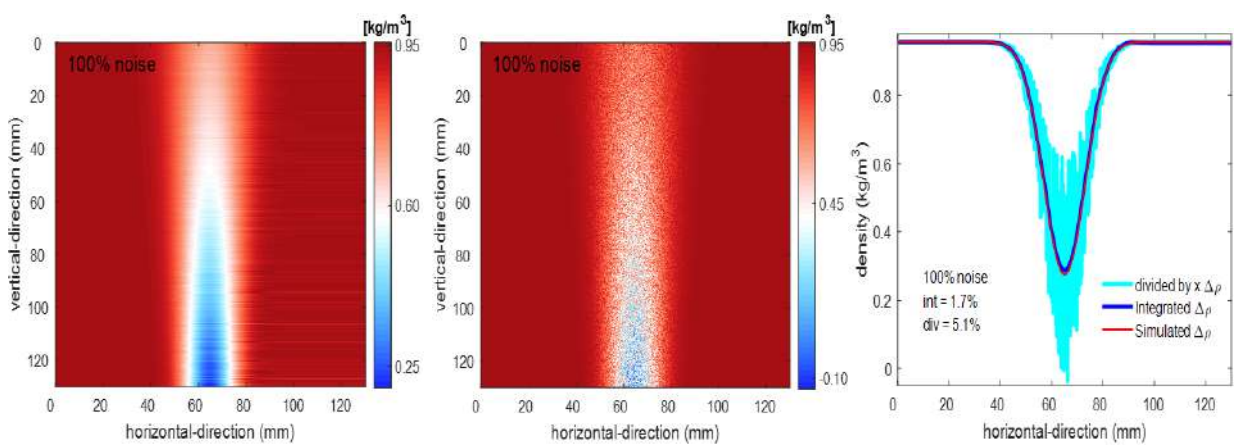

(a) Recovered ρ by integration (b) Recovered ρ by divided by x (c) Horizontal profile comparison

Figure 4.3.14: Recovered ρ; $a)$ by the integration technique, $b)$ by dividing by x , and $c)$ profile comparison.

$Figure$ 4.3.15(a) shows the recovered density ρ by the integration procedure after noise amounting to 150% were added. $Figure$ 4.3.15(b) depicts the recovered density ρ by the procedure of dividing by x . $Figure$ 4.3.15(c) demonstrates the comparison of the horizontal profiles. An error of 2.3% was recorded for the integration method and an error of 11.7% for dividing by x.

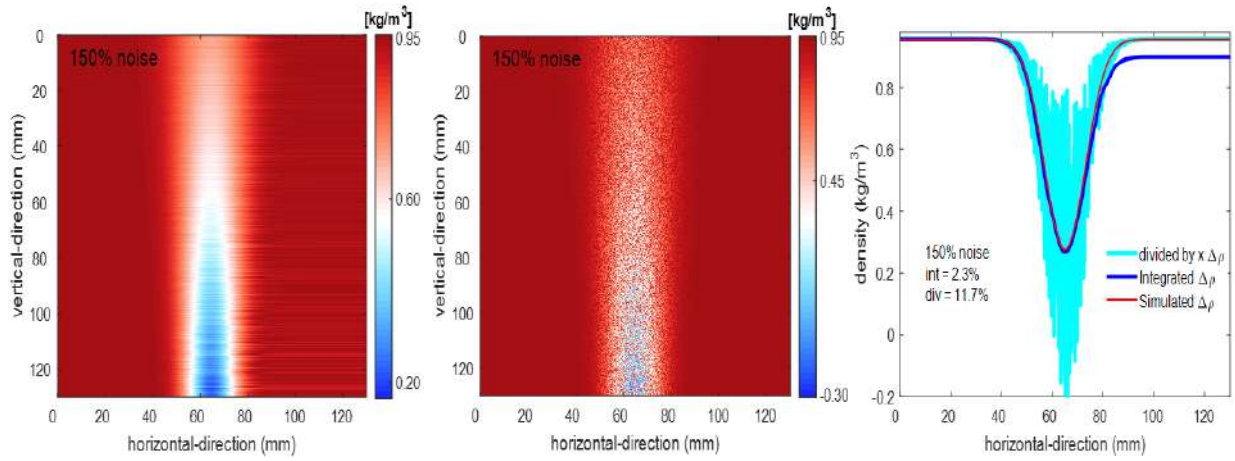

(a) Integrated (b) Divided by x (c) Horizontal profile comparison

Figure 4.3.15: Recovered ρ; $a)$ by integration, $b)$ by dividing by x , and $c)$ profile comparison.

The recovered parameters in the presence of noise compares well with the originally simulated parameters, except in the cases where the method of dividing by x is used, which produces large errors. The horizontal profile comparisons clearly shows that large errors are produced in the method of dividing by x, especially towards the center line of the parameters where values of x approaches zero.

4.4 Fringe Deflection Simulation

To simulate the Fringe Deflection, the reference image of the Refractive Index was first generated using $Eq.(2.4.28)$. The image is shown in $Figure$ 4.4.1(a). The equation $I_{patt} = 2 + cos(\frac{2\pi}{P}x)$ was used to generate the fringe patterns shown. P is the period, set to 200 lines per inch.

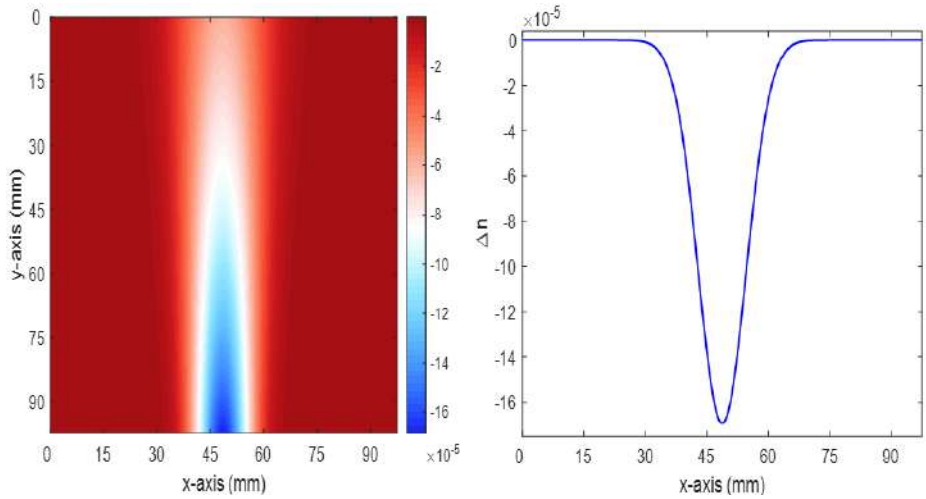

(a) Reference Δn (b) Δn horizontal profile

Figure 4.4.1: Change in Refractive Index ; a) Reference image, b) Horizontal profile

Vertical fringes were created using $Eq.(2.11.1)$, the resulting fringes are shown below. $Figure\ 4.4.2(a)$ is the reference image (un-displaced fringe patterns) and (b) is the displaced fringes.

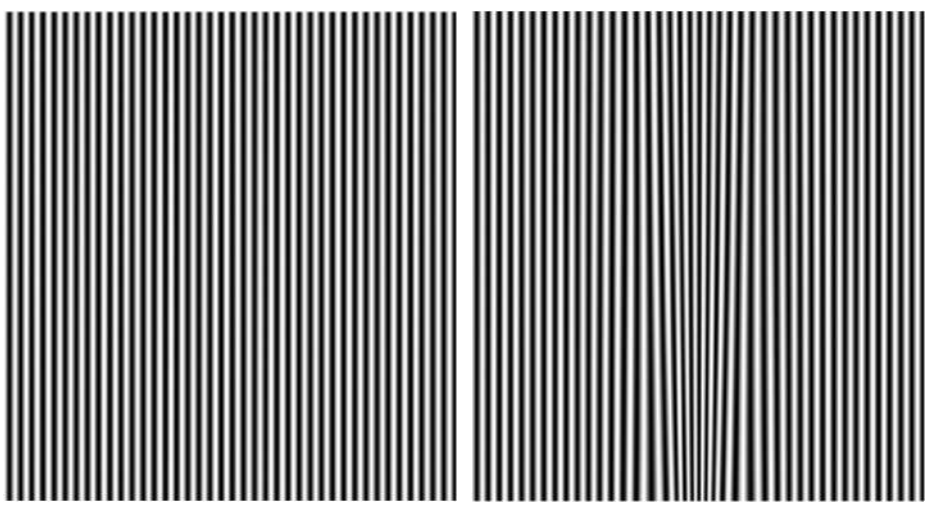

(a) Reference image (vertical fringes) (b) Displaced fringes

Figure 4.4.2: Fringe pattern ; a) Reference pattern,b) Deflected pattern.

The change in phase $\Delta\phi$ that was used to displace the fringe patterns is shown in $Figure\ 4.4.3\ (a)$, which is between $-1.5rad$ and $1.5rad$.

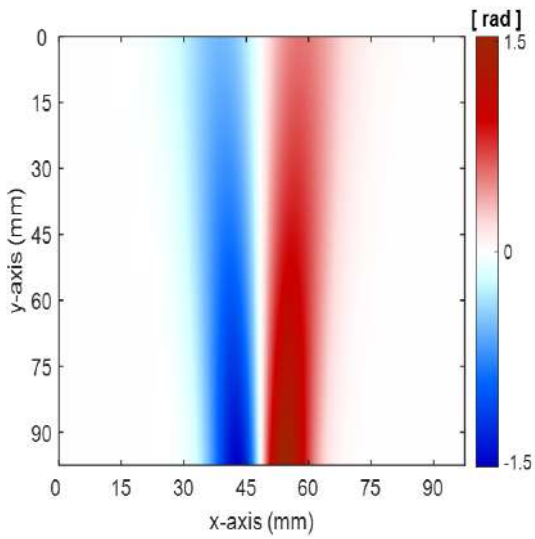

Figure 4.4.3: a) Change in phase ϕ ($\Delta\phi$)

The next figures show the Fourier transforms of the reference fringe pattern and the displaced fringes. $Figure$ 4.4.4a results from performing the Fourier transform to the reference image and the displaced fringe patterns respectively.

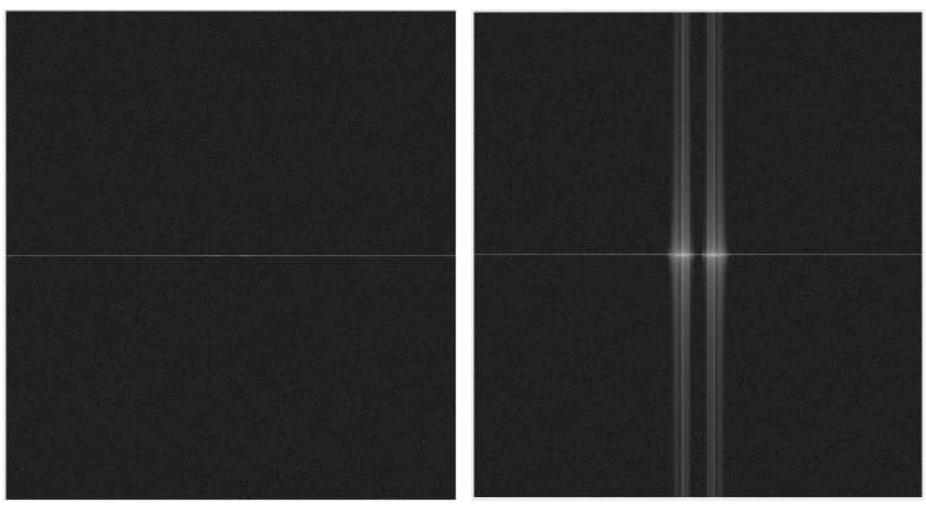

(a) Fourier transform of reference fringes (b) Fourier transform of deflected fringes

Figure 4.4.4: Fourier Transform; a) reference image and, b) deflected image

A filter (mask) was applied to both images to isolate the lopes. An inverse Fourier transform was then applied to the difference of the two Fourier transformed images to produce the wrapped phase image shown in $Figure$ 4.4.5 (a). An algorithm was then applied to unwrap the phase. $Figure$ 4.4.5(b) shows the unwrapped phase, with its horizontal profile shown in $Figure$ 4.4.5(c).

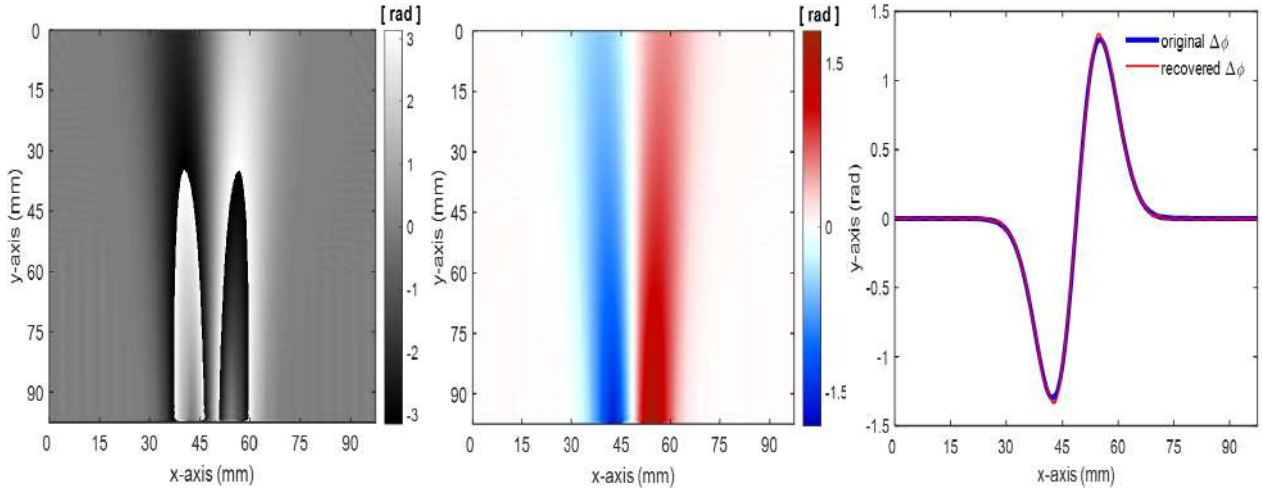

(a) Wrapped phase (b) Unwrapped phase (c) Horizontal profile

Figure 4.4.5: Recovered information; a) Unwrapped phase and, b) Wrapped phase, c) Unwrapped phase horizontal profile.

The recovered Δx shown in $Figure\,4.4.6(a)$ was computed from $Eq.(2.4.32)$. This recovered Δx resembles $\Delta\phi$ because it is $\Delta\phi$ multiplied by a constant $\frac{P}{2\pi}$.

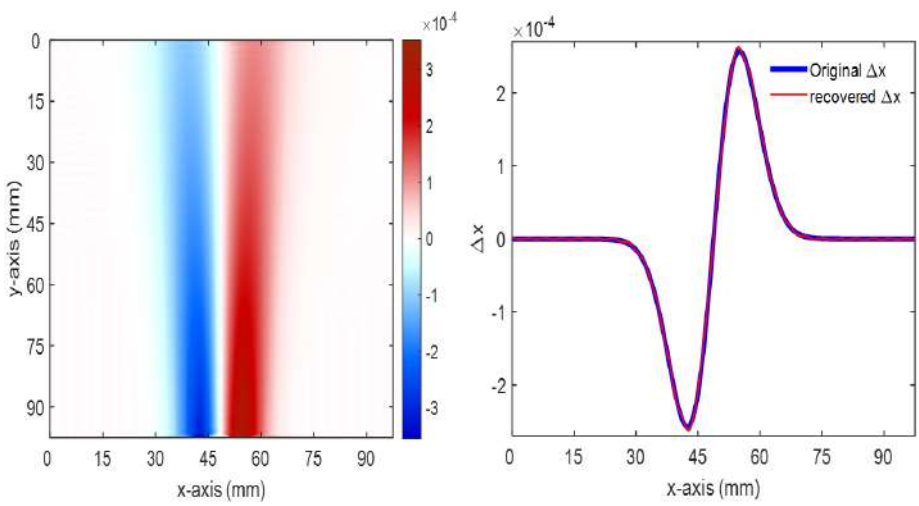

(a) recovered Δx (b) Recovered Δx horizontal profile

Figure 4.4.6: a) Recovered Δx and, b) recovered Δx horizontal profile

After recovering the unwrapped phase and the change in x (Δx), the next step is to reconstruct the refractive index variation Δn. The reconstruction process uses two methods (Method 1(**P1**) and Method 2(**P2**)) described in Section 2.4.1. The results of the reconstructed $\triangle x$, $\triangle n$, $\triangle T$ and $\triangle\rho$ are presented in Section 4.7 and the errors resulting from the application of the computational algorithms are also given.

4.4.1 Radius Computation

One of the most important parameters of the reconstructed $\triangle n$ is the radius. $Figure\,4.4.7$ shows the comparison of the of the radii. Shown in the figure is the original radius which is the simulated radius (in blue curve), and

the radius of reconstructed $\triangle n$ (in red curve). The recovered radius shows a lot of deviations from the original radius at the edges, however, it follows the original radius precisely in the center of the image. In general, the recovered radius is similar to the original. The computed radius ranges between $7.5mm$ and $12.8mm$. Compared with the original simulated radius, the calculated error is 0.2%.

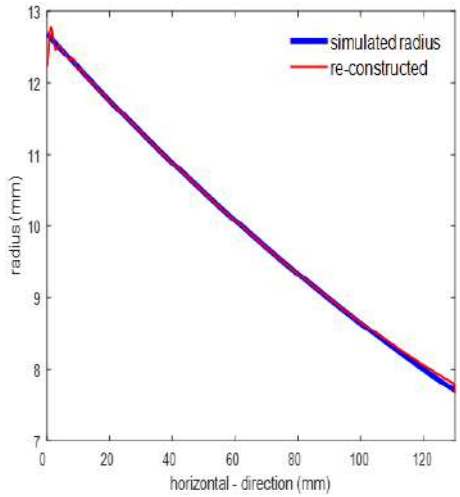

Figure 4.4.7: Radius comparison

4.5 FD Error Computation

This section assesses FD technique when recorded images contains added noise. The randomly generated noise is added to the respective reference and object images before the Fourier transform is applied. For the error analysis of FD technique, $Eq.(2.6.5)$ is the equation used to generate the random noise.
Parameters are recovered and compared with the original simulated parameters with no noise, in order to determine the robustness of the algorithm. $Figure\ 4.5.1$ shows fringes with 50% added noise.

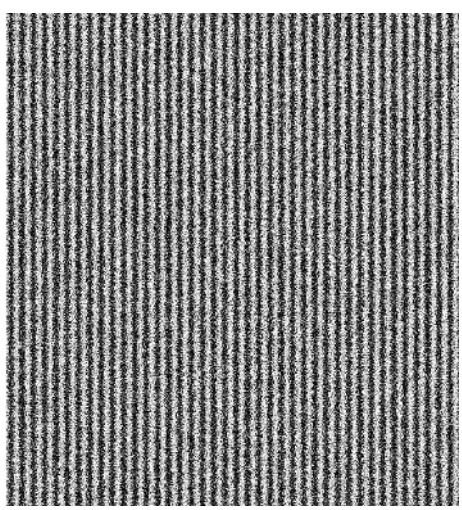

Figure 4.5.1: Fringes with 50% noise.

4.5.1 Change in Displacement Δx

For the Fringe Deflection technique, the recovered phase is the first recovered parameter of which the subsequent parameters are computed from. The change in x is calculated from the recovered phase, where the phase is multiplied by a constant $Eq.(2.4.32)$. It is for this reason that the change in x errors are evaluated.
50% noise was added in the fringes before recovering the parameter Δx_{REC}, $Figure$ 4.5.2(a) shows the recovered parameter, which was then compared to the original Δx_{SIM} (without noise), to a recorded discrepancy of 3.8% error. A horizontal profile comparison of Δx_{REC} and Δx_{SIM} the simulated change in x is shown in $Figure$ 4.5.2(b).

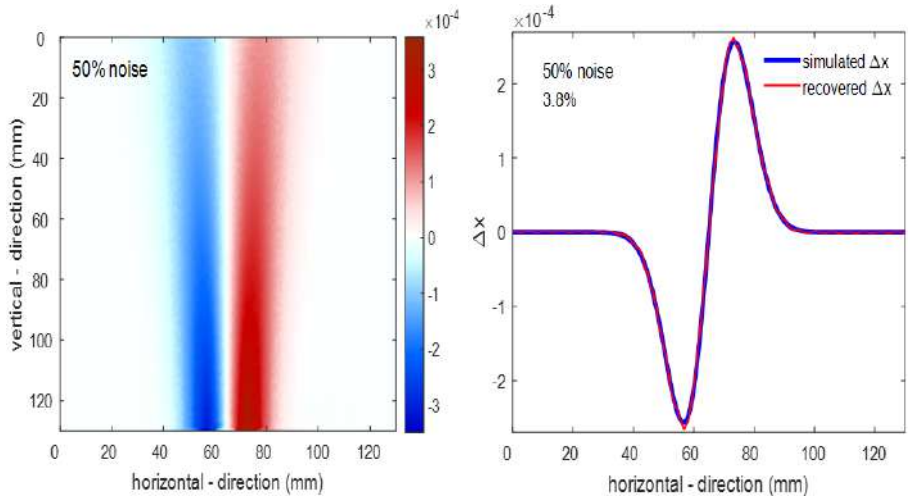

(a) Recovered Δx (50% noise). (b) Horizontal profile comparison (50% noise).

Figure 4.5.2: Change in displacement in the x-direction $a)$ recovered with 50% noise, and $b)$ horizontal profile

The noise was increased to 100%, $Figure$ 4.5.3(a) shows the recovered change in x, with the horizontal profile comparison between Δx_{REC} and Δx_{SIM} depicted in $Figure$ 4.5.3(b) for a recorded error of 7.9%.

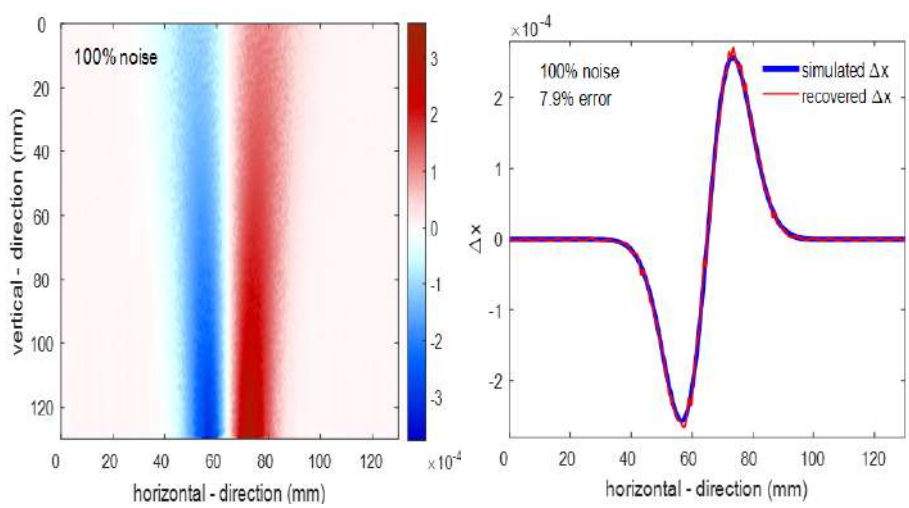

(a) Recovered Δx (b) Horizontal profile comparison (100% error).

Figure 4.5.3: Change in displacement $a)$ 100 noise added and $b)$ horizontal profile

An added noise of 150% results in a deviation of Δx_{REC} from Δx_{SIM} amounting to 12.2% error. The recovered Δx_{REC} is shown in $Figure$ 4.5.4(a), and $Figure$ 4.5.4(b) shows he horizontal profile comparison.

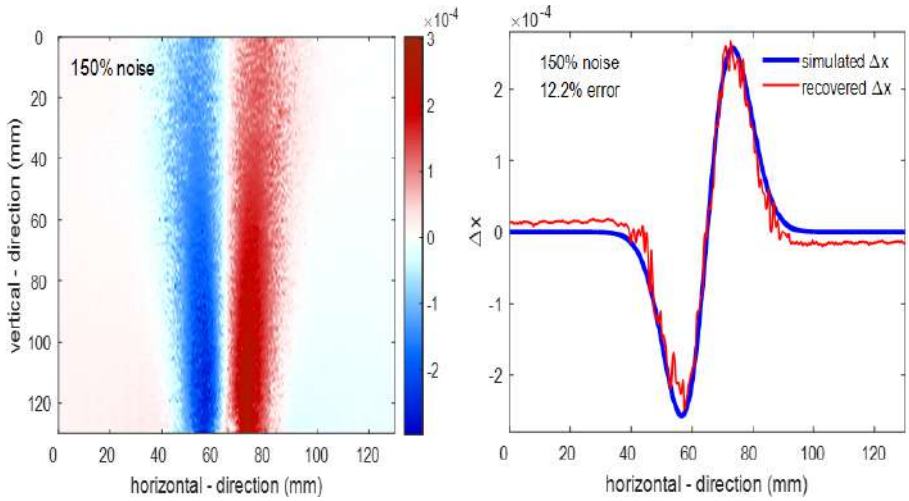

(a) Recovered Δx (b) Horizontal profile comparison (150% noise).

Figure 4.5.4: Change in displacement $a)$ 150% noise added and $b)$ horizontal profile

4.5.2 Radius

The radius is one of the most important parameters as it is needed when reconstructing other parameters. The radius of the recovered parameters is compared to the original simulated radius (without noise). $Figure$ 4.5.5 shows the recovered radius compared to the original radius after noise ranging from 50% to 150% were added. $Figure$ 4.5.5(a) show the recovered radius after the noise amounting to 50% were added. Adding noise of 100% results in a deviation of 4.6% from the originally simulated radius, while added noise of 150% results in 17.3% error.

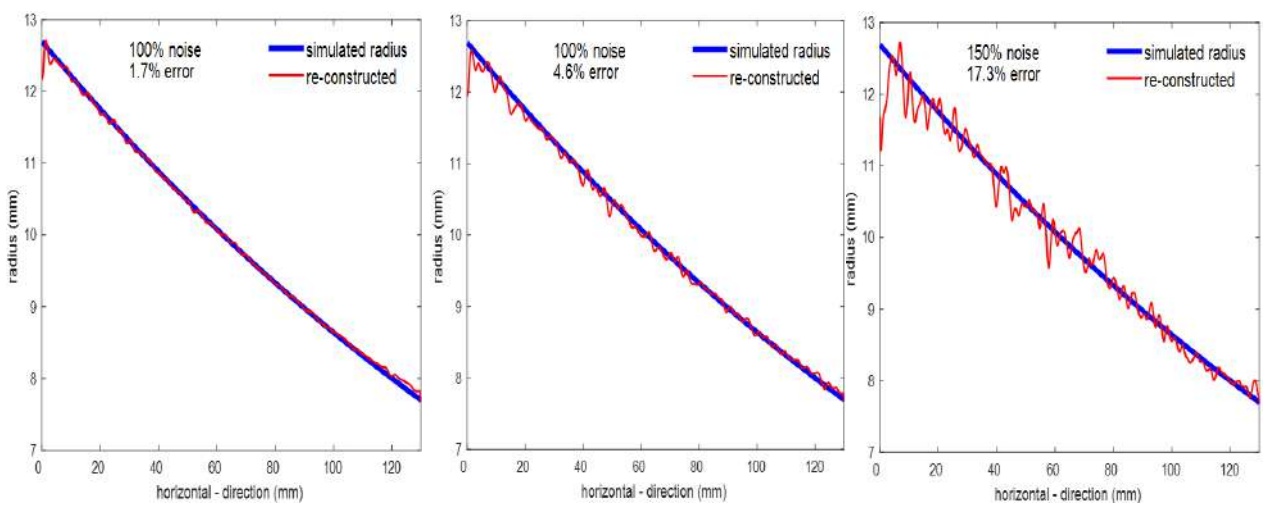

(a) Recovered radius with 50% added noise. (b) 100% added random noise . (c) 150% added random noise.

Figure 4.5.5: Recovered radius with added noise: $a)$ 50% noise $b)$ 100% noise $c)$ 150% noise.

4.5.3 Change in Refractive Index Δn

The refractive index is reconstructed by two methods, the first is by the integration procedure and the second is through dividing $\triangle x$ by x discussed in Section 2.4.1. $Figure$ 4.5.6 to $Figure$ 4.5.8 shows the images after noise ranging from 50% to 150% are added to $\triangle n$.

The recovered change in refractive index Δn after adding 50% noise is shown in $Figure$ 4.5.6. The recovery of $\triangle n$ by the integration procedure is shown in $Figure$ 4.5.6(a), Shown in $Figure$ 4.5.6(b) is the recovered change in refractive index Δn by dividing by x. The horizontal profile comparison is shown n $Figure$ 4.5.6(c), the computed error of 0.9% for the integration procedure and 3.7% for dividing by x.

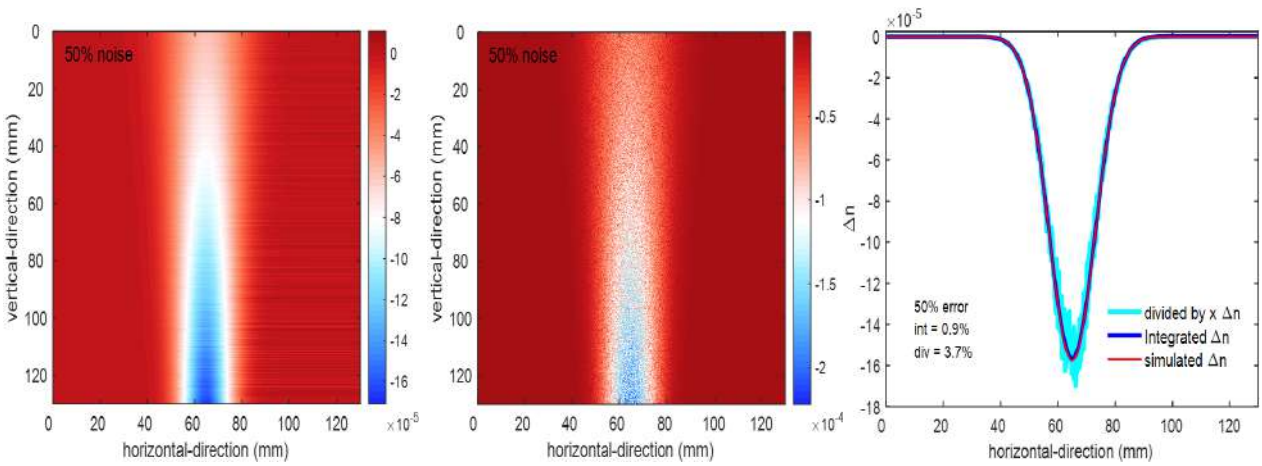

(a) Integration method (b) Division by x. (c) Horizontal profile comparison.

Figure 4.5.6: Recovered index of refraction with added 50% noise .

$Figure$ 4.5.7 shows the results when the noise is increased to 100%. $Figure$ 4.5.7(a) and (b) are the recovered change in refractive index Δn by the integration method and dividing by x procedure, respectively. $Figure$4.5.7(c) demonstrates the comparison of the horizontal profiles, with 1.2% and 7.5% errors, respectively.

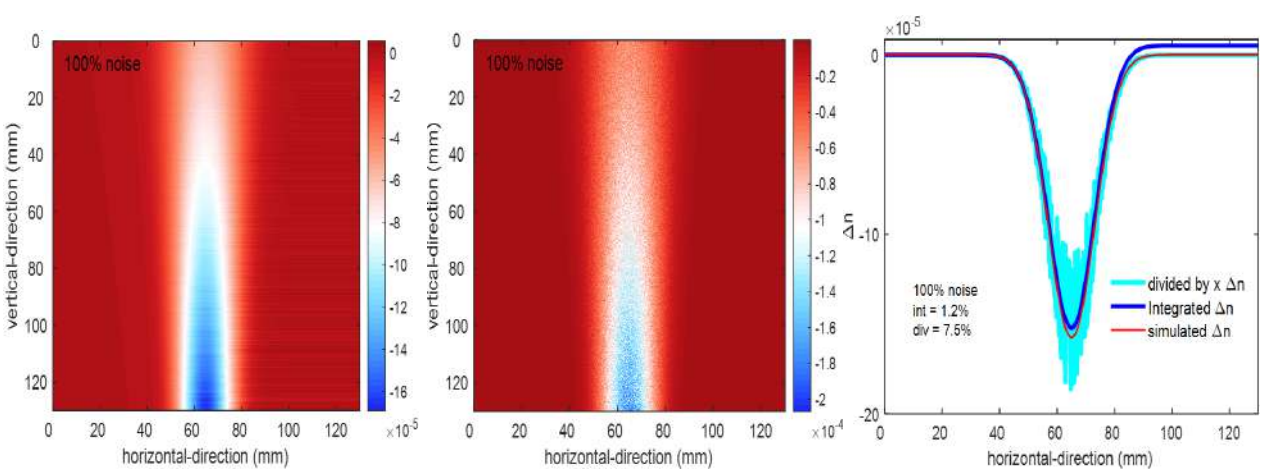

(a) Integration method. (b) Division by x. (c) Horizontal profile comparison.

Figure 4.5.7: Recovered index of refraction with added 100% noise.

$Figure$ 4.5.8(a) show the recovered change in refractive index Δn by the integration procedure after the errors amounting to 150% were added. $Figure$ 4.5.8(b) depicts the recovered change in refractive index Δn by the dividing by x procedure, and $Figure$ 4.5.8(c) demonstrates the comparison of the horizontal profiles. The computed error is 1.9% for the integration procedure while an error of 11.6% is shown for the method of dividing by x.

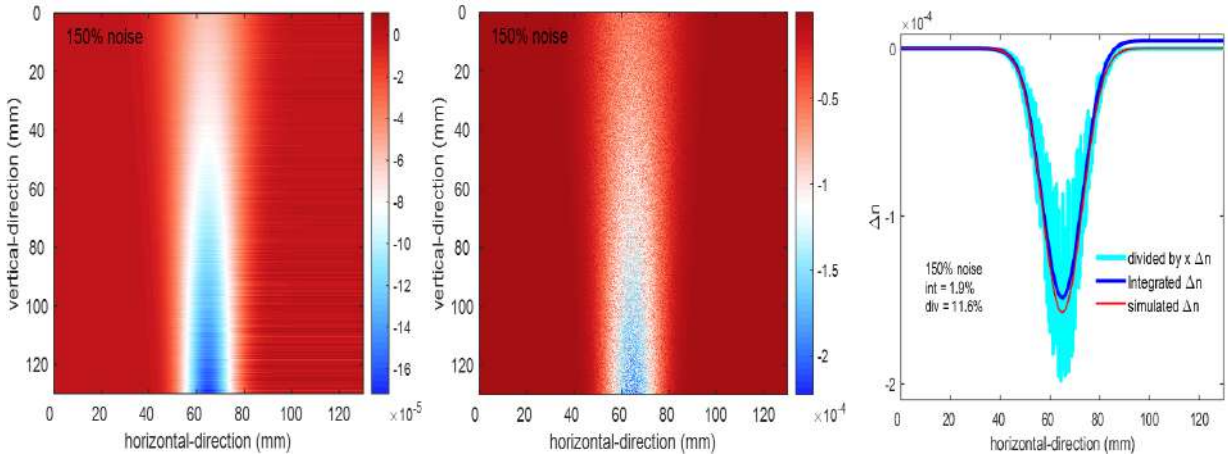

(a) Integration method. (b) Division by x. (c) Horizontal profile comparison.

Figure 4.5.8: Recovered index of refraction with added 150% noise.

Division by zero is not permitted, that is why dividing by x results in larger errors compared to integration method. This is one of the reasons that the integration method is widely used in research and practice and is preferred over the method of division by x, although it is complicated. The horizontal profiles also depicts the errors associated with method 2, which increases as the added noise increases.

4.5.4 Temperature T

$Figure$ 4.5.9 to $Figure$ 4.5.11 shows the recovered Temperatures T computed from the recovered $\triangle n$ by using the equation $Eq.(2.3.8)$. The recovered Temperatures were computed after 50%, 100% and 150% noise was added to T.

After adding noise of 50%, the recovered temperature is shown in $Figure$ 4.5.9(a) for the integration method, and $Figure$ 4.5.9(b) is the Temperature recovered by dividing by x method. $Figure$ 4.5.9(c) shows the horizontal profile of the recovered Temperature for comparison. The calculated error is 0.7% for the integration method and 7.8% for division by x.

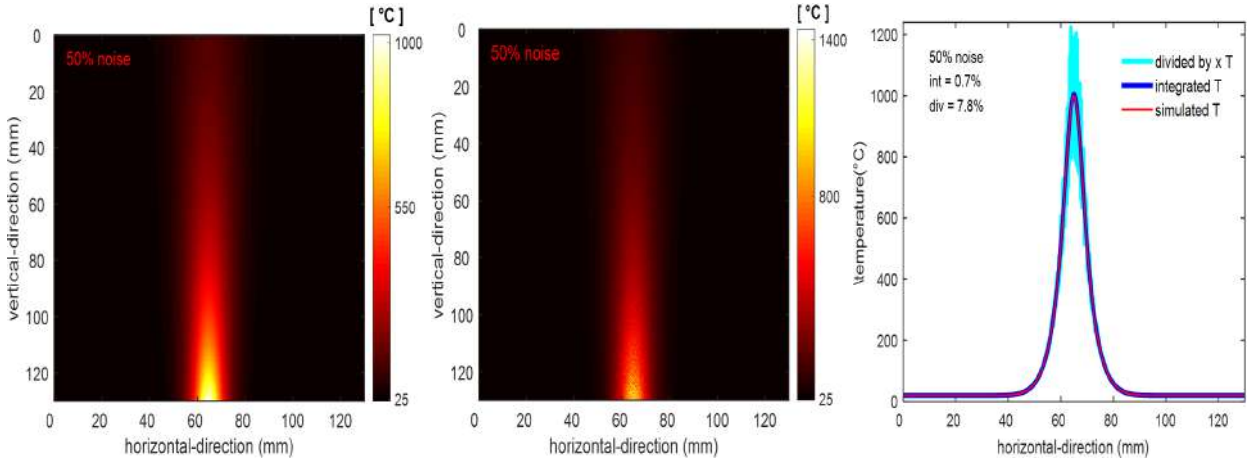

(a) Temperature by the method of integration.

(b) Temperature by the method of dividing by x.

(c) Horizontal profile comparison.

Figure 4.5.9: Recovered temperature with added 50% noise.

$Figure$ 4.5.10(a) show the recovered Temperature T by the integration procedure after the noise amounting to 100% were added. $Figure$ 4.5.10(b) depicts the recovered Temperature T by the method of dividing by x. $Figure$4.5.10(c) shows the comparison of the horizontal Temperature profile of the two methods. The calculated error is 1.5% for the integration method and 78.3% for division by x.

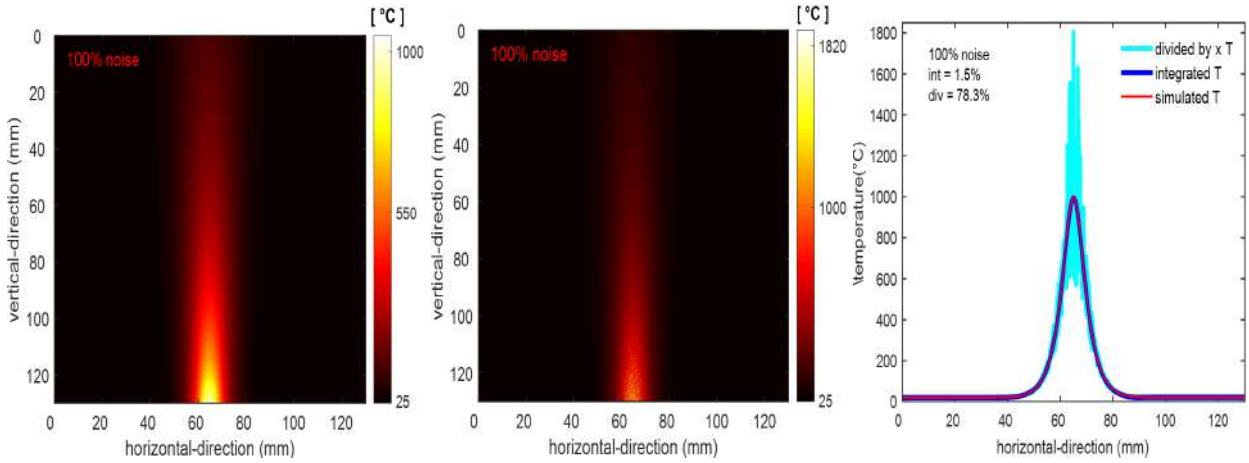

(a) Temperature by the method of integration.

(b) Temperature by the method of dividing by x.

(c) Horizontal profile comparison.

Figure 4.5.10: Recovered temperature with added 100% noise.

Increasing the added noise to 150% results in the recovered Temperature variation T as shown in $Figure$4.5.11(a) when the Temperature is recovered by the integration procedure. In $Figure$4.5.11(b), T is recovered by the method of dividing by x. While $Figure$ 4.5.11(c) demonstrates the comparison of the horizontal profiles. The calculated error is 3.0% for the integration method and 211.8% for division by x.

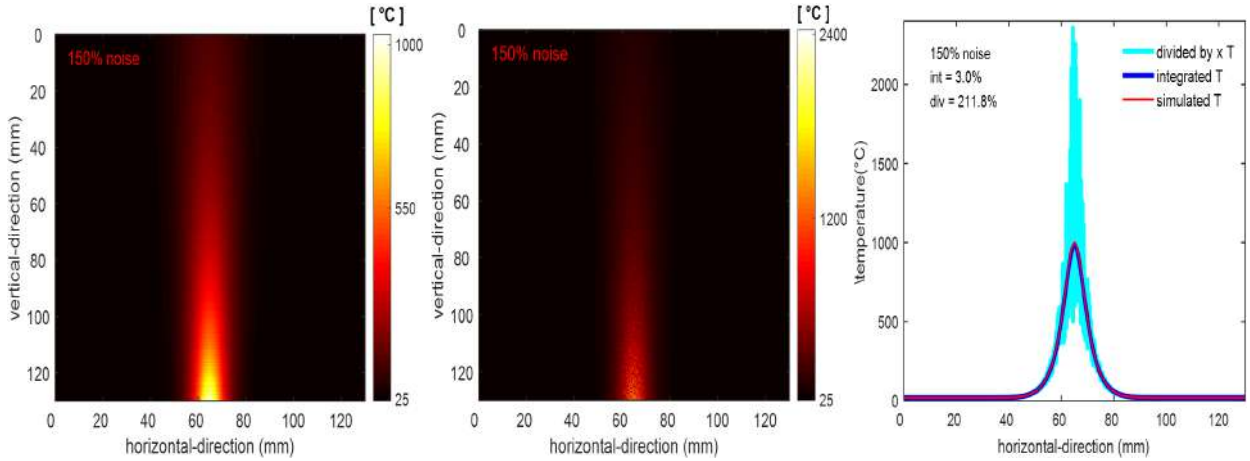

(a) Temperature by the method of integration.

(b) Temperature by the method of dividing by x.

(c) Horizontal profile comparison.

Figure 4.5.11: Recovered temperature with added 150% noise.

4.5.5 Change in density ρ

$Figure 4.5.12$ to $Figure 4.5.14$ show the recovered densities ρ calculated from the equation $\rho = \frac{n-1}{K}$. $Figure 4.5.12(a)$ shows the density ρ recovered by the integration process after 50% noise was added, in $Figure$ 4.5.12(b) the division by x method was used to recover ρ. $Figure 4.5.12(c)$ shows the horizontal profile of the recovered density for comparison. The calculated error is 0.6% for the integration method and 2.6% for division by x.

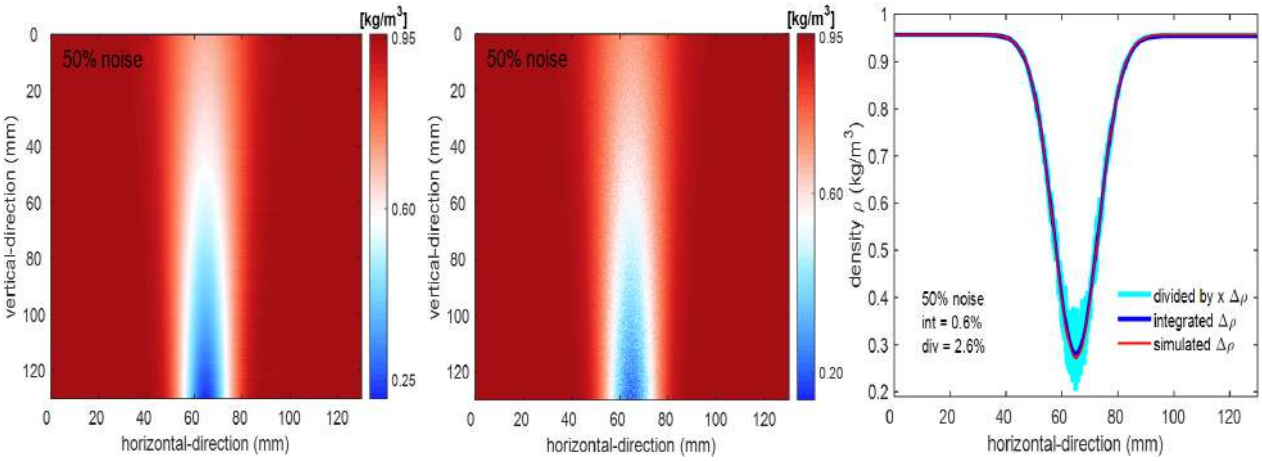

(a) Density by the method of integration.

(b) Density by the method of dividing by x.

(c) Density horizontal profile comparison.

Figure 4.5.12: Recovered density with added 50% noise.

Increasing the noise to 100% results in the recovered density as shown in $Figure$ 4.5.13. In $Figure$ 4.5.13(a) ρ is recovered by the integration method, in $Figure$ 4.5.13(b) ρ is recovered by the method of dividing by x. $Figure$ 4.5.13(c) compares the horizontal profiles. The resulting errors for the two methods are 1.3% and 3.9%, respectively.

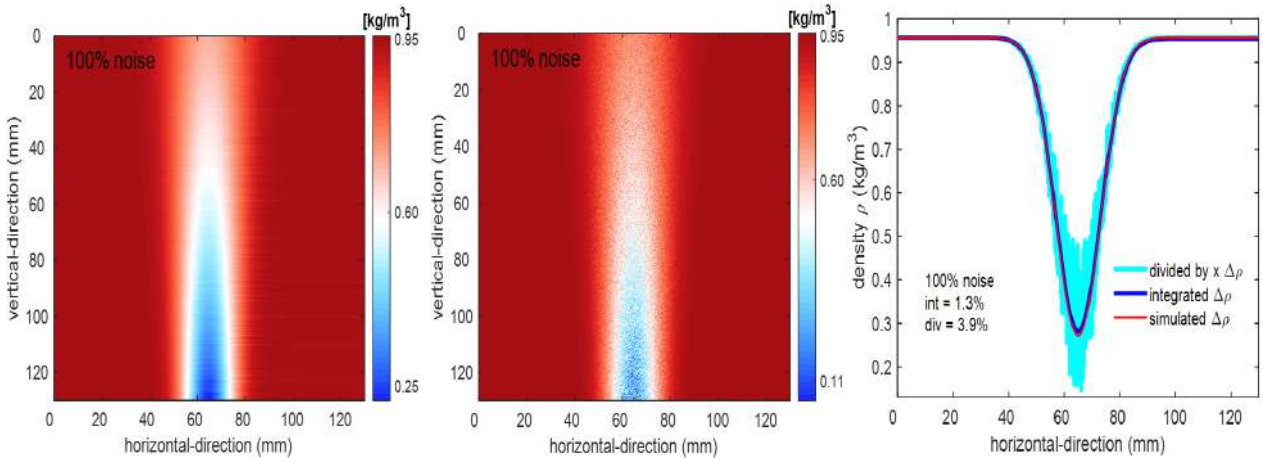

(a) Density by the method of integration. (b) Density by the method of dividing by x. (c) Density horizontal profile comparison.

Figure 4.5.13: Recovered density with added 100% noise.

150% added noise results in the recovered ρ as shown in $Figure$4.5.14 where $Figure$4.5.14(a) show the recovered density ρ by the integration procedure and $Figure$ 4.5.14(b) depicts the recovered density ρ by the dividing by x method. The recovered density profile comparison is shown in $Figure$ 4.5.14(c). The resulting errors for the two methods are 2.0% and 5.4%, respectively.

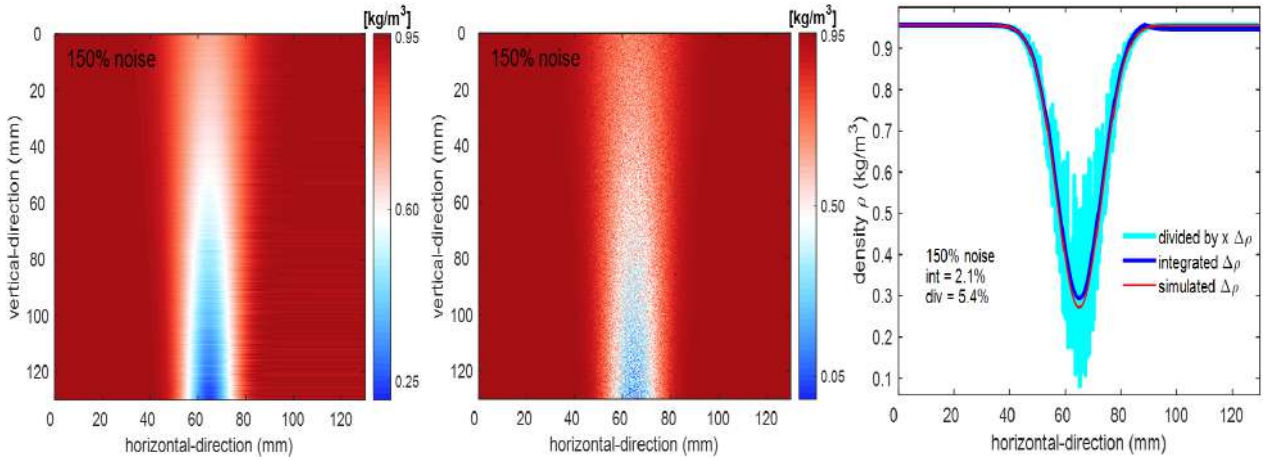

(a) Density by the method of integration. (b) Density by the method of dividing by x. (c) Density horizontal profile comparison.

Figure 4.5.14: Recovered density with added 150% noise.

The recovered densities compares well with the original simulated temperature, as shown by the horizontal profiles.

4.6 Conclusions

Based on the errors, the developed algorithms performed well. The parameters are recovered well even through there is added noise. It can be concluded without a doubt that the algorithms developed are quite robust, since they work well in an environment where there is noise. By comparing the errors between the BOS technique and

the Fringe Deflection, the Fringe Deflection outperforms the BOS method. It is therefore recommended to use the Fringe Deflection technique in the Helmholtz resonator experiment.

Although the method of recovering parameters by division by x is relatively easier to implement than the integration method, it leads to large errors because division by 0 is not allowed. This leads to large errors when x approaches 0. However, this approach has been studied and implemented as it could be used in some experimental procedures with a relatively low level of noise.

Bibliography

[1] M. Raffel, C. Willert, and J. Kompenhans, "Particle image velocimetry, a practical guide.", Springer - Verlag, Berlin (1998).

[2] M. Ota, F. Leopold, R. Noda, and K. Maeno. "Improvement in spatial resolution of background-oriented schlieren technique by introducing a telecentric optical system and its application to supersonic flow", In: Experiments in Fluids 56.3 (2015).

[3] G.E. Elsinga, B.W. Van Oudheusden, F. Scarano, and D. W. Watt, " Assessment and application of quantitative schlieren methods: Calibrated color schlieren and background oriented schlieren", Exp. Fluids 36 (2004).

[4] G. A. Meier, "Computerized background-oriented schlieren", Exp. Fluids 33, 181-187 (2002).

[5] A. Meier and T. Roesgen, "Improved background oriented schlieren imaging using laser illumination", Exp. Fluids 54:1549 (2013).

[6] N. Vinnichenko, A. Uvarov, and Y. Plaksina, "Accuracy of background oriented schlieren for different background patterns and means of refraction index reconstruction", 15th International Symposium on flow visualization, Minsk, Belarus (2012).

[7] H. J. Huang, A. and M. Waas, "Improved speckle method for measuring in-plane displacement and strain fields", Opt. Eng. 46(5), 051005 (2007).

[8] A. Blanco, B. Barrientos and C. Mares, "Performance comparison of background-oriented schlieren and fringe deflection in temperature measurement: part I. Numerical evaluation", Opt. Eng., 55(5), 064104 (2016).

[9] E. Goldhahn, and J. Seume, "The background oriented schlieren technique: Sensitivity, accuracy, resolution and application to a three-dimensional density field", Exp. Fluids 43:241-249 (2007).

[10] A.B. Gojani, B. Kamishi, and S. Obayashi, "Measurement sensitivity and resolution for background oriented schlieren during image recording.", The Visualization Society of Japan, June (2013).

Chapter 5

Experiments

Contents

For the sake of completeness, the performance of the BOS and the Fringe Deflection methods is evaluated experimentally in order to verify the results obtained in the simulation. In this Chapter, the conducted practical experiments; BOS and Fringe Deflection are presented. The PIV experiment is carried out to evaluate the developed correlation algorithm which is then used in the BOS experimental analysis.

5.1 PIV Experiment

PIV does not track each particle individually that is a similar but different technique known as Particle Tracking Velocimetry (PTV), but track the movement of particles in an interrogation window.

5.1.1 PIV Experimental Setup

The main components of a PIV system are the illuminating system, the camera and the imaging system. Two records of the location of the particle were taken. The first recording captures the start position of the particle and the second records its end position. A CCD camera was used, which enables post-processing of digital images by a computer.

For this experiment, polyamide tracer particles (PSP) with average diameters per particle of $50\mu m$ were used. The experimental setup used consists of a $JDSU\ He-Ne$ laser light source with a wavelength (λ) of $532.8nm$ and a power of $400mW$. The optical system for generating the light sheet consists of a cylindrical lens with an effective focal length of $-25mm$ and a spherical lens with an effective focal length of $50mm$. An aquarium with water and a heating system at its base was used to observe the flow of particles.

The video imaging system consists of a Lumenera camera (model $LM165M$) based on a gray-scale CCD sensor with a pixel size of $6.45\mu m$, a frame rate of $15fps$ and a resolution of 1392×1040 pixels; a lens with a focal length of $45mm$; and software that stores data as a byte array ($8\,bits$ per element) in 256 levels of gray. The experimental setup is shown in $Figure$ 5.1.1; Laser (A), Optical system (B), Fish tank (aquarium) with illuminated particles (C), Heating system (D), CCD camera (E), Computer for processing (F).

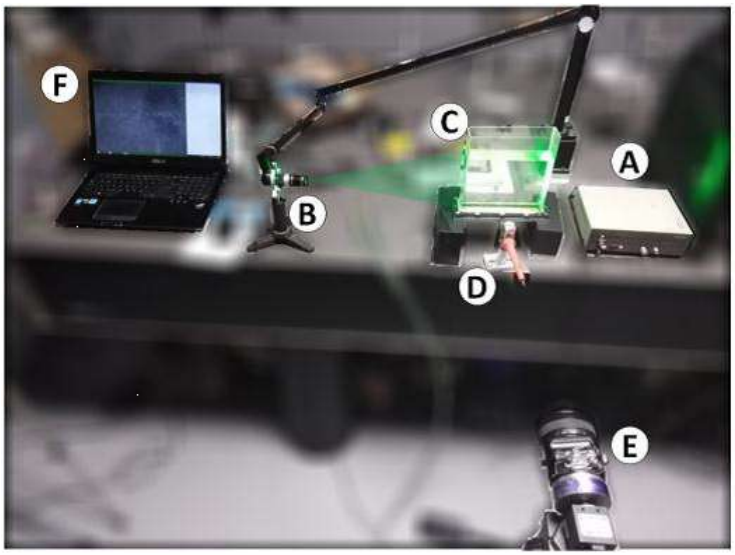

Figure 5.1.1: PIV experiment setup.

Regarding the geometry of the arrangement: the vertex distance from the last lens of the optical system to the

center of the camera's field of view was $50cm$, while the distance from the region illuminated by the light sheet to the aperture stop of the camera was $75.5cm$.

5.1.2 PIV Experimental Results

Considering that the field of view provided by the camera was in a ratio of $0.1005mm/px$ and that each image was taken $0.08sec$ apart; from a series of 15 images, however, only the first 3 images were the best and were selected for processing. The results are shown in $Figure$ 5.1.2:

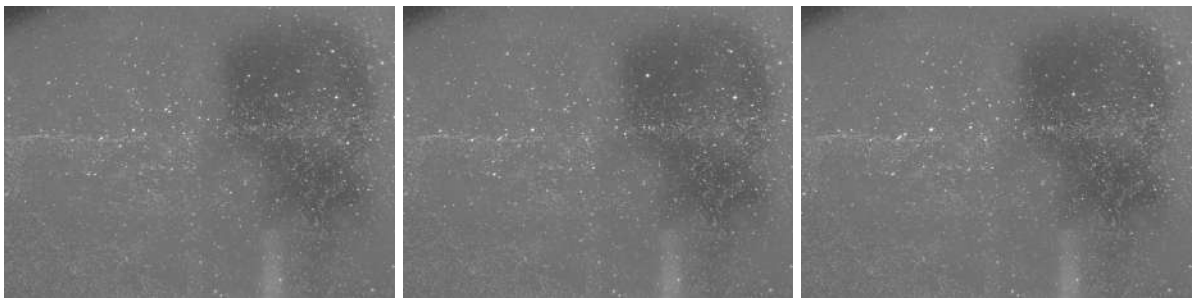

(a) First image (b) Second consecutive image (c) Third consecutive image

Figure 5.1.2: PIV experimental images;

This section presents the spatial and temporal velocity maps obtained from PIV. In contrast to the average velocity, which is usually expressed as a single value, the PIV results are displayed in the form of velocity fields or velocity maps. PIV provides information about the velocity development at a specific point in time (temporal velocity). An instantaneous spatial velocity profile is created by measuring the velocity of all points in the camera's field of view at a given point in time.

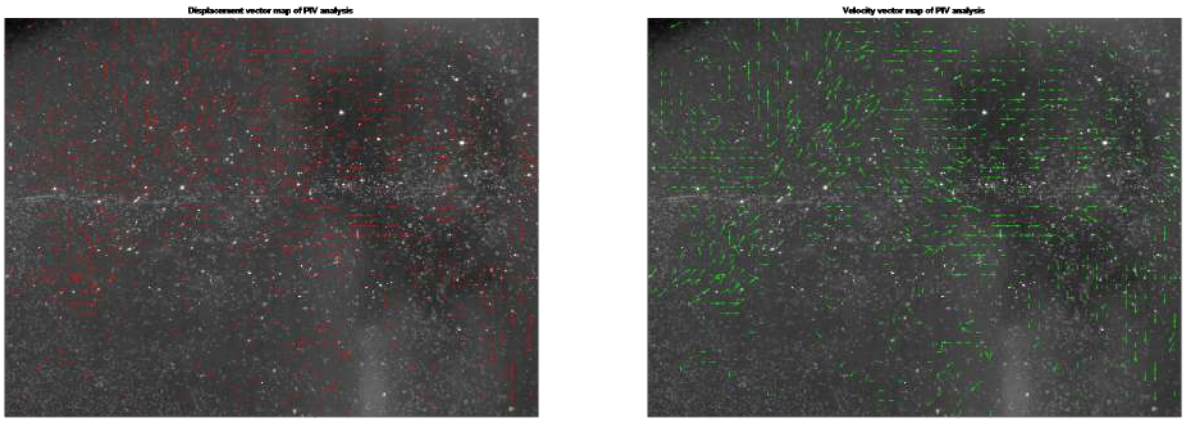

(a) Displacement vectors; image 1 & 2 (b) Velocity vectors; image 1 & 2

Figure 5.1.3: PIV analysis ; a) Displacement vectors between image 1 & 2 and b) Velocity vectors between image 1 & 2

$Figure$ 5.1.3(a) shows the calculated displacement vectors between the first image, which is used as a reference image in this case, and the second image. The time elapsed between taking the first image and the second image

was recorded as Δt. The recorded time was then used to calculate the velocity vectors shown in $Figure$ 5.1.4(b), by the use of the equation which states that the velocity is equal to the displacement over change in time $(v = d/\Delta t)$.

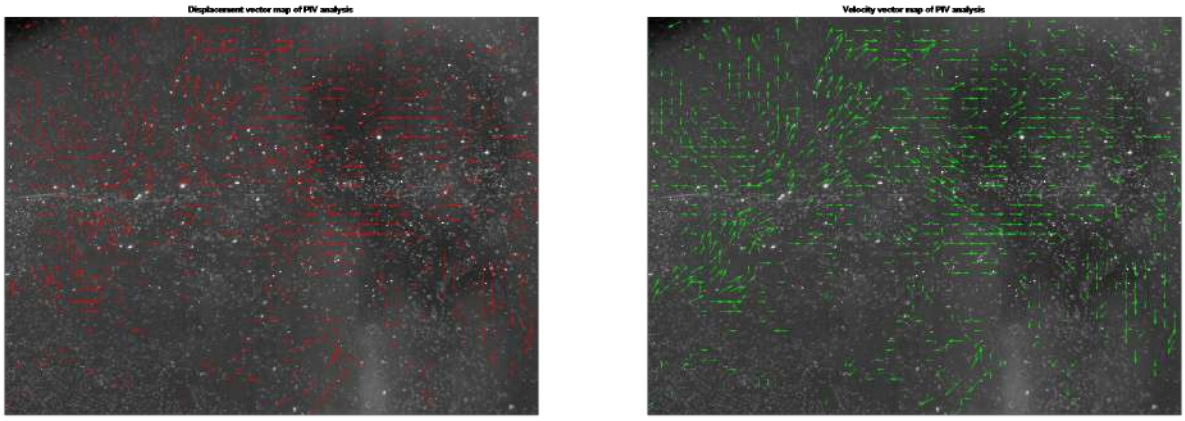

(a) Displacement vectors; image 2 & 3

(b) Velocity vectors; image 2 & 3

Figure 5.1.4: PIV analysis ; a) Displacement vectors between image 2 & 3 and b) Velocity vectors between image 2 & 3

The same procedure was followed in the subsequent images, 2 and 3, to plot the displacement vectors and the velocity vectors shown in $Figure$ 5.1.4 (a) and (b).
The aim of this experiment was to develop the PIV algorithm, track the particles and then record the displacement and velocity vector, which is then used in the BOS experiment. It is emphasized that the BOS technique uses the PIV algorithm to detect the movement of the points in the background.

5.2 BOS Experiment

In this section, the BOS experiment, consisting of a camera that is placed on a tripod and focused on the background, a computer to record and evaluate images, and a background with a random dot pattern. The experiment is performed to determine the temperature of a burning candle. The experimental setup, reference image formation, Refractive Index temperature and density extraction are discussed below. BOS technique is another application of cross-correlation procedures developed for PIV measurement technique.

5.2.1 BOS Experimental Setup

The only optical part required for the BOS experiment is an objective lens attached to a camera on the side of the receiver. The camera used focuses on a random dot pattern in the background, creating an image very similar to a particle image or a speckle pattern. It is for this reason the method is called background schlieren. The flow field is located on the axis of the view. Due to the refractive index gradients, the dot pattern is displaced in comparison to the reference recording, as observed from the recording side.
The recording configuration diagram for the BOS measurements is shown in $Figure$ 5.2.1, consisting of a CCD camera (sensor) with a variable aperture imaging lens, a sample object ($wax\ candle$) and a background (randomly dotted pattern). For the two experiments carried out, the sample object was positioned at a distance of $0.5m$ and

$0.75m$ from the source respectively. As an information acquisition system for recording the intensity images, the illuminated sample was observed by a closed monochrome Lumenera $10.7Mpix$ camera with model $LW11057M$ with a resolution of 4008×2672 effective pixels at a distance of $2.55m$ from the sample object; the screen pixel size was 141 micrometers, while the camera sensor size was 9 micrometers.
In the BOS experiment, the object to be examined is a candle, which has a temperature distribution similar to that in the numerical simulations.

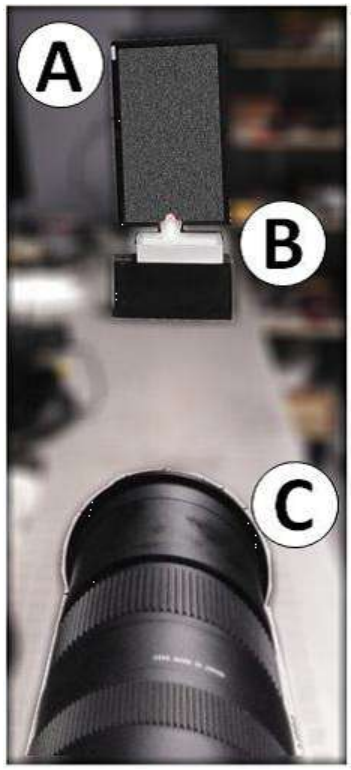

Figure 5.2.1: BOS measurement setup.

The dotted pattern is labeled as A, marked as B is the object (candle), and C is the camera lens.

5.2.2 Reference Image Construction

A background image is displayed on a computer screen. The image on the screen is a randomly located dot pattern generated by a computer program, placed at a distance from the object, which is usually less than the distance between the object and the camera, but in the same order of magnitude. For this experiment, the background reference image was generated digitally by speckle patterns in a computer using a Matlab programme.

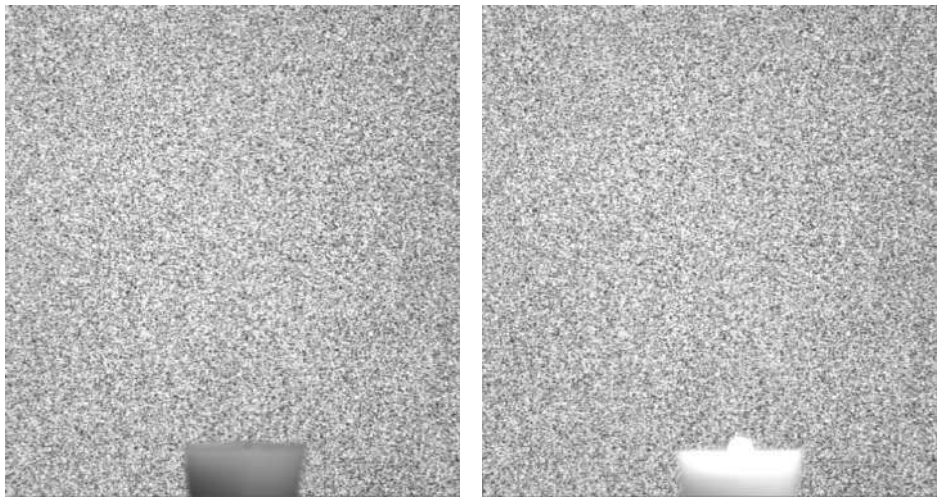

(a) Reference image (b) Image with object

Figure 5.2.2: BOS images ; $a)$ Reference image and $b)$ Image with object

The image of the background pattern captured without the flow or dynamic phenomenon is referred to as the "reference image", while the image obtained through the disturbance due to the flow is referred to as the "object image".

First, a reference image is generated by recording the background pattern as observed in still air before (or subsequent to) the experiment, as shown in $Figure$ 5.2.2(a). In the second step, additional exposure through the stream under study $(burning\ candle)$ in $Figure$ 5.2.2(b) results in a locally displaced image of the background pattern. The resulting images from the two exposures are then compared and evaluated using image correlation methods. The comparison is usually done by cross-correlation interrogation which is adopted from PIV technique, resulting in displacement field which is then used to reconstruct the refractive index field and subsequently the temperature and density variations.

Existing evaluation algorithms developed and optimized, for the PIV method discussed in Section 2.5 and experimentally implemented in Section 5.1, was then used to determine the displacement of the pattern at different locations throughout the image. The single beam deflection contains information about the spatial gradient of the integrated refractive index along the line of sight.

5.2.3 Parameter Extraction

A series of images were taken with the object (candle) placed between the camera and the background image. The object image was correlated with the reference image and the change in displacement Δx in $Figure$ 5.2.3$a)$. The length of each displacement vector indicates how much the particles are displaced. After Δx is calculated, all other parameters of interest can be computed, starting with the reconstruction of the change in the index of refraction Δn.

5.2.4 Change in Displacement ($\triangle x$)

The change in displacement ($\triangle x$) was recovered to be as shown in $Figure$ 5.2.3 below. The change in displacement is a map showing by how much the displaced particles are shifted in a given region.

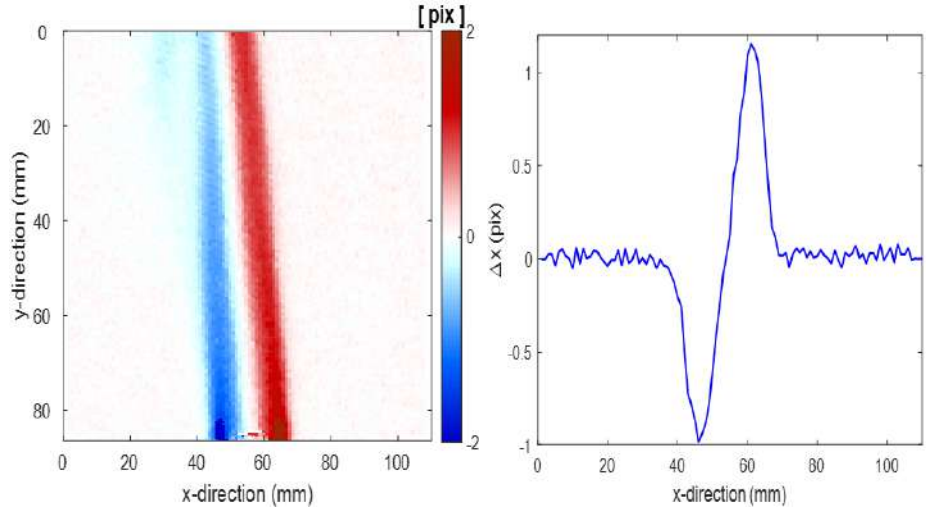

(a) Recovered $\triangle x$. (b) Horizontal profile through row 150.

Figure 5.2.3: Change in displacement; ($\triangle x$), a) showing a maximum displacement of $2\ pixels$ and b) horizontal profile through row 150.

The horizontal profile was taken through row 150. The recorded maximum change in displacement, as shown in the color bar, is $2\ pixels$.

5.2.5 Recovered Radius

The radius r_0 is one of the most important parameters since it is needed to compute other parameters. After obtaining $\triangle x$ as shown in $Figure$ 5.2.3, the calculation of r_0 from the curve fitting process follows. A curve fitting algorithm is applied to $\triangle x$ of the form:

$$Fit = A(x - x_0)exp\left[-\frac{(x - x_0)^2}{r_0^2}\right], \tag{5.2.1}$$

where the parameter r_0 is calculated for each row of $\triangle x$. The recovered radius in $Figure$ 5.2.4 ranged between $7mm$ and $13.4mm$ which compared well with the simulated radius in $Figure$ 4.4.7 ranging between $7.5mm$ and $12.8mm$.

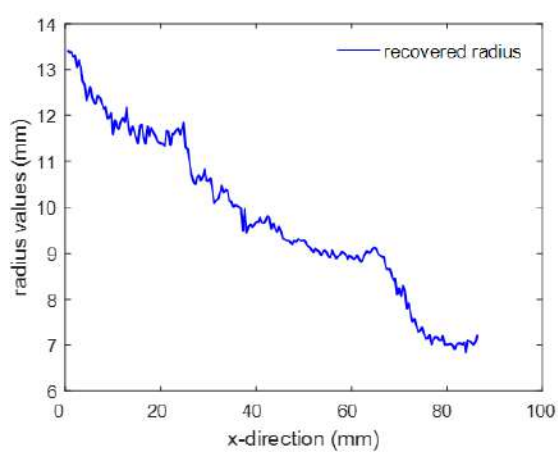

Figure 5.2.4: Computed radius by curve-fitting.

5.2.6 Change in Refractive Index

The re-constructed change in Refractive index is shown in $Figure$ 5.2.5 below. In order to obtain the map of the change in the refractive index, the change in displacement is integrated. The horizontal profile shown in $Figure$ $(5.2.5(b)$ was computed through row 150. The maximum change in Refractive Index is -16.0×10^{-5}.

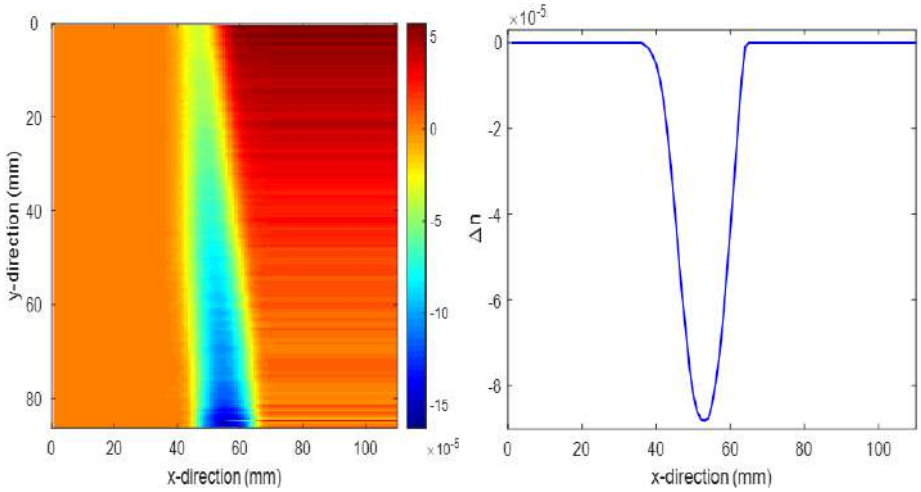

(a) Experimentally recovered $\triangle n$. (b) Horizontal profile through row 150.

Figure 5.2.5: Re-constructed change in Refractive Index ($\triangle n$) and the horizontal profile.

5.2.7 Temperature

The re-constructed change in Temperature is shown in $Figure$ 5.2.6 below, computed from the Refractive index Δn by the equation $T = T_0 \frac{n_0 - 1}{n - 1}$. The horizontal profile shown in $Figure$ $5.2.6(b)$ was taken through row 210. The recorded maximum change in temperature $T_{max} = 1050°C$ while the minimum temperature is at room temperature $T_{min} = 25°C$.

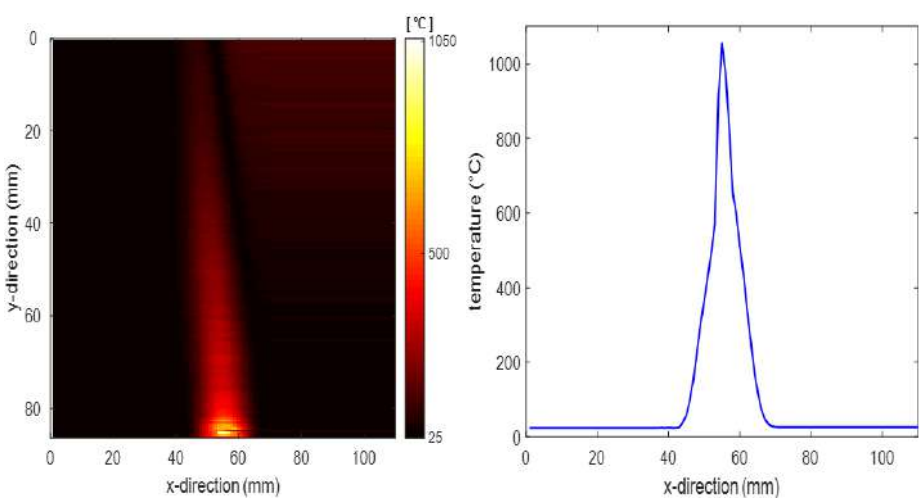

(a) Temperature. (b) Horizontal profile through row 210.

Figure 5.2.6: Re-constructed change in Temperature ($\triangle T$) and the horizontal profile.

5.2.8 Density

The re-constructed change in Density is shown in $Figure$ 5.2.7 below, computed from the Refractive index Δn by the equation $\rho = \frac{n-1}{K}$. The horizontal profile shown in $Figure$ 5.2.7(b) was taken through row 214. The recorded maximum change in density is $\rho_{max} = 0.96\frac{kg}{m^3}$ and the minimum is $\rho_{min} = 0.28\frac{kg}{m^3}$.

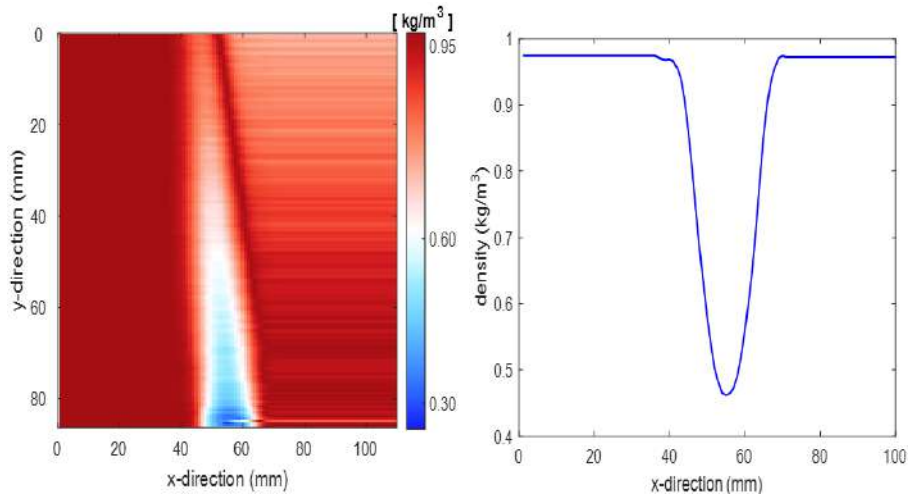

(a) Recovered density. (b) Horizontal profile through row 196.

Figure 5.2.7: Re-constructed change in Density ($\triangle\rho$) and the horizontal profile throuth row 196.

5.3 Fringe Deflection Experiment

$Figure$ 2.11.1 shows the schematic representation of the Fringe Deflection experimental setup. Shown in the representation is a background with a grid pattern with a period of $p = 0.05cm$ in both axes, a commercial "high quality" candle, a CCD camera Lumenera $LM11057M$ with a resolution of 4008×2672 pixels in combination with a lens and a computer to receive and save the images. $D = 33cm$ is the distance from the candle to the background, $\triangle x$ is the displacement created on the fringes when the phase modifying element is introduced, in this case the flame with a diameter of $L = 1.47cm$, and ε_x shows the deflection angle that each ray experiences. Finally, $d = 265cm$ is the distance between the flame and the CCD camera. It is important to keep a small numerical aperture because this technique requires the sample and background to be focused at the same time.

5.3.1 Experimental Procedure

An image of the multi-grid background, without an object, was taken, the image can be seen in $Figure$ 5.3.1(a). A second image, with an object, was taken. The image is illustrated in $Figure$ 5.3.1(b).
A multi-grid cross-correlation algorithm with a final interrogation size of 32×32 pixels was used to determine the displacement.

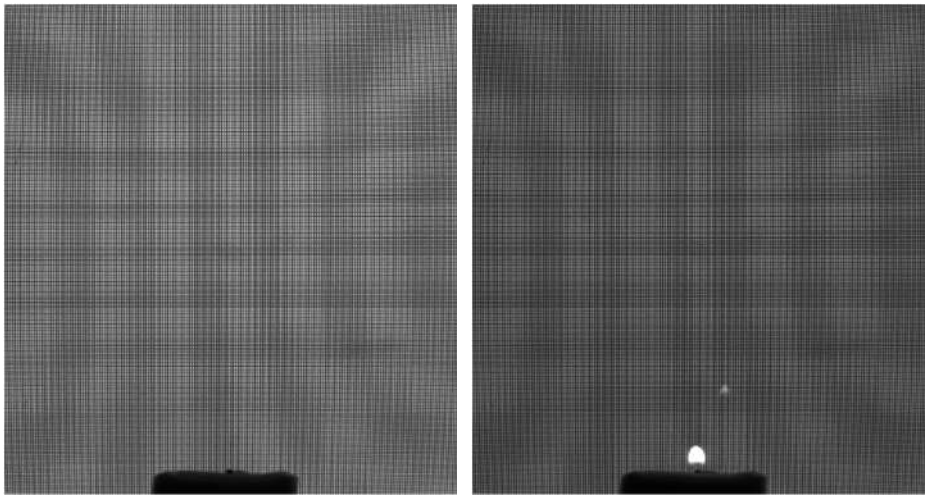

(a) multi-grid reference image (b) Deflected fringes

Figure 5.3.1: Multi-grid patterns ; a) Reference patterns, b) Deflected patterns

A Fourier transformation was carried out on the reference image and the object image, the results are presented in *Figure* 5.3.2.

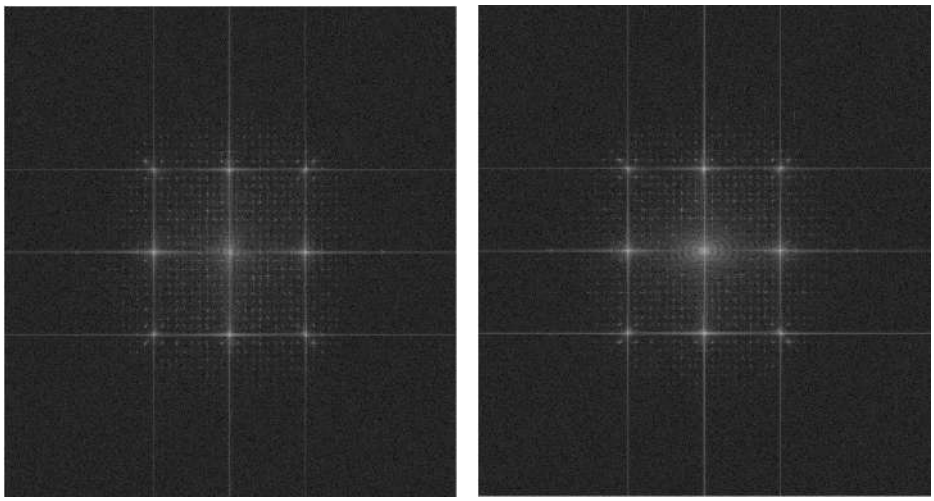

(a) Fourier transform of the reference pattern. (b) Fourier transform of the deflected pattern.

Figure 5.3.2: Fourier transform of ; a) Reference image, b) Deflected patterns

A filter (mask) was applied to the Fourier transform results of both images to isolate the lopes.

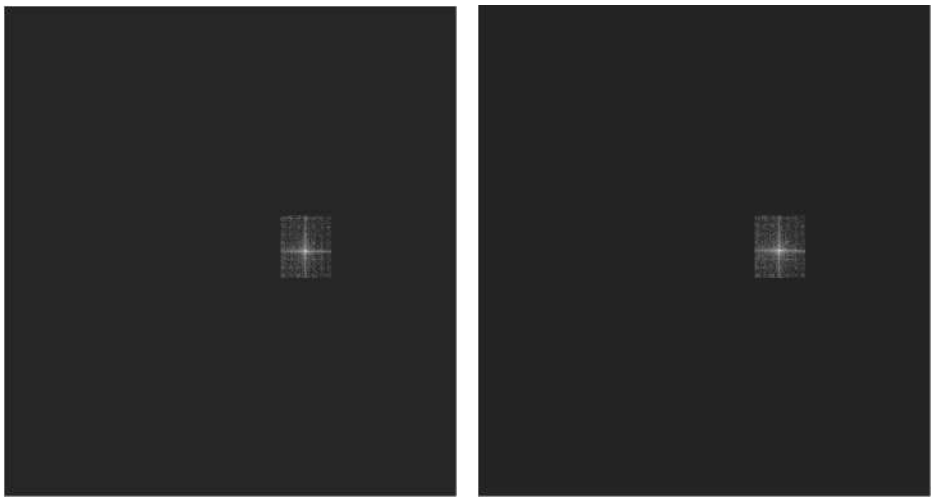

(a) Masked Fourier transform of reference pattern.

(b) Masked Fourier transform of deflected pattern.

Figure 5.3.3: Masked Fourie transform ; a) Reference image, b) Deflected patterns

An inverse Fourier transform was then applied to the difference of the two Fourier transformed images to produce the wrapped phase image shown in $Figure\,5.3.4(a)$ which ranges between $-3rad$ and $3rad$. An algorithm was then applied to unwrap the phase.

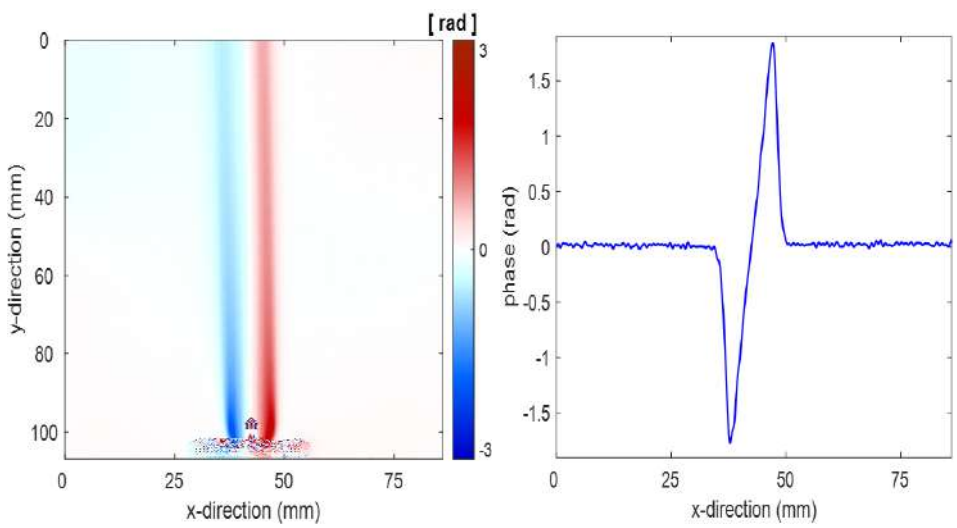

(a) Computed phase.

(b) Horizontal profile of the recovered phase.

Figure 5.3.4: a) re-constructed phase and b) computed radius by curve-fitting.

The equation to calculate $\triangle n$ in Table **2.1** requires the values of r_0, which after recovering the phase as shown in $Figure\,5.3.4(a)$, was calculated by curve-fitting. A Gaussian curve of the form as in $Eq.(5.2.1)$ was fitted and the values of r_0 for each row were calculated to be between $13.8mm$ and $9.5mm$ as shown in $Figure\,5.3.5$.

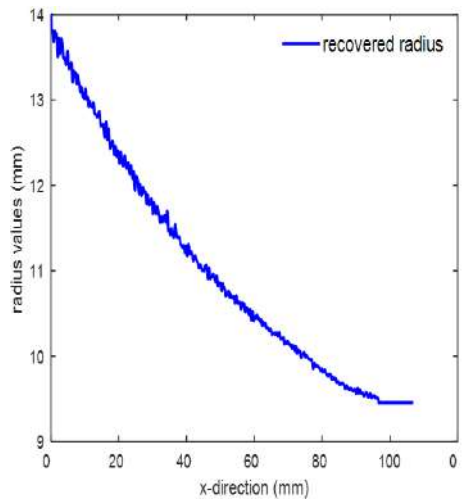

Figure 5.3.5: Recovered radius by curve-fitting.

To recovered the change in displacement Δx, the unwrapped phase in $Figure\ 5.3.4(b)$ was divided by 2π , calculated by the $Eq.(2.4.32)$. To recover the refractive index variation, the equation $\Delta n = \frac{1}{D} n_0 \frac{1}{\sqrt{n}} \frac{1}{r_0} \int (\Delta x) dx$ was used, which integrates the change in the x displacement to reconstruct Δn. $Figure\ 5.3.6(a)$ shows the recovered index of refraction, $Figure\ 5.3.6(b)$ shows a horizontal profile of the recovered index of refraction.

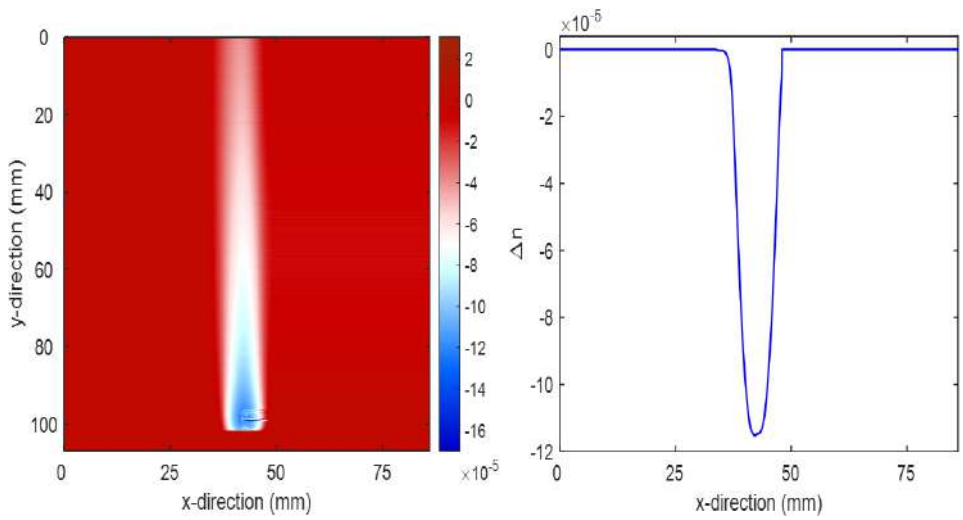

(a) Recovered change in Refractive Index (b) Horizontal profile.

Figure 5.3.6: Recovered; a) Change in Refractive Index, b) Temperature variation

$Figure\ 5.3.7(a)$ shows the recovered temperature, while the recovered density is shown in $Figure\ 5.3.7(b)$.

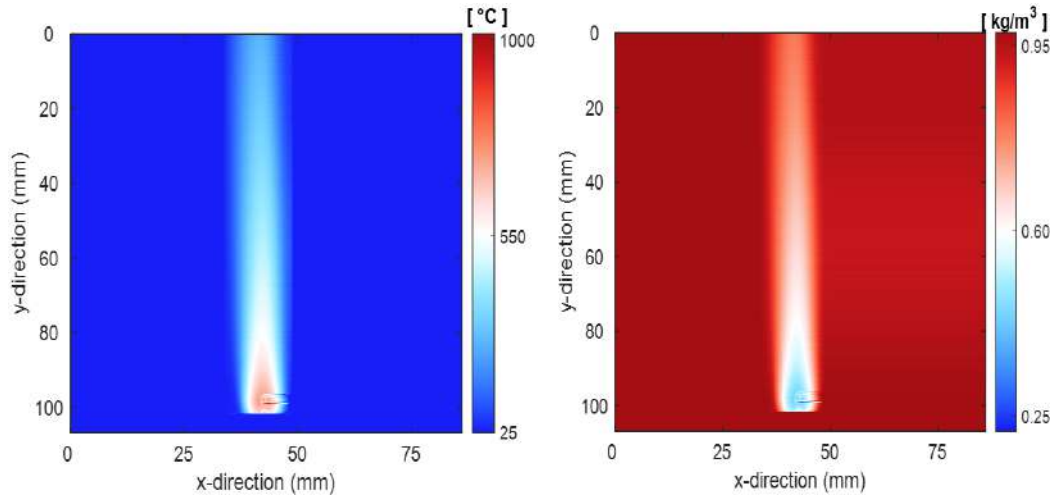

(a) Recovered temperature variation. (b) Recovered density variation.

Figure 5.3.7: Recovered parameters; a) temperature variation, b) density variation

The reconstructed index of fraction variation has a value of $\Delta n = -1.637 \times 10^{-4}$. The temperature variation has a minimum and maximum of $\Delta T_{min} = 25°C$ and $\Delta T_{max} = 1000°C$ respectively, while the minimum and maximum density variation is $\Delta\rho_{min} = 0.25kg/m^3$and $\Delta\rho_{max} = 0.95kg/m^3$ respectively.

5.4 Conclusions

In the experiment, the PIV technique was successfully applied to velocity field measurements. The basic principle of the technique is of the method was successfully implemented. Among the experimental techniques, the particle image velocimetry (PIV) is undoubtedly one of the most attractive modern methods of investigating fluid flow in a non-invasive way and allows to obtain instantaneous fluid flow fields by correlating with at least two exposures. The vast amount of data that can be obtained with the PIV technique requires that appropriate post-processing tools be used for an in-depth study of fluid dynamics phenomena.

In both method, the BOS and FD experiment, it was shown that refractive index gradients are important in the measurement of temperature field and density variations. The obtained results conforms well with the values stipulated in. The obtained temperature of the burning candle is $1050°C$ for the BOS method, while for the FD method the value is $1000°C$. The FD method performs relatively better than the BOS technique. The density values is $\rho_{max} = 0.96\frac{kg}{m^3}$ and $\rho_{min} = 0.28\frac{kg}{m^3}$for the Background Oriented Schlieren method and $\rho_{max} = 0.95\frac{kg}{m^3}$ and $\rho_{min} = 0.25\frac{kg}{m^3}$ for the Fringe Deflection technique were obtained, respectively. The computed refractive index are as follows: -1.64×10^{-4} for FD and -16.00×10^{-5} or the BOS technique.

Bibliography

[1] M. Raffel, C. Willert, and J. Kompenhans, "Particle image velocimetry, a practical guide.", Springer - Verlag, Berlin (1998).

[2] G. S. Settles, "Important developments in schlieren and shadowgraph visualization during the last decade," in Internatioanl Symposium on Flow Visualization, Springer Verlag (2004).

[3] A. Blanco, B. Barrientos and C. Mares, "Performance comparison of background-oriented schlieren and fringe deflection in temperature measurement, part 2: experimental evaluation,"Opt. Eng., 55(6) (2016).

[4] B. Barrientos, M. Cerca, J. Garcia-Marquez and C. Hernandez-Bernal, "Three-dimensional displacement fields measured in a deforming granular-media surface by combined fringe projection and speckle photography", J. Opt. A: Pure Appl. Opt., 10, 104027, 10 (2008).

[5] M. Stanislas and J. C. Monnier, "Practical aspects of image recording in particle image velocimetry", Meas. Sci. Technol. 8, 1417-1426 (1997).

[6] N. A. Fomin, "Speckle photography for fluid mechanics measurements", Springer-Verlag, Berlin (1997).

Chapter 6

A Helmholtz Resonator

Contents

This chapter deals with the application of the Fringe Deflection measurements in a Helmholtz resonator. The focus is on the Helmholtz resonator with one output. The synthetic air jet consists of a sealed cavity with an acoustic speaker, which acts as a nozzle membrane on one end and the jet orifice opposite it. The orifice is the only mode to interact between the cavity and the surrounding environment. According to the current experiment, air is the working fluid. As a diaphragm, an electromagnetic actuator (acoustic speaker) with a diameter of $83mm$ and an input voltage $(Vrms)$ of $4V$ is used. The dynamic field flows of the outlet are examined.

6.1 Helmholtz Resonator

Resonators find most uses in acoustics to amplify or attenuate sound waves, namely in musical instruments to amplify certain frequencies to produce desired tone and in internal combustion engines to dampen high levels of noise caused by internal combustion engines (ICEs), and in cooling systems by a synthetic jet [3] . A synthetic jet is commonly formed when fluid is alternately drawn into a small cavity and expelled through the movement of a membrane bounding the cavity so that no net mass is added to the system.
Helmholtz resonator (HR) can be represented as two elementary components: the first is the closed cavity and the second is a short open neck cavity. The resonator, often referred to as a Helmholtz resonator, behaves similarly to a mass spring oscillator, with air in the neck representing the mass and air in the volume acting like a spring [15]. It is basically a bottle with a large cavity and a short neck, named after Hermann L.F. von Helmholtz, who pioneered the discovery of the principles of physics and mathematics involved. Bottles and stringed instruments are the best well-known examples of Helmholtz resonators. A simple schematic representation of a HR is depicted in $Figure$ 6.1.1. The cavity of the bottle has a length of l_1 and the cross-sectional area is A_1, while the neck has a length of l_2 and the cross-sectional area of the neck is A_2. With the air density denoted by ρ, the mass in the neck is given by $M_2 = A_2 \rho l_2$. If there is a pressure difference between the inside and outside of the neck ($e.g.$ when blowing over the tip of the neck), the force of the small air mass is proportional to the cross-sectional area in the neck and the pressure difference.

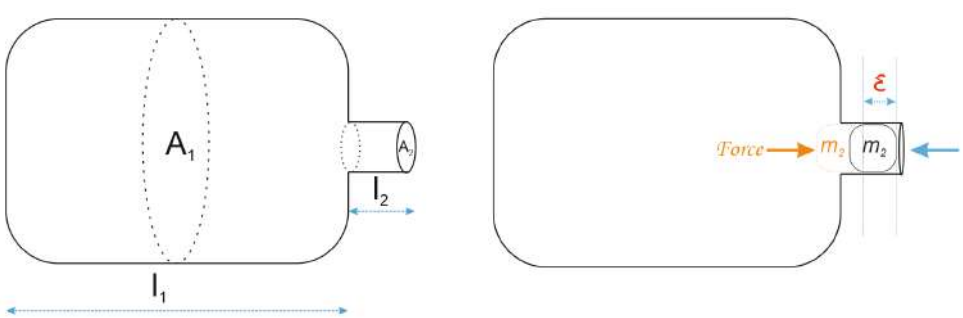

(a) Helmholtz resonator (b) schematic with depicted mass.

Figure 6.1.1: Schematic representation of the experimental setup of the Helmholtz resonator.

Suppose the small air mass in the neck is pushed in a little. The air in the cavity is compressed slightly. Since the compression takes place relatively quickly, the air in the cavity does not have time to exchange heat with others. Instead, the pressure in the cavity increases, pushing the small air mass in the neck outwards and transferring the energy back to the small air mass in the neck as work. This process is known as the adiabatic process, and the relationship between pressure and volume is:

$$PV^{\gamma} = const, \tag{6.1.1}$$

where $\gamma = \frac{C_p}{C_v}$ is the ratio of specific heats at constant pressure and constant volume. For air it is ≈ 1.4 [15]. When the small mass of air is pushed out of the neck, the air in the cavity expands and the pressure inside decreases, pulling the small mass of air inward. The small air mass in the neck oscillates (as shown in $Figure$ 6.1.1(b) following the simple harmonic motion.

The Helmholtz resonator (HR) is a perfect example of an aeroacoustic generator. A periodic external driving force (pressure perturbation) can cause high amplitude resonances if the applied frequency corresponds to the natural frequency of the system. The basic equation for the frequency of an ideal Helmholtz resonator is similar to oscillating systems, such as the classical spring-mass arrangement. Helmholtz resonators are often used as passive attenuators due to their simple geometry and stable acoustic absorption performance, used to damp acoustic waves and to decouple the acoustic and heat release rate fluctuations [1].

It follows from $Eq.$(6.1.1) that a change in volume dV_1 causes a pressure change dP, from $Eq.$(6.1.1), such that:

$$dPV^{\gamma} + P\gamma V_1^{\gamma-1} dV_1 = 0, \tag{6.1.2}$$

$$\frac{dP}{P} = -\gamma \frac{dV_1}{V_1}. \tag{6.1.3}$$

For a small disturbance of the air (inwards) of ξ, results in dV (as the mass moves inward, a distance of ξ , causes the volume inside the cylinder to decrease $(dV \simeq A_2\xi)$ such that $Eq.$(6.1.3) becomes :

$$dP = \left(\gamma \frac{A_2 P}{V_1}\right) \xi. \tag{6.1.4}$$

When the mass m_2 moves inward, the volume in the cylinder decreases, which leads to an increase in pressure in the cylinder. From the pressure equation $Pressure = \frac{force}{area}$ it follows that $Force = Pressure \times Area$. From Newton's second law of motion, which states that $force = mass \times acceleration$, we have $F = m\ddot{\xi}$, where $\ddot{\xi}$ is the second derivative of the displacement. Also take into account that mass in terms of volume and density can be written as $Volume = \frac{mass}{density}$. The restoring force on the mass plug (indicated as m_2 in $Figure$ 6.1.1(b) is

$$A_2 l_2 \rho \ddot{\xi} = -\left(\gamma \frac{A_2^2 P}{V_1}\right) \xi. \tag{6.1.5}$$

and the equation of motion of the air is

$$dP = \left(\gamma \frac{A_2 P}{V_1}\right) \xi. \tag{6.1.6}$$

or

$$\ddot{\xi} + \omega_0^2 \xi = 0, \tag{6.1.7}$$

where .

$$\omega_0 = \sqrt{\left(\gamma \frac{P}{\rho}\right)\left(\frac{A_2}{V_1 l_2}\right)} = c\sqrt{\frac{A_2}{(V_1 l_2)}}. \tag{6.1.8}$$

The frequency obtained in $Eq.$(6.1.8) is called the fundamental frequency, the lowest form of oscillation at which the sound pressure can be considered approximately uniform across the main volume of the bottle, where c is

the speed of sound in the cavity, also given as $c = \sqrt{\gamma \frac{P}{\rho}}$ [15], A_2 is the neck cross-sectional area, l_2 is the neck length and $V_1 = A_1 l_1$ is the cavity volume. In most cases, the Helmholtz resonators generate a known, stable, or unstable mass or momentum flow that primarily interacts with the domain under control consideration. $Figure$ 6.1.2 shows a schematic representation of the Helmholtz resonator with the parameters indicated.

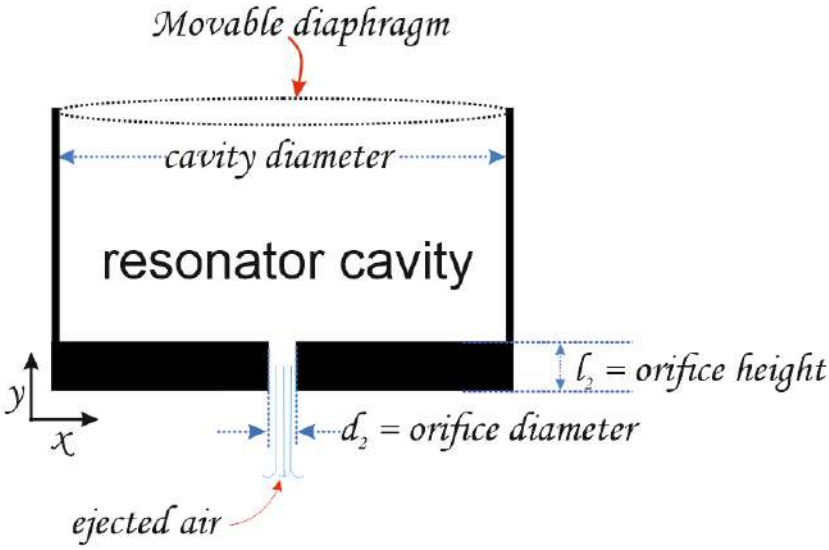

Figure 6.1.2: Schematic representation of a Helmholtz resonator.

Based on extensive research on synthetic jets in the past, the parameters that determine the synthetic jets flow field and subsequent performance can be broken down into operating parameters, geometric parameters, and fluid parameters, as shown in $Figure$ 6.1.3.

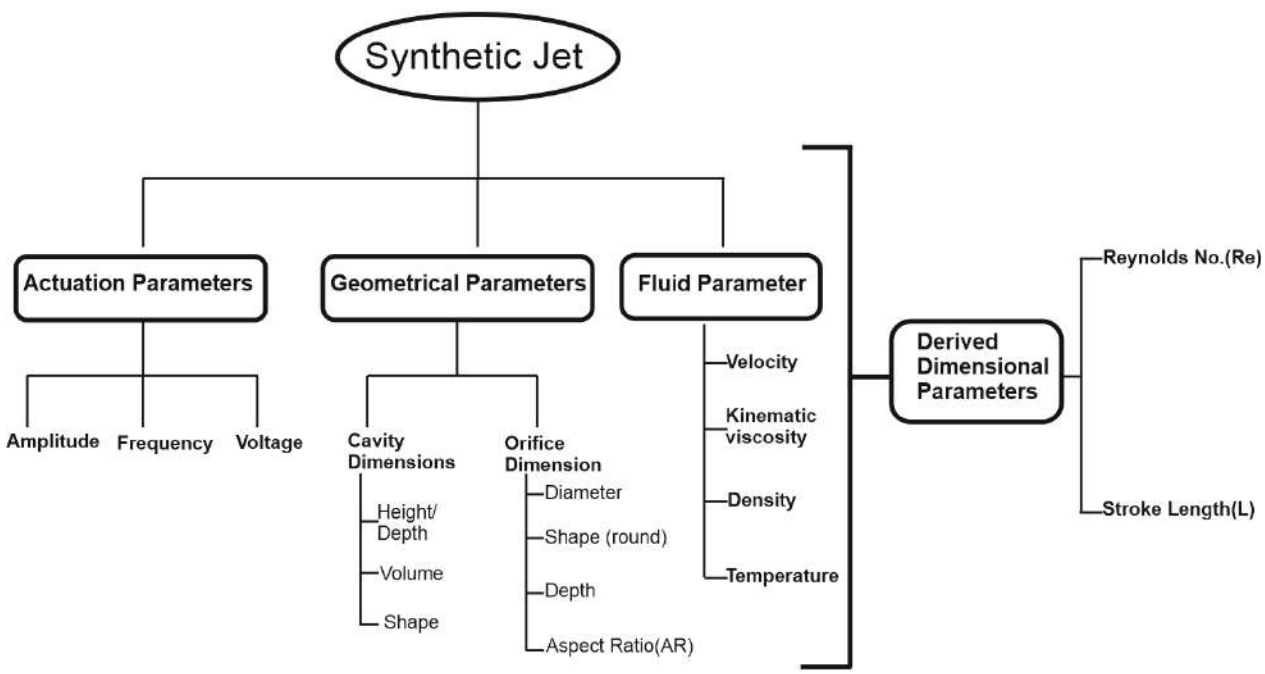

Figure 6.1.3: Parameters influencing synthetic jet flow-field.

The orifice plate thickness (orifice height), orifice and cavity radius are considered to be the most significant parameters.

6.2 Experimental Setup

6.2.1 Components of the Optical Arrangement

The components used for the experimental setup are as follows:

- Power supply unit to power the LED with $3V$ and $1A$.
- $3W$, $600 - 650nm$ red LED.
- Convex lens with a focal length of $24cm$ and a diameter of $50mm$.
- Ronchi grid with 150 lines per inch.
- Ronchi grid with 200 lines per inch.
- Hot table $250W$, $220V$ with a surface area of $16cm \times 10cm$.
- Speaker $5W$, 8 ohms diameter 4 inch.
- Cavity with a diameter of $83mm$ and a height of $30mm$.
- The distance between the heating table and the orifice of the cavity is $9mm$.
- $2\times$ Canon TSE lens with a focal length of $45mm$.
- $2\times$ $25mm$ $50/50$ beam splitter.
- Reflective mirrors with 90% reflectance.
- Nikon telecentric lens with $300mm$ focal length.
- NOVA FASTCAM $S12$ digital camera

To perform the experiment of the Helmholtz resonator, the high-speed $FastCam$ Nova $S12$ with resolution of 1024×1024 $pixels$, type $1000K - C - 32GB$ camera shown in $Figure$ 6.2.1 was used. $Figure$ 6.2.1(a) depicts the LED light source connected to the power supply. In front of the light source is a lens. The camera show in $Figure$ 6.2.1(b) has a focal length of $300mm$. Both the background and the plane of the object are within the depth of field of the lens. Images are taken at $12800fps$.

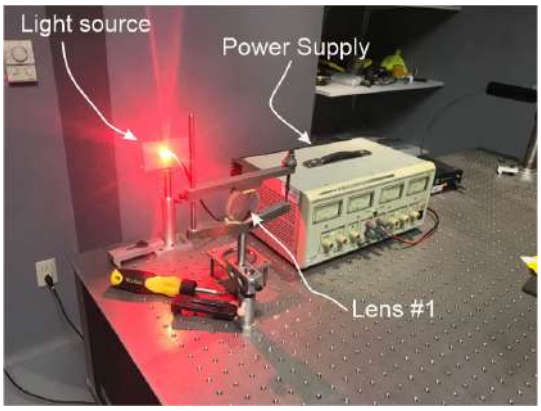

(a) Light source

(b) Nova $S12$ Camera

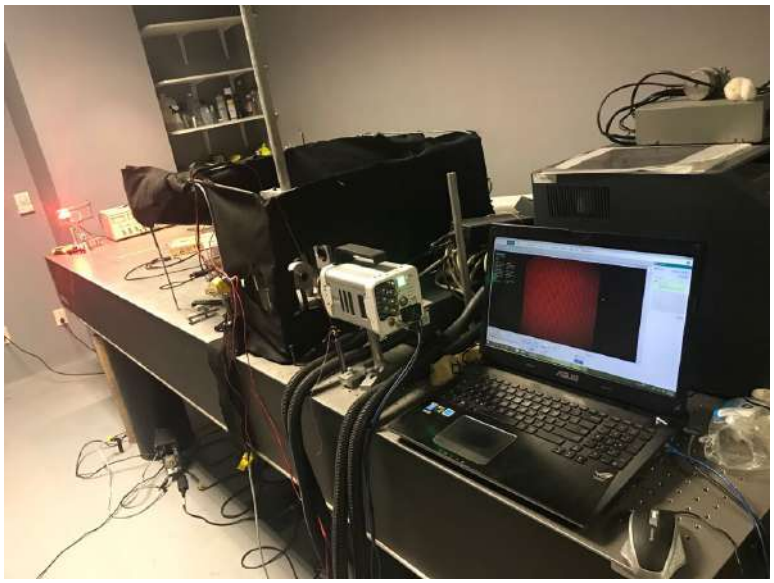

(c) Experimental set-up.

Figure 6.2.1: Experimental setup.

The Helmholtz resonator is a cavity with a speaker used as a diaphragm.
To show the inside of the covered back-box, a top view of the box was taken, shown in *Figure* 6.2.2.

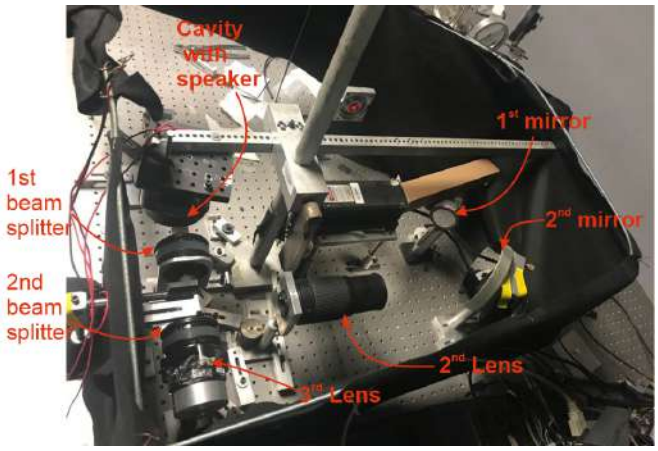

Figure 6.2.2: Top-view of the covered back-box.

To clarify the above experimental set-up, the schematic representation on the experimental set-up is shown in *Figure* 6.2.3.

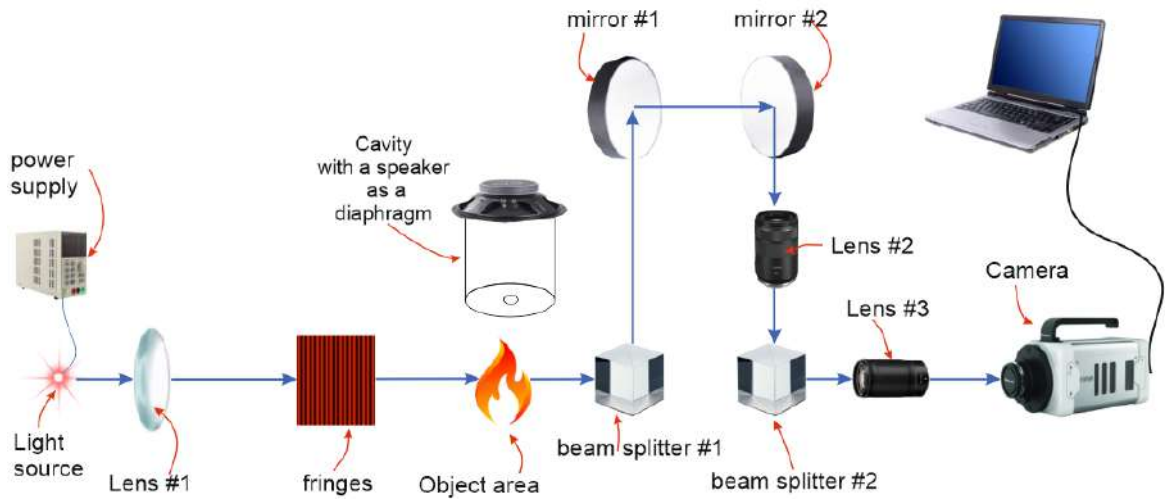

Figure 6.2.3: Schematic representation of a Helmholtz resonator experimental set-up.

An LED connected to the power supply is placed $24cm$ from lens number 1, which is placed $170cm$ from the fringes. The fringes forms the background pattern which is printed on a transparent slide and placed on the surface of an acrylic sheet. The distance from the fringes to the object area is $20cm$. Above the object area is the cavity with a speaker placed on top to form the diaphragm. The light then goes to the beam-splitter number 1 which is placed $6cm$ from the object, then to mirror number 1 placed $55cm$ from the 1st beam-splitter.The light is then deflected to mirror number 2 placed $14cm$ from mirror number 1. The light then goes through lens number 2 placed $30cm$ from mirror 2 before reaching to beam-splitter number 2 which is placed $25cm$. After the beam-splitter the light goes through lens number 3 which is placed $4cm$ from the beam-splitter, before reaching to the camera which is placed $25cm$ from lens number 3. The camera is connected to the computer for recording the captured images. The background is printed on a transparent slide and placed on the surface of an acrylic sheet. Both the background and the object plane are within the depth of focus of the lens.
Figure 6.2.4 shows the schematic representation of the object area and the device for generating the synthetic

air jet, $i.e.$ the area examined. The temperature value $(90°C)$ at the surface of the hot plate is set by the user, and he temperature $(47°C)$ at the bottom surface of the Helmholtz cavity is measured by a Thermocouple.

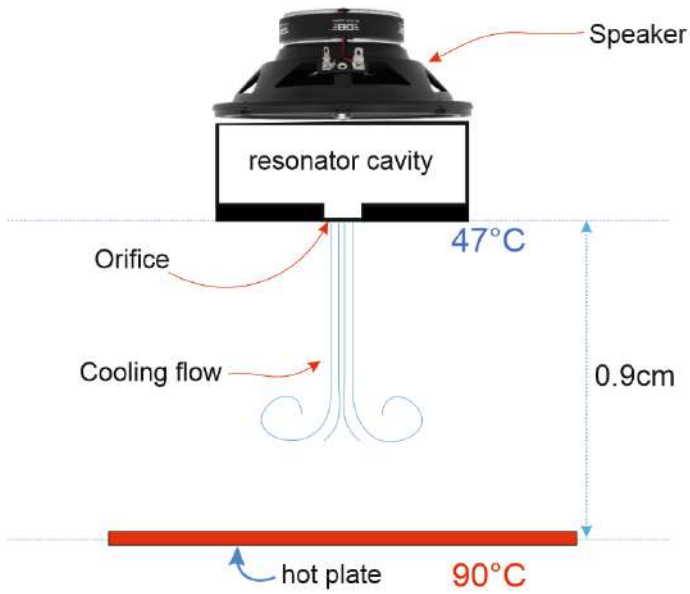

Figure 6.2.4: Object area.

When the light beam produced by the LED passes through the transparent ronchi, an image of the fringes is created in the camera sensors. Since the object area is between the fringes and the camera, the fringes form the background. The loudspeaker (membrane) is connected to a frequency generator, which lets out the smaller air in the cavity with the oscillation of the applied frequency. Since the cooler air is directed towards the hotter plate, the hot plate is cooled down.

6.2.2 Reynolds Number

It has been established that the properties of the synthetic jet depend heavily on two dimensionless parameters [5]. These are the Reynolds number and the Dimensionless Stroke Length.
The Reynolds number Re expresses the relationship between inertial forces (resistance to change or movement) and viscous forces (heavy and gluey or sticky).

$$Re = \frac{inertial\ force}{viscous\ force}, \tag{6.2.1}$$

For flow in a round (circular) pipe of diameter d with an average velocity U_0, the Reynolds number Re is defined as follows:

$$Re = \frac{\rho U_0 d_2}{\mu} = \frac{U_0 d_2}{\nu}, \tag{6.2.2}$$

where, μ is the dynamic viscosity of the fluid, and ρ is the density of the fluid, the ratio $\nu = \frac{\mu}{\rho}$ is called the kinematic viscosity, where d_2 is the diameter of the orifice, and U_0 is the average velocity of the orifice during the ejection part of the cycle at the outlet and on the axis of the orifice. In circular pipes, the transition from laminar flow to turbulent flow takes place over a Reynolds number range from around 2300 to 4000, regardless of the fluid type or pipe size or average speed. The only important thing is that this particular combination of parameters,

known as the Reynolds number, be within the stated range. Thus, if the Reynolds number is less than 2300, the flow can be expected to be laminar, and if it is greater than about 4000, the flow is turbulent. Between these two limits, the current is called the "transient flow". The Reynolds number helps predict flow patterns in various fluid flow situations.

The dimensionless stroke length L is defined as the distance that a surge of fluid travels through the orifice during the ejection phase of the synthetic jet. L plays a crucial role in the evolution of the synthetic jet.The dimensionless Stroke Length (L) is mathematically defined as:

$$L = \frac{l}{d_2}, \tag{6.2.3}$$

where l is the stroke length representing the amount of liquid ejected during the ejection portion of the cycle.

$$l = \int_0^{\frac{T}{2}} u_{cl}(t)dt. \tag{6.2.4}$$

also

$$U_0 = lf. \tag{6.2.5}$$

Here, $u_{cl}(t)$ represents the centerline velocity and f is the actuator frequency. If L is small, it means that the actuation frequency is high and therefore the same amount of fluid is processed in the suction and pressure stages, but at a great pace [17].

6.3 Results

The diameter of the cavity was measured to be $d_1 = 83mm$ with the height of $h_1 = 30mm$. The diameter of the orifice is $d_2 = 3mm$ and the orifice flow length is $12mm$. A speaker controlled by a sinusoidal signal generates the airflow (diameter of the speaker $= 83mm$). The speaker frequency corresponding to the first frequency of the resonance cavity, was calculated as follows:

$$f_{ref} = \frac{c}{2\pi}\sqrt{\frac{A_2}{V_1(l_2 + 1.5r_2)}}, \tag{6.3.1}$$

where $1.5r_2$ is the correction factor for the neck length. $A_2 = \pi(\frac{0.003}{2})^2 = 706.8 \times 10^{-8}m^2$, effective length of the neck is $l_e = l_2 + 1.5r_2 = 12 \times 10^{-3}m + 22.5 \times 10^{-4}m = 142.5 \times 10^{-4}m$,

$$V_1 = \pi r_1^2 h_1 + \tfrac{1}{2}lb(2\pi r_1)$$

$$V_1 = \pi(\tfrac{0.083}{2})^2(0.03) + \tfrac{1}{2}(\tfrac{3.5}{1000})(\tfrac{0.083}{2})2\pi(\tfrac{0.083}{2})$$

$$V_1 = 1.813 \times 10^{-4}m^3$$

$\frac{c}{2\pi} = \frac{343}{2\pi} = 54.59$, therefore:

$$f_{ref} \approx 90.3Hz. \tag{6.3.2}$$

The frequency generator was set to $90Hz$ for the $3mm$ orifice, which corresponds to the first resonant cavity frequency.

$A_2 = \pi(\frac{0.002}{2})^2 = 314.1 \times 10^{-8} m^2$ and $l_e = l_2 + 1.5r_2 = 135 \times 10^{-4} m$ results in the frequency of $f_{ref} \approx 61.8Hz$. In the experimental procedure, a frequency of $60Hz$ was used for the $2mm$ diameter orifice.

The heated surface is an aluminum plate heated to $90°C$. The state of the reference object relates to the convection plume generated by the plate surface at $90°C$, without the air jet. The result is an even temperature distribution over the plate surface, shown in $Figure$ 6.3.2(a). The temperature of the surface of the hot plate was kept at $90°C$ throughout the experiment.

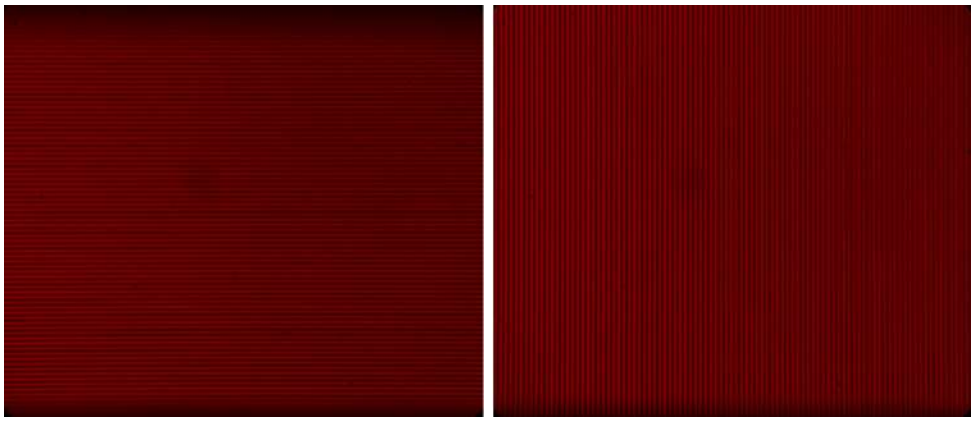

(a) horizontal fringes (b) vertical fringes

Figure 6.3.1: Fringe Deflection images for the analysis of the Helmholtz cavity $a)$ horizontal fringes for the heat convection flow from the hot plate, without air jet. and $b)$ vertical fringes for the synthetic air jet.

Using the horizontal fringes shown in $Figure$ 6.3.1(a), a reference image and an object image (with the heating plate turned on) are computed to produce the temperature change variation in $Figure$ 6.3.2a, to be used as a reference temperature.

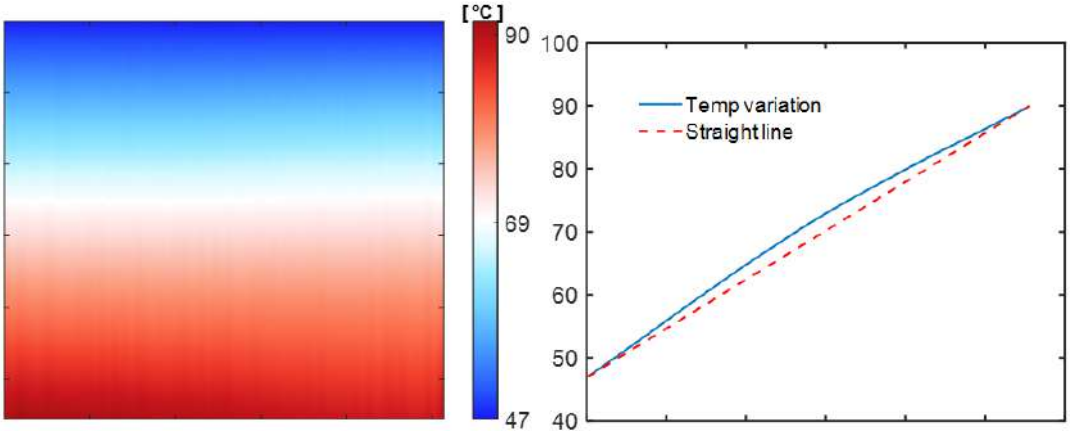

(a) Reference temperature (b) Vertical profile through the center of the reference temperature.

Figure 6.3.2: Reference temperature; $a)$ temperature variation ranging from $47°C$ to $90°C$, and $b)$ vertical profile through the center of the reference temperature.

$Figure$ 6.3.2(b) shows a vertical profile of the reference temperature variation from the top at approximately $47°C$ to the bottom hot plate at $90°C$. This profile shows the gradual increase in the reference temperature (blue

line) from top to bottom. The red dotted line shows a straight line from $47°C$ to $90°C$ for comparison. The reference temperature deviates slightly from the straight line, however it is accepted as it is quite linear.
A series of images of the object area were recorded (with the speaker switched on) for evaluation (using the vertical fringes). Fourier transforms were performed to extract the information from the fringes. The first half of a cyclical image sequence begins with the diaphragm (speaker) moving forward and expelling relatively cooler air through the cavity orifice. Four sets of data were experimentally collected and analyzed.

- 150 lines-per-in (fringes), $60Hz$ frequency $(3.0V)$, with a $2mm$ orifice diameter.
- 200 lines-per-in (fringes), $60Hz$ frequency $(2.1V)$, with a $2mm$ orifice diameter.
- 150 lines-per-in (fringes), $90Hz$ frequency $(2.5V)$, with a $3mm$ orifice diameter.
- 200 lines-per-in (fringes), $90Hz$ frequency $(2.5V)$, with a $3mm$ orifice diameter.

The ejected air jet forms a pair of vortices at the exit of the cavity. The vortices transverse downstream and lose their cohesion and become turbulent before reaching the hot plate. The images in $Figure$ 6.3.6 and $Figure$ 6.3.7 shows that the air jet interacts with the hot plate. On the surface of the heating plate, an enhanced mixing of the spatial structures can be observed through the dissolution of the vortex rings. A new cycle begins and a new air jet is generated. This air jet interact with the previous one and enhances the mixing process.
Based on the collected data, an estimated average velocity of $4.4m/s$ is calculated for the air jet for the 150 lines-per-inch, $2mm$ orifice diameter, $3.4m/s$ is calculated for the air jet for the 200 lines-per-in, $2mm$ orifice diameter, $4.2m/s$ is calculated for the air jet for the 150 lines-per-inch, $3mm$ orifice diameter and $3.3m/s$ is calculated for the air jet for the 200 lines-per-inch, $3mm$ orifice diameter.
The results are shown below. $Figure$ 6.3.3 and $Figure$ 6.3.4 are part1 and part2 of the results for 150 lines-per-inch (fringes), $60Hz$ frequency $(3.0V)$, with a $2mm$ orifice diameter. $Figure$ 6.3.6 and $Figure$ 6.3.7 shows the results for part1 and part2, respectively, of the 200 lines-per-inch (fringes), $60Hz$ frequency $(2.1V)$, with a $2mm$ orifice diameter. In $Figure$ 6.3.9 and $Figure$ 6.3.10 are the results for 150 lines-per-inch (fringes), $90Hz$ frequency $(2.5V)$, with a $3mm$ orifice diameter. Lastly the results for 200 lines-per-inch (fringes), $90Hz$ frequency $(2.5V)$, with a $3mm$ orifice diameter are shown in $Figure$ 6.3.12 and $Figure$ 6.3.13.
The following set of images shows the phase in radians and the calculated temperature for the 150 lines-per-inch at a frequency of $60Hz$, $3V$, for a cavity with an orifice diameter of $2mm$.

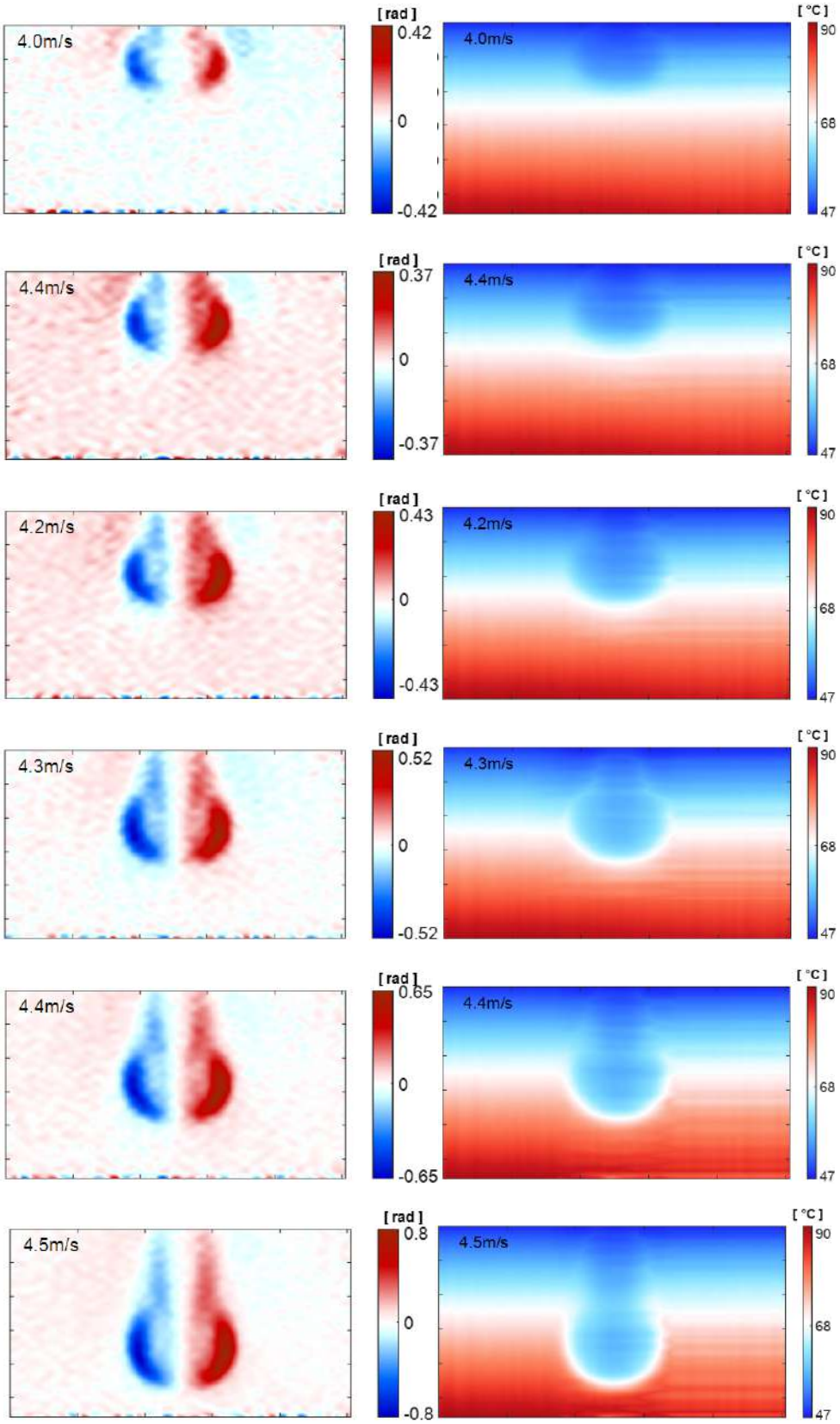

Figure 6.3.3: Part 1: results for 150 lines-per-in (fringes) $60Hz$ frequency $(3.0V)$, $2mm$ orifice diameter. Beginning and descending of the pulse from top to bottom. The column to the left shows the phase of the air jet. The column to the right shows the temperature variation.

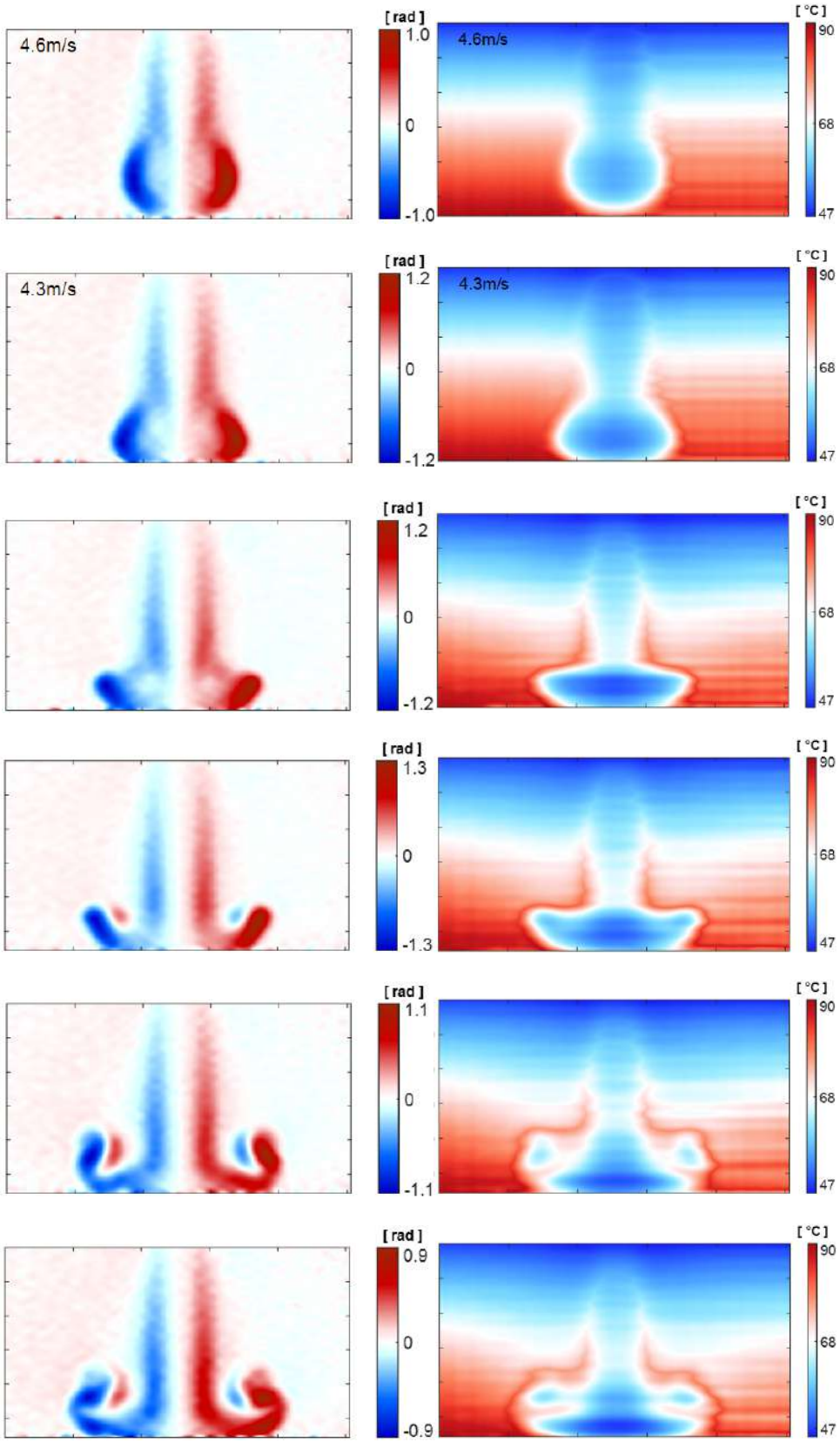

Figure 6.3.4: Part 2: results for 150 lines-per-in (fringes) $60Hz$ frequency $(2.5V)$, $2mm$ relative cooler air jet descending through the warmer temperature, eventually coming into contact with the hot surface at the bottom.

$Figure$ 6.3.3 and $Figure$ 6.3.4 illustrate cooler air jet ejected from the Helmholtz cavity. The air jet is a $2D$ representation of a circular mushroom-shaped $3D$ sphere made of cool air that descends in a warm air environment at an average speed of $4.3m/s$. As the spherical ball of cool air moves down, it leaves a trail of cool air behind, eventually comes into contact with the hot surface and begins to mix. The figures on the left-hand-side are the phase in radians, and the figures on the right-hand-side are the temperature in degrees Celsius.
$Figure$ 6.3.5 below shows the density of the descending ball of air, for few selected frames. The density varies from $0.87kg/m^3$ in the upper part of the observation area, where the ambient air has a temperature of $(47°C)$, to $0.77kg/m^3$ on the lower hot surface. The relatively cooler, high-density air jet descends at an average speed of $4.4m/s$ to the lower edge of the field of vision where the hot plate is located. The observation in $Figure$ 6.3.5 are for the $150lpi$, when $60Hz$ at $3V$ is applied to the Helmholtz resonator cavity with an orifice of $2mm$.

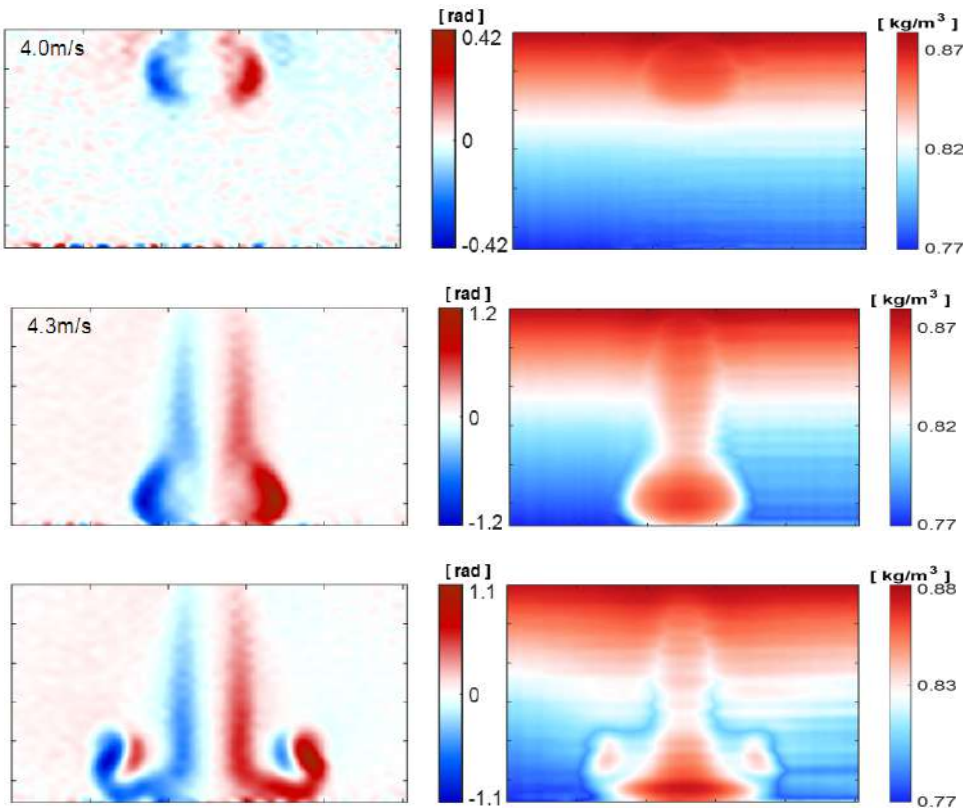

Figure 6.3.5: Density variation of the air jet as it descends from the top to the bottom hot plate.

The following discussion is about the effect of increasing the fringes (lines-per-inch) from 150 to 200 when a frequency of $60Hz$ at $2.1V$ is applied to the cavity with a $2mm$ orifice diameter. The series of images shows the point at which the cooler air jet is ejected out of the cavity until the air jet hits the hot surface and mixes with the warmer air.

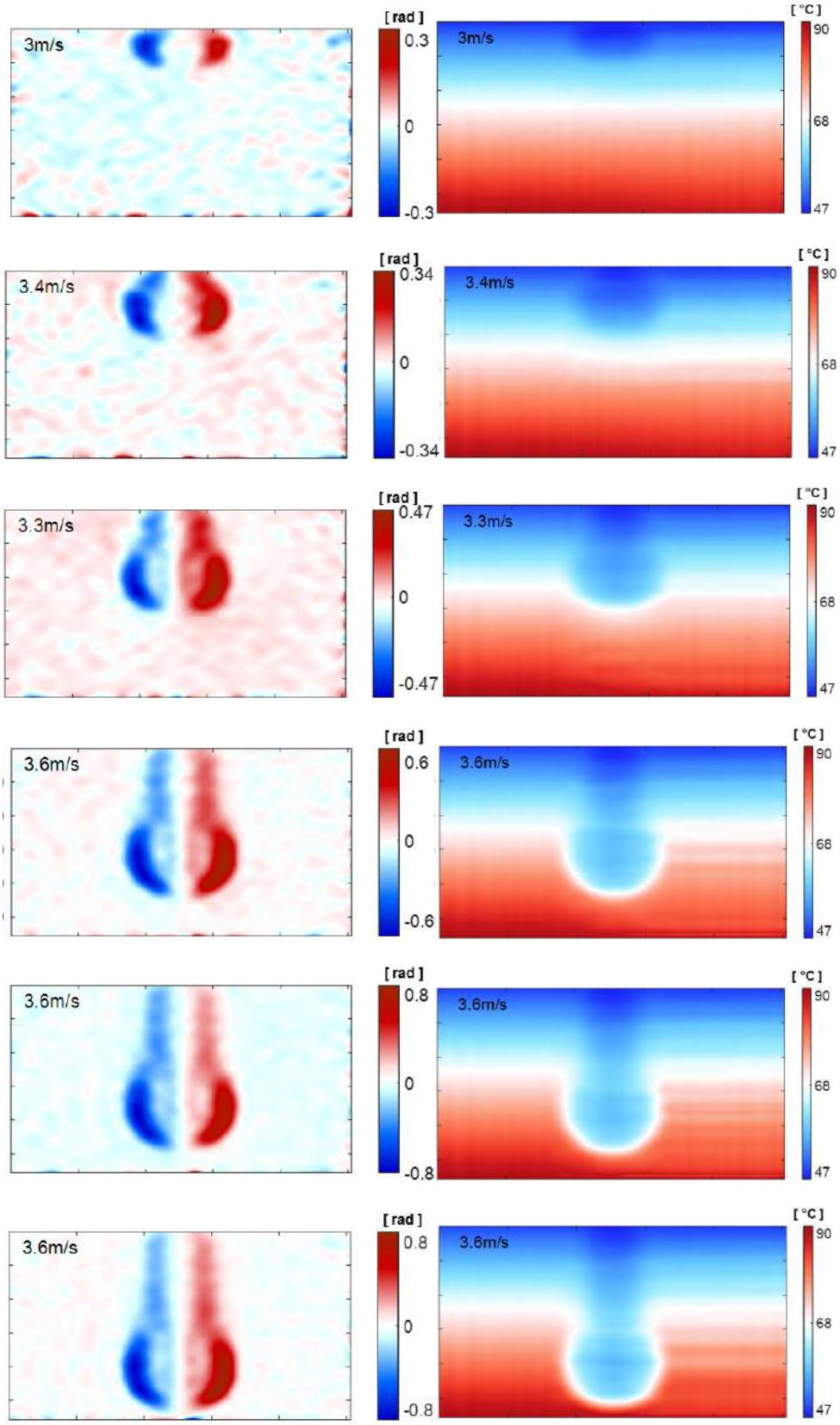

Figure 6.3.6: Part 1: results for 200 lines-per-in (fringes) $60Hz$ frequency $(2.1V)$, $2mm$ orifice diameter. Beginning and descending of the pulse from top to bottom. The column to the left shows the phase of the air jet. The column to the right shows the temperature variation.

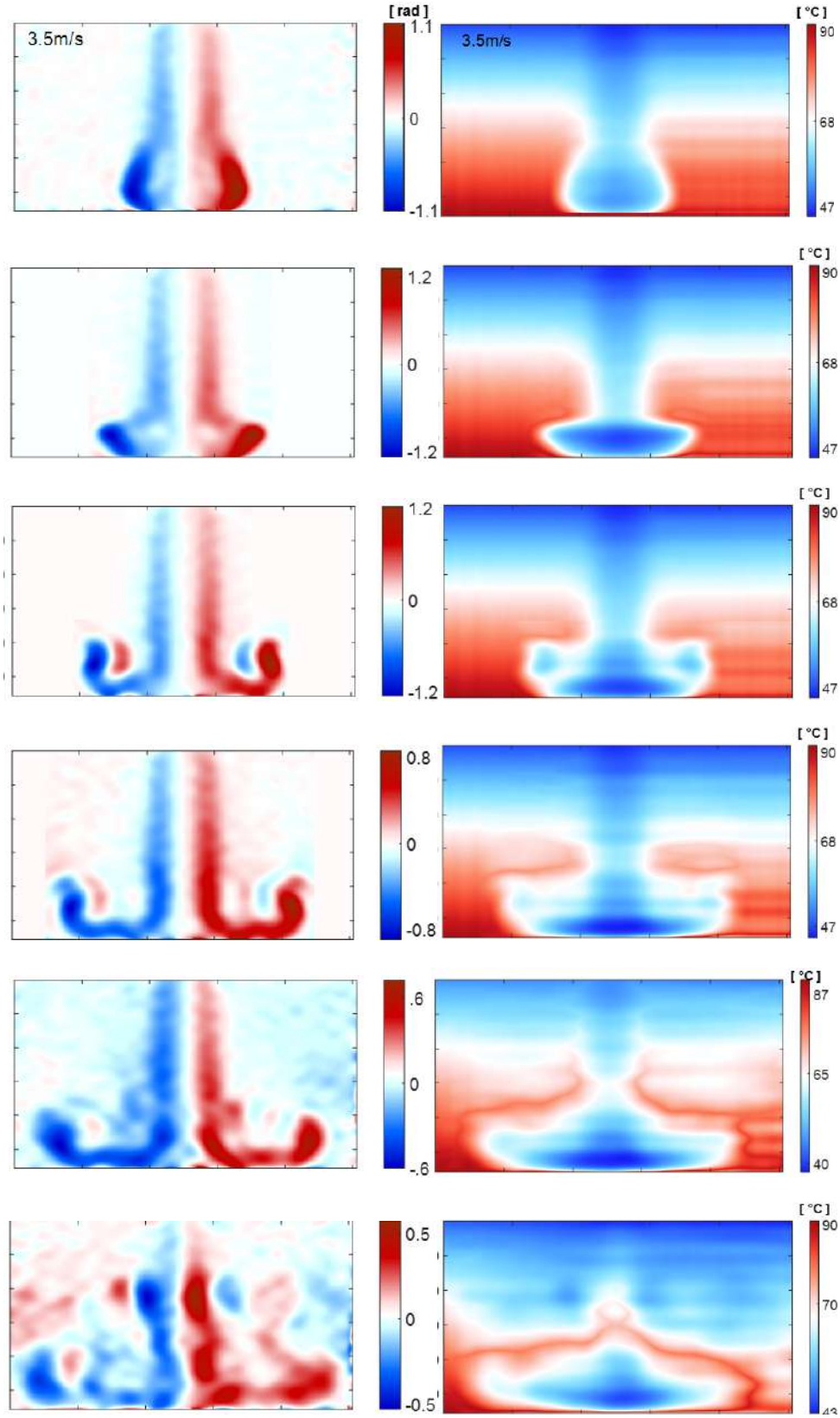

Figure 6.3.7: Part 2: results for 200 lines-per-in (fringes) $60Hz$ frequency $(2.1V)$, $2mm$ relative cooler air jet descending through the warmer temperature, eventually coming into contact with the hot surface at the bottom.

$Figure$ 6.3.8 shows the density variation of the air jet in the range from $0.88kg/m^3$ to $0.77kg/m^3$. The air jet has a relatively high density compared to the surrounding hot air. The trailing tail and the mixing at the edges of the air jet density is clearly visible.

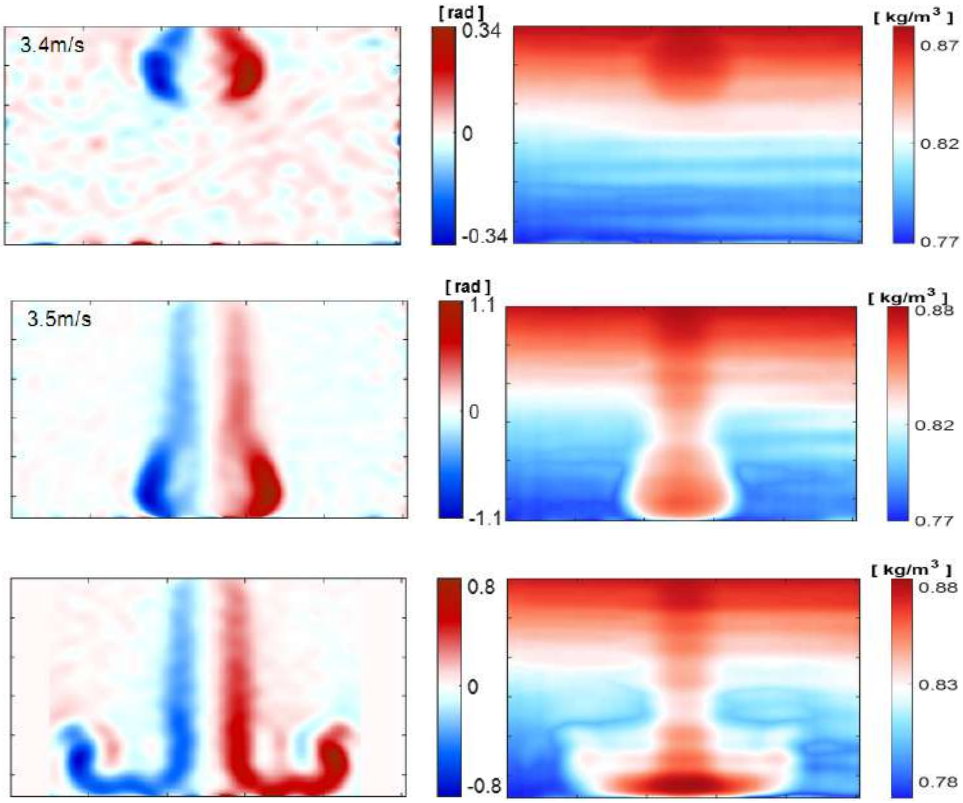

Figure 6.3.8: The phase of the air jet is shown to the left of its density on the right.

The size of the orifice diameter was changed to $3mm$ and based on the calculations in Section 6.3, the driving frequency was set to $90Hz$. $Figure$ 6.3.9 and $Figure$ 6.3.10 show a series of density and temperature images for 150 lines-per-inch, $90Hz$ frequency $(2.5V)$ applied to a cavity with a $3mm$ orifice diameter. The air jet takes an average of $4.2m/s$ to descend from top to bottom.

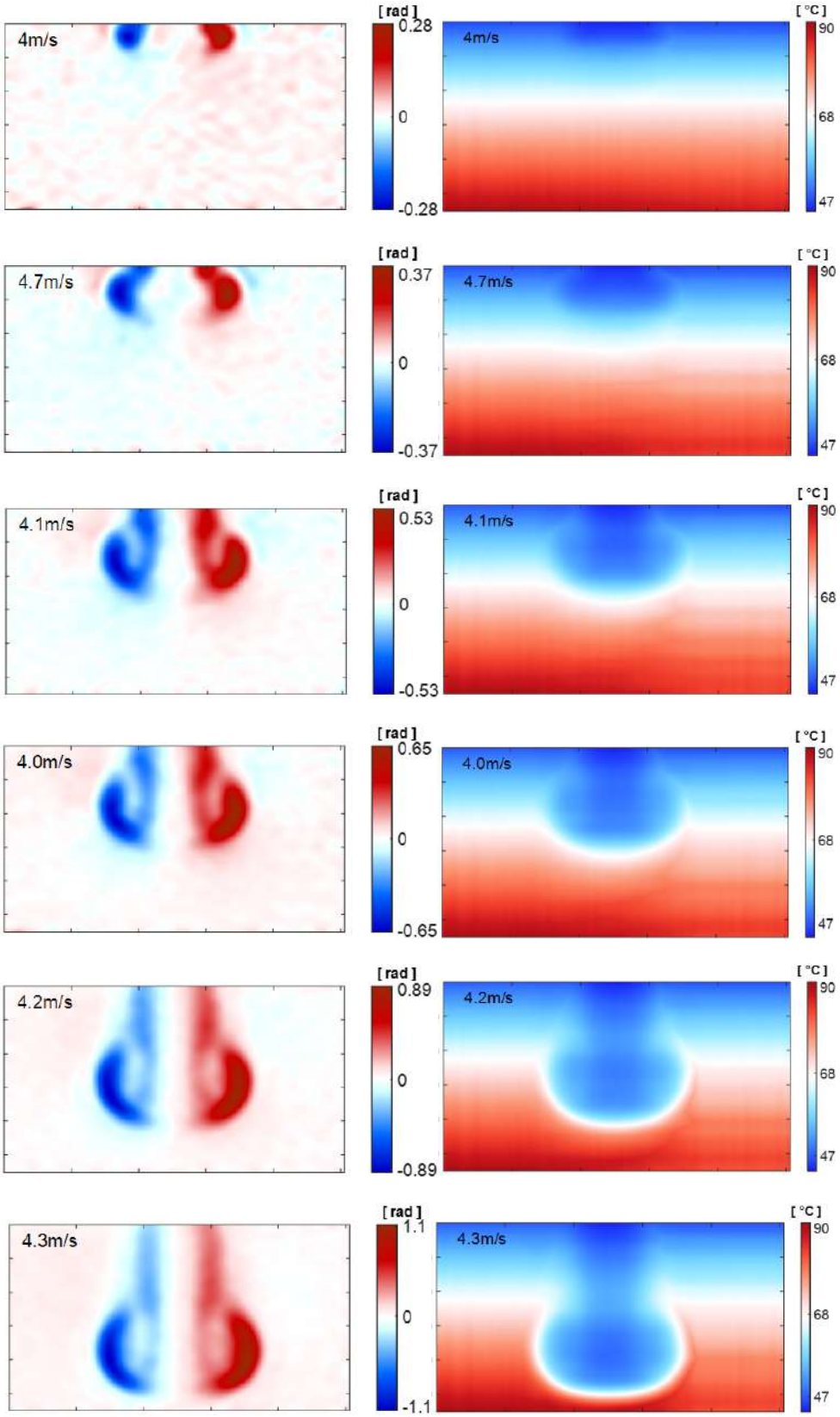

Figure 6.3.9: Part 1: results for 150 lines-per-in (fringes) $90Hz$ frequency $(2.5V)$, $3mm$ orifice diameter. Beginning and descending of the pulse from top to bottom. The column to the left shows the phase of the air jet. The column to the right shows the temperature variation.

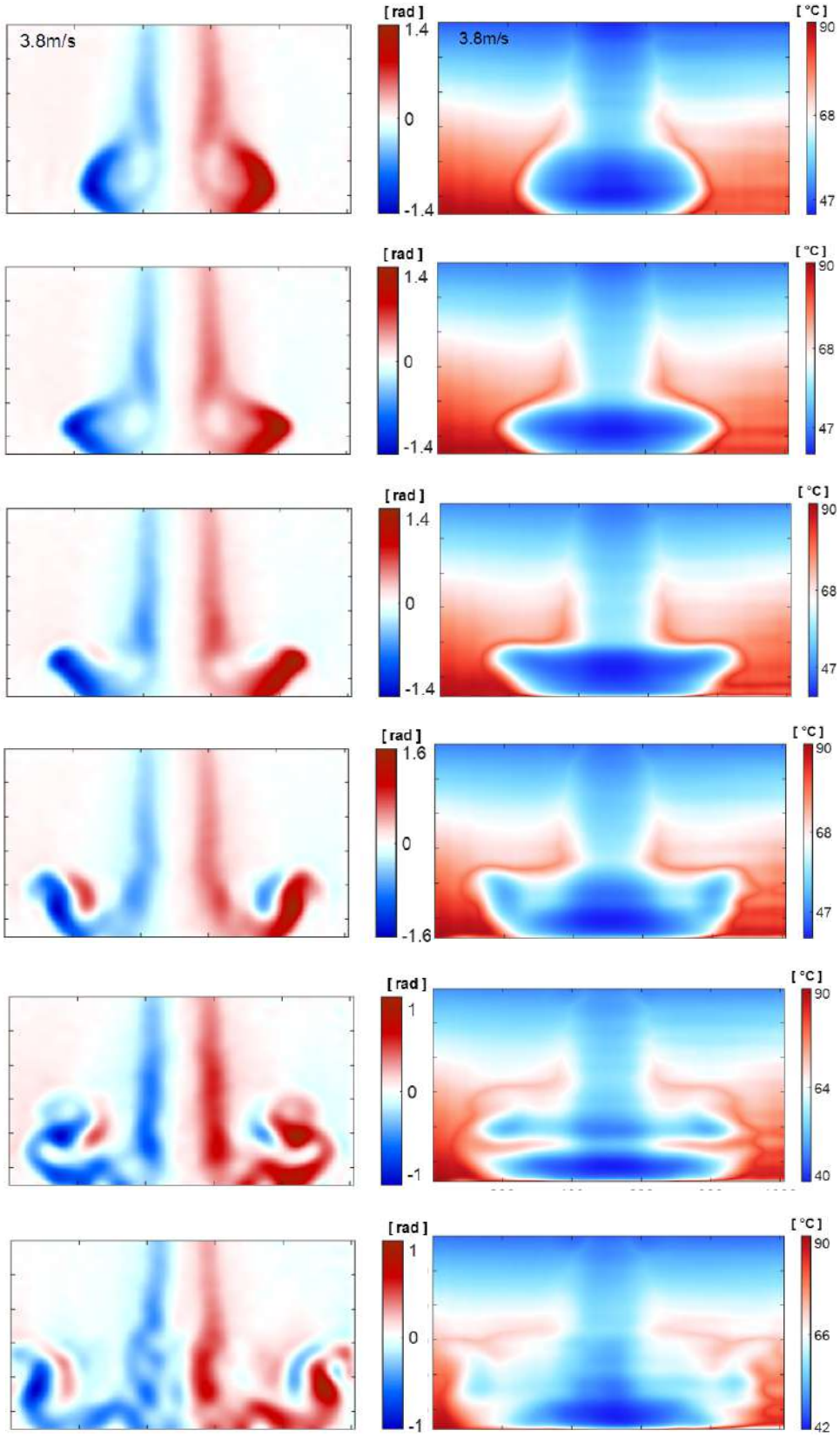

Figure 6.3.10: Part 2: results for 150 lines-per-inch (fringes) $90Hz$ frequency $(2.5V)$, $3mm$ relative cooler air jet descending through the warmer temperature, eventually coming into contact with the hot surface at the bottom.

The density of the air jet is shown in $Figure$ 6.3.11, where the mushroom shape can be clearly seen and the mixing of the different densities can be clearly observed.

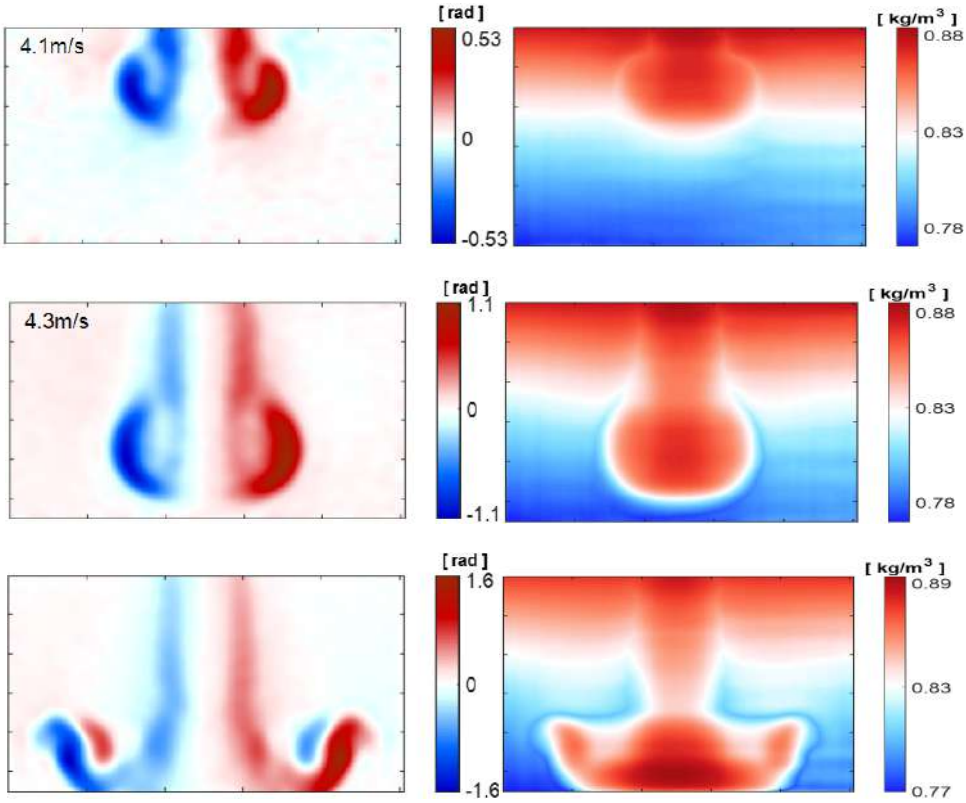

Figure 6.3.11: Phase clearly visible in radians and density variation in kg/m^3.

Results for 200 lines-per-inch, $90Hz$ frequency $(2.5V)$ applied to a cavity with a $3mm$ orifice diameter are shown in $Figure$ 6.3.12 and $Figure$ 6.3.13. The average velocity for the air-jet is $3.3m/s$. The $3mm$ orifice diameter allows a much clearer observation of the air jet. The trailing tail in phase images is clearer and the mushroom shape is clearly visible in temperature images. In addition, for the $150lpi$ case, higher air jet velocity is observed than in the case of $200lpi$. This is due mainly to the lack of repeatability of the Helmholtz resonator, since the movable diaphragm is a simple paper membrane.

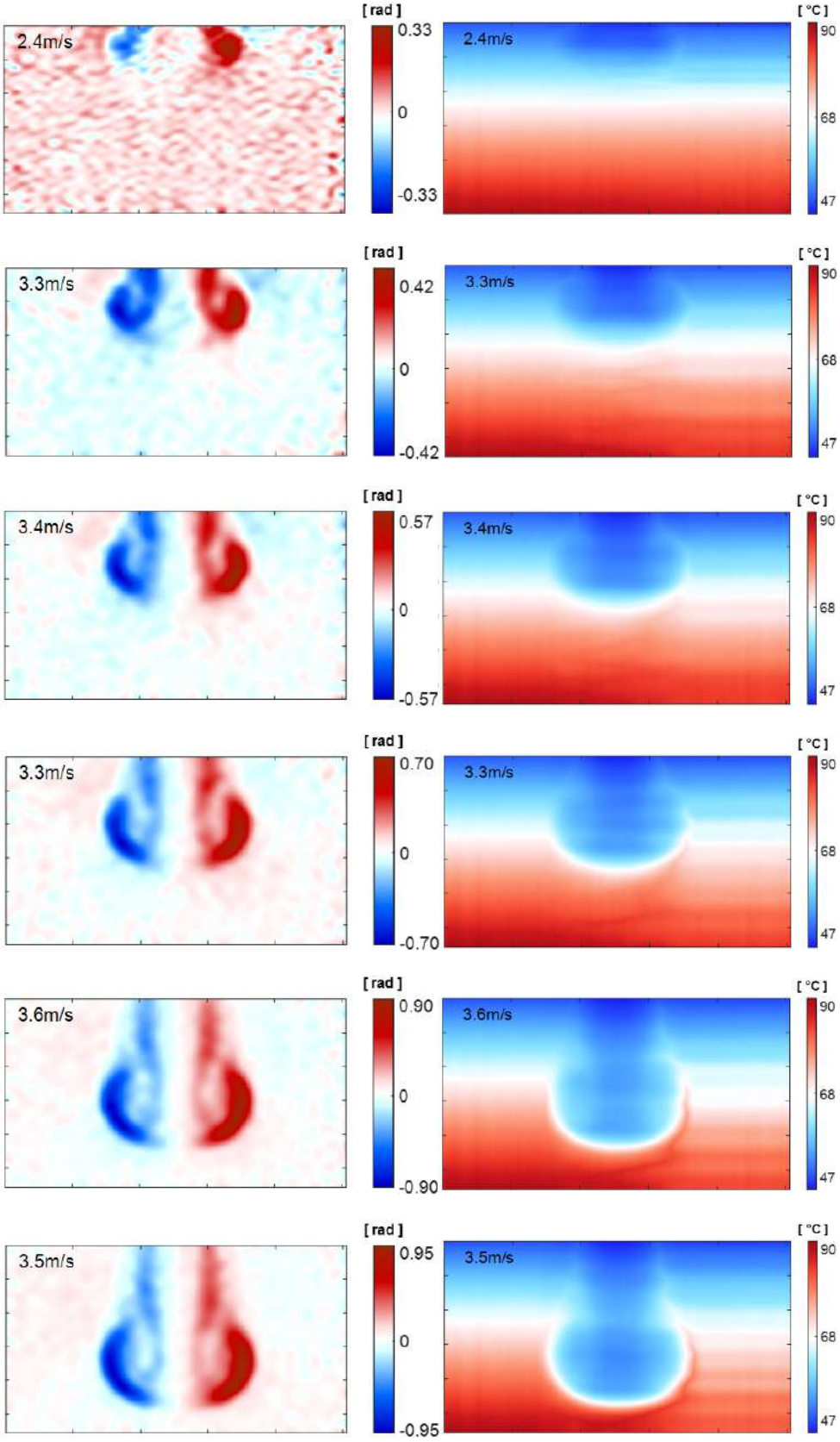

Figure 6.3.12: Part 1: results for 200 lines-per-inch (fringes) $90Hz$ frequency $(2.5V)$, $3mm$ orifice diameter. Beginning and descending of the pulse from top to bottom. The column to the left shows the phase of the air jet. The column to the right shows the temperature variation.

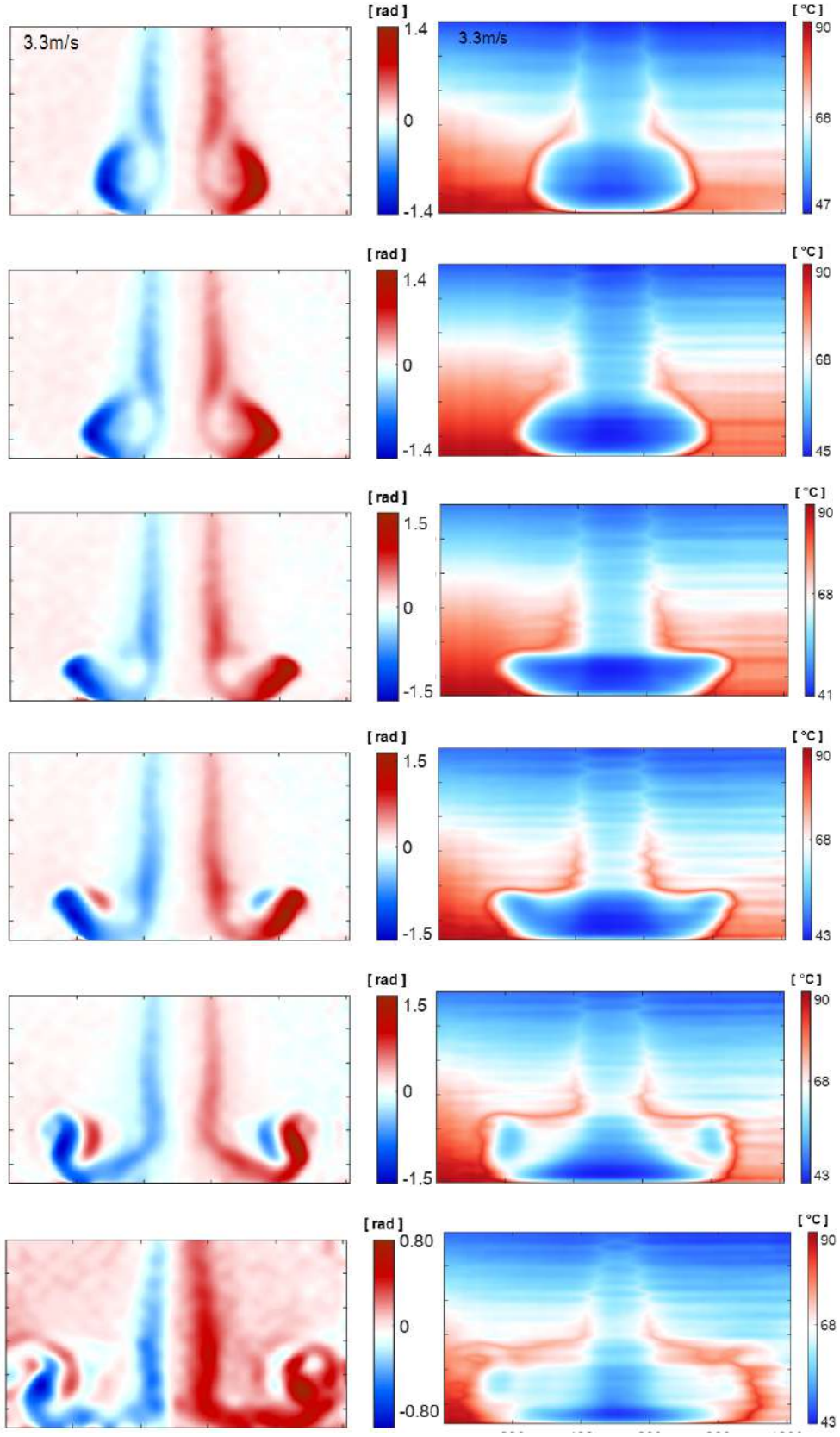

Figure 6.3.13: Part 2: results for 200 lines-per-inch (fringes) $90Hz$ frequency $(2.5V)$, $3mm$ relative cooler air jet descending through the warmer temperature, eventually coming into contact with the hot surface at the bottom.

The density variation of the descending air jet is shown in $Figure$ 6.3.14 below. As the ball of high density descends to the hot plate, it causes mixing with the surrounding low density caused by the heated plate.

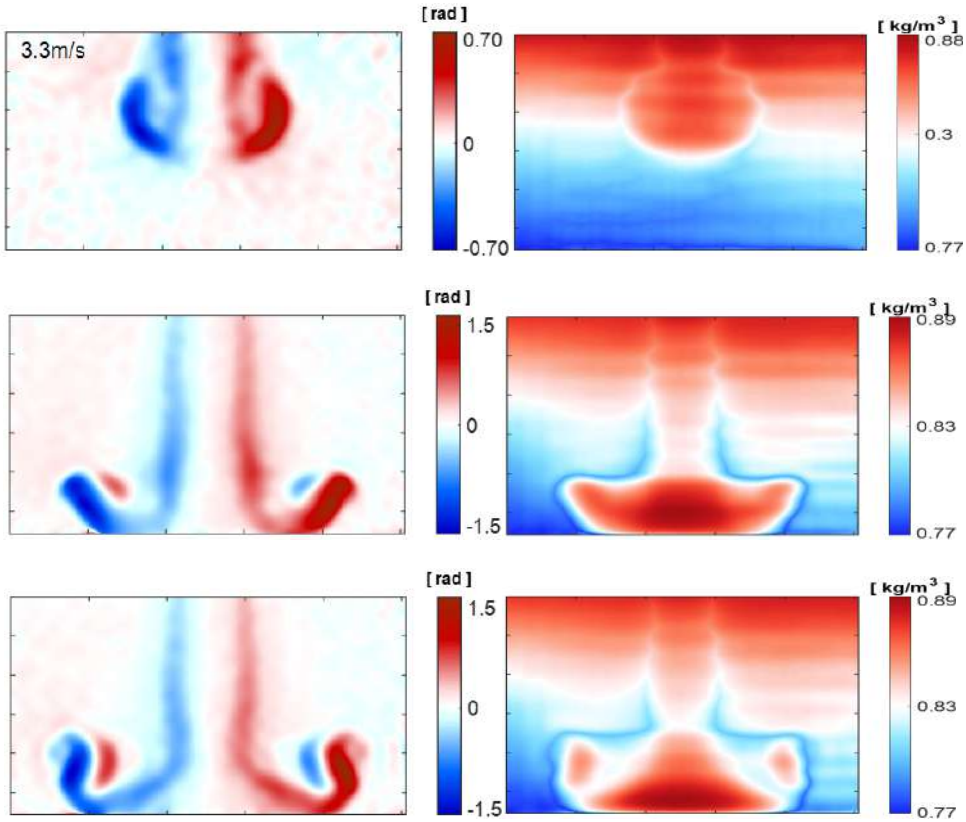

Figure 6.3.14: Phase in rdadians and density kg/m^3.

In subsequent cycles, the full periodicity of the phenomenon is observed. The air jet dynamics is represented by the associated temperature field, taking into account that the variation in the refractive index is axisymmetrical and is modeled as a Gaussian function of (y, z), according to, for example, $Eq.$(2.4.26). The temperature values are obtained by the $Eq.$(2.3.8), which requires the reference temperature T_0 at each point. The value of T_0 at each point can be determined by measuring the temperature field by comparing images without a convection plume (hot plate off, room temperature $24°C$) with images with an existing convection plume (hot plate set to $90°C$) - no synthetic air jet for both images, shown in $Figure$ 6.3.2. In this first part, horizontal fringe pattern was used. For the variation of the refractive index, the integration process is performed along the vertical direction (vertical fringe pattern). The resulting synthetic jet temperature maps are obtained and are shown from $Figure$ 6.3.3 to $Figure$ 6.3.13. The formation of a synthetic air jet with each cycle is clearly visible.

The synthetic jet transports air from the exit orifice of the cavity. As the cool air from the cavity approaches the heated plate, it heats up (becomes warmer). After the collision with the heating plate, a further increase in the temperature of the air jet is observed. A new ejection period begins and the new jet begins to interact with the debris from the previous jet. The results shows that the synthetic jet entrails cool air from the environment, impinges on the lower heated plate surface and circulates the surrounding air back to the environment. Eddies from the synthetic air jet that impinge on the heat surfaces create a turbulent surface renewal effect that increases heat transfer from the impact surface. The vortex structure is stretched radially after impact, increasing in size

and strength, rolling outward along the flat surface and breaking into turbulence that coalesces with the hot air, improving heat transfer performance.

The air ejected from the orifice should have sufficient self-induced velocity or high enough vortex strength to be able to travel all the way down to the plate. The Reynolds number and the dimensionless stroke length and computed and tabulated below. Reynolds number, density of air in León, Guanajuato, Mexico is $\rho = 0.94\frac{kg}{m^3}$, the dynamic viscosity of air at $25°C$ is $\mu = 1.184 \times 10^{-5}\frac{kg}{m \cdot s}$.

Experiment	**Velocity** (U_0)	**Reynolds #** (Re)	**Stroke-length** (L)
150 fringes, $2mm$ orifice diameter.	$4.4m/s$	699	36.7
200 fringes, $2mm$ orifice diameter.	$3.4m/s$	540	28.3
150 fringes, $3mm$ orifice diameter.	$4.2m/s$	1000	15.6
200 fringes, $3mm$ orifice diameter.	$3.3m/s$	786	12.2

Table 6.1: Computed Reynolds numbers, and the dimensionless stroke-length.

The calculated Reynolds numbers are all below 2000, which means that the air jet streams are laminar. Since the velocities are calculated before the air jet hits the hot plate, the Reynolds number indicates that the flow is laminar before impact but tabulated after impact. The L values are well above the threshold of $L = 4$, which is the jet-forming state. Values of L less than 4 results in a suppressed synthetic jet formation. Any value greater than $L = 4$ indicates that the expelled air jet is strong enough to drift downstream [17].

As can be seen in the images, the trailing jet becomes more pronounced as the strength of the air jet increases which leads to a strong mixing and hence, turbulent intermittent jet immediately after impact with the surface.

6.4 Conclusions

After performing better in the simulations in terms of noise handling, accuracy and robustness, the Fringe Deflection technique was used to measure the temperature of a synthetic jet of air as it interacts with the heat flow generated by a heated (hot) surface in the Helmholtz Resonator experiment. The jet of air moves downstream and entrains the surrounding hot air and grows in width. The results show the occurrence of synthetic air-flow and the subsequent downward movement that occurs for about half the drive frequency cycle. In the other half of the observed period, the airflow interacts with the top of the hot plate and draws in the heated air around the hot plate. Although the area of interest in the vertical direction is relatively small at $0.9cm$, the results show that the fringe deflection method can potentially be used for the analysis of Helmholtz resonators for temperature measurement experiments.

New technologies such as synthetic air jets have the potential to meet the fast growing cooling requirements of electronic components. Synthetic air jets are a promising new technology which has shown to be capable of providing cooling of continuous air jet impingement. Various values of frequency and orifice diameter were examined to determine which values optimize the performance of the Helmholtz resonator. Frequency is directly proportional to the area of the orifice, therefore, an increase in the orifice diameter leads to an increase in the frequency. Therefore $90Hz$ was used for the $3mm$ diameter and $60Hz$ for the $2mm$ diameter. This fact is also demonstrated in the frequency calculation in Section 6.3. It is also observed that better results, those that

generate fringes with a lager value of contrast, are obtained by the use of the grating of $150lpi$. The grating of $200lpi$ takes the imaging system to the limit of spatial resolution. However, for gratings with lower density of fringes, resolution is lowered.

Bibliography

[1] A. P. Dowling, and J. E. Ffowcs Williams, "Sound and Sources of Sound", Wiley, New York, Chap.6 (1983).

[2] C. Soares, "Gas Turbines: A Handbook of Air, Land and Sea Applications", Butterworth-Heinemann, San Diego, CA, 2008, Chap.3.

[3] A. Selamet, V. Kothamasu, and J. Novak, "Insertion loss of a Helmholtz resonator in the intake system of internal combustion engines: an experimental and computational investigation," Applied Acoustics, vol. 62, no. 4, 381–409 (2001).

[4] U. Ingard, "On the theory and design of acoustic resonators", J. Acoust. Soc. Am., 25(6), 1037-1061 (1953).

[5] B. L. Smith, and A. Glezer, "The formation and evolution of synthetic jets", Phys. Fluids, 10(9), 2281-2297 (1998).

[6] B. Barrientos, M. Cywiak, W. K. Lee, and P. Bryanston-Cross, "Measurement of dynamic deformation using a superimposed grating", Rev. Mex. Fis. 50, 12-18 (2004).

[7] K. J. Gasvik, "Optical Metrology", 3rd Ed. John Wiley and Sons, Sussex (2003).

[8] C. Alvarez-Herrera, D. Moreno-Hernandez, and B. Barrientos, "Temperature measurement of an axisymmetric flame by using a schlieren system", J. Opt. A: Pure Appl. Opt., 10, 104014, 7 (2008).

[9] W. Hauf, and U. Grugull , "Optical methods in heat transfer", Academic Press Inc., New York, 166-167 (1970).

[10] O. S. Jensen, J. P. Kunsch, and T. Rosgen, "Optical density and velocity measurements in cryogenic gas flows", Exp. Fluids 39, 48-55 (2005).

[11] H. Schardin, "Toepler's schlieren method, basic principles for its use and quantitative evaluation", Selected Papers on Schlieren Optics, SPIE Milestones Series Vol. MS61, SPIE Bellingham, WA. (1992).

[12] A. McGuinn, T. Persoons, T. S. O'Donovan, P. Valiorgue, and D.B. Murray, "Heat transfer measurements of an impinging synthetic air jet with constant Stroke length", 5th European Thermal-Sciences Conference, The Netherlands (2008).

[13] T. Persoons, and T. S. O'Donovan, "A pressure-based estimate of synthetic jet velocity", Physics of Fluids 19, 128104-1 (2007).

[14] J. Davis, and P. Rabinowitz, "Methods of Numerical Integration", Academic Press Inc., New York, 51-52 (1984).

[15] U. Ingard, "Notes on Acoustics", Infinity Science press LLC (2008).

[16] U. Ingard, "On the theory and design of acoustic resonators", J. Acoust. Soc. Am., 25(6), 1037-1061 (1953).

[17] G. Krishan, K. C. Aw, and R. N. Sharma , "Synthetic jet impingement heat transfer enhancement – A review", Applied Thermal Engineeruing, 149, 1305-1323 (2019).

[18] M. Gillespie, W. Black, C. Rinehart, and A. Glezer, "Local convective heat transfer from a constant heat flux flat plate cooled by synthetic air jets", J. Heat Transf. 128, 990–1000 (2006).

Chapter 7

Conclusions

Contents

7.1 Summary

The success of Schlieren temperature measurement technique is due to the relatively simple implementation, low costs, the use of conventional light sources and the high and variable sensitivity. This dissertation demonstrated the feasibility of techniques for measuring the various physical parameters of transparent media of interest, such as temperature, density gradient and variation of the refractive index in space.

Based on the results of the analysis of the simulated noise, the robustness and the sensitivity of the analyzed techniques, it is concluded that the Background Oriented Schlieren with a randomly located dots pattern and the Fringe deflection methods are not sensitive to external noise when using white light, which is advantageous for performing parameter measurements of transparent media. The algorithm developed is robust and works better because the results generated are error-free and can be used in a wide variety of application scenarios.

In terms of the complexity of the developed codes and the amount of processing, the requirements of the techniques are more or less similar. However, in the Background Oriented Schlieren with a randomly located dots pattern, relatively complex correlation techniques are used compared to the complex phase unwrapping algorithms that are commonly used in the Fringe Deflection method. The results shows that the Fringe Deflection technique gives better results than the Background Oriented Schlieren method.

From this it can be concluded that, although Background Oriented Schlieren and Fringe Deflection techniques are based on the calculation of the derivative of the refractive index, the results are of very high quality and reliability. In addition, the integration process is mainly implemented to reconstruct the refractive index, but in this study the process of dividing by x to reconstruct the refractive index was analyzed as well. It can therefore be concluded that the act of dividing by x, while relatively simple, causes a large number of errors. For this reason, the vast majority of researchers prefer the integration method. The main reason the division by x method has been studied is because there may be certain scenarios where using this method might be a better solution.

The results of the experiments showed good agreement between them, however, only the FD was implemented in the analysis of the Helmholtz resonator. In the Helmholtz's experiment, a transparent air jet was successfully recorded and visualized as it exits the cavity orifice until it impacts the hot surface. The mushroom-shaped vortexes were clearly recorded, with the temperature and density properly reconstructed for measurement and visualization. The mixing of the cooler air jet with the hotter air from the heated hot place was visualized. The mixture of the cooler airflow with the warmer air from the heated hot plate was visualized. When the process is repeated, the expulsion of air from the cavity cools the hot spot, and the process can be controlled by varying the frequency at which the cavity membrane is pushed up and down and the orifice diameter.

Some of the advantages and disadvantages of Background Oriented Schlieren techniques are listed below:

7.1.1 Advantages of BOS

7.1.1.1 Schlieren imaging without expensive, large-scale precision optics.

BOS has extremely simple and very modest technical requirements, which offers the advantage of portability and promises the use of existing and natural backgrounds.

7.1.1.2 Large field-of-view

BOS experiments offer a large field-of-view compared to conventional Schlieren optics. The field of view of the BOS can be at least half the size of the background.

7.1.1.3 Unique solution

BOS offers a unique solution to some problems that normally do not have significant optical access for traditional Schlieren or Shadowgraphy.

7.1.2 Disadvantages of BOS

7.1.2.1 Limited resolution

Since image cross-correlation algorithms average over the interrogation window size, BOS always offers a lower image resolution than comparable traditional Schlieren instruments. An increase in the BOS sensitivity also requires a larger interrogation window and thus a lower resolution.

7.1.2.2 Limited real-time imaging

BOS requires post processing on a capable computer running FFT-based image cross-correlation code. The computing power and graphics processing unit needed to perform real-time imaging and analysis are not currently available.

7.1.2.3 Difficulty in attaining sharp focus on both subject and background

A small aperture on the camera and a short distance from the Schlieren object to the background are recommended to minimize the difficulty of getting both the object and the background into sharp focus.

7.1.2.4 Vibration sensitivity

Vibration or anything other than the Schlieren object, changing the exposure area (interrogation region) leads to undesirable problems.

7.2 Contribution to the Field/Discipline

The following contributions were made:

- Provided insight into the dynamic performance of the Helmholtz resonator by using the Fringe Deflection technique.
- Reconstruction of the refractive index without integration process, used the method of dividing $\triangle x$ by x.
- A simple deprojection method has been proposed.

7.3 Future Work

The proposed future work includes:

- Use software that allows calculation of parameters in real time.
- Improve on the experimental set up and post-processing to reduce errors.
- Examine a Helmholtz resonator with more than one orifice of different diameters.

- Use crossed fringes. This will enables displacement sensitivity in two mutually perpendicular directions, allowing information on the gradients in both directions to be obtained.

Bibliography

[1] Blanco A., Barrientos B., and Mares C. Performance comparison of background-oriented schlieren and fringe deflection in temperature measurement, part 2: experimental evaluation. *Opt. Eng. , 55(6), 054102*, 2016.

[2] Blanco A., Barrientos B., and Mares C. Performance comparison of background-oriented schlieren and fringe deflection in temperature measurement, part 2: Numerical evaluation. *Opt. Eng., 55(5), 064104*, 2016.

[3] Fomin N. A. Speckle photography for fluid mechanics measurements. *Springer - Verlag, Berlin*, 1997.

[4] Meier A. and Roesgen T. Improved background oriented schlieren imaging using laser illumination. *Exp. Fluid 54:1549*, 2013.

[5] Meier G. A. Computerized background-oriented schlieren. *Exp. Fluids, 33, 181-187*, 2002.

[6] Adrian. Scattering particle characteristics and their effect on pulsed laser measurements of fluid flow: speckle velocimetry vs particle image velocimetry. *App. Opt. 23, 1690-1691*, 1984.

[7] Halliwell N. A.Pickering C. J. D and. Particle image velocimetry: a new field measurement technique, optical measurements in fluid mechanics. *Adam Hilger, 147-152, Bristol, U. K.*, 1985.

[8] Barker D. B. and Fourney M. E. Measuring fluid velocities with speckle pattern. *Opt. Lett., 1, 135-137*, 1977.

[9] Barrientos B., Cerca M., Garcia-Marquez J., and Hernandez-Bernal C. Three-dimensional displacement fields measured in a deforming granular-media surface by combined fringe projection and speckle photography. *J. Opt. A.: Pure Appl. Opt., 10, 104027, 10 pp*, 2008.

[10] Barrientos B., Cywiak M., Lee W.K., and Bryanston-Cross P. Measurement of dynamic deformation using a superimposed grating. *Rev. Mex. Fs. 50(1) 12-18*.

[11] Dalziel B., Highes G., and Sutherland T. Synthetic schlieren. *Proceedings of the 8th International Symposium on flow visualization, ed. G. M. Carlomagno, I. Grant, 62.1-62.6*, 1998.

[12] Dalziel B.S., Hughes G.O., and Sutherland B.R. Whole-field density measurements by synthetic schlieren. *Exp. Fluids, 322-335*, 2000.

[13] Landreth C. C., Adrian J. R., and Yao C. S. Double pulsed particle image velocimetry with directional resolution for complex flows. *Exp. Fluid, 6, 119-128*, 1988.

[14] Van de Hulst H. C. Light scattering by small particles. *John Wiley and Sons*, 1957.

[15] Blanco D.M. Coparacion de metodos opticos para la medicion de temperatura en objetos de fase. *Tesis de maestria en ciencias, CIO*, 2011.

[16] Goldhahn E. and Seume J. The background oriented schlieren technique: Sensitivity, accuracy, resolution and application to a three-dimensional density field. *Exp. Fluids, 43: 241-249*, 2007.

[17] Elsinga G.E:, Van Oudheusden B.W., Scarano F, and Watt D. W. Assessment and application of quantitative schlieren methods: Calibrated color schlieren and background oriented schlieren. *Exp. Fluids 36, pp 309-325*, 2004.

[18] Richard H. and Raffel M. Principle and application of the background oiented schlieren (bos) method. *Measurement Science and Technology 12, pp 1576-1585*, 2001.

[19] Adrian R. J. Scattering particle characteristics and their effect on pulsed laser measurements of fluid flow: speckle velocimetry vs particle image velocimetry. *App. Opt. 23, 1690-1691*, 1984.

[20] Huang H. J. and Waas A. M. Improved speckle method for measuring in-plane displacement and strain fields. *Opt. Eng. 46(5), 051005*, 2007.

[21] Szinitman J. and Rosgen T. Whole-field density visualization and abel reconstruction of axisymmetry vortex rings. *J. Flow Visual. Im. Process. 13 343-358*, 2006.

[22] Kopf. Application of speckling for measuring the deflection of light by phase objects. *Opt. Comm. 5(5), 347-350*, 1972.

[23] Cerca M., Barrientos B., Garcia-Marquez J., and Hernandez-Bernal C. Obtencion del relieve digital mediante proyeccion de luz estructurada en modelos analogicos de extension. *Bol. Soc. Geolog. Mex., Tomo LIX(1), 101-113*, 2007.

[24] Raffel M., Willert C., and Kompenhans J. Particle image velocimetry, a practical guide. *Springer - Verlag, Berlin*, 1998.

[25] Stanislas M. and Monnier J. C. Practical aspects of image recording in particle image velocimetry. *Meas. Sci. Technol. 8, 1417-1426*, 1997.

[26] Vinnicheko N., Uvarov A., and Plaksina Y. Accuracy of background oriented schlieren for different background patterns and means of refraction index reconstruction. *15th International Symposium on flow visualization, Minsk, Belarus*, 2007.

[27] Wernet M. P. Particle image velocimetry processing pivproc. *notes from The Glenn Research Center NASA*, 1999.

[28] Grousson R. and Mallik S. Study of flow patterns in a fluid by scattering laser light. *App. Opt., 16, 1334-1337*, 1977.

[29] Debrus S., Francon M., Grover C., May M., and Roblin M. Ground glass differencial interferometer. *App. Opt. 11(4), 853-857*, 1972.